



KING'S COLLEGE LONDON
DEPARTMENT OF PHYSICS

CO₂ Reduction on Cu Nanocatalysts

Investigating how the formation process of Cu nanoparticles affects their
CO₂RR activity.

Author

Elena Gazzarrini

Supervisor

Dr. Francesca Baletto

A thesis presented for the degree of

MSci in Physics

April 3, 2020

Abstract

We propose a multiscale numerical model to estimate how the formation process to produce Cu nanoparticles affect their catalytic activity for CO₂ reduction. Although this reaction can lead to multiple hydrocarbon products, we focus our attention on the hydrogenation to methane for which the protonation of CO to CHO is the rate-limiting step. Using classical molecular dynamics, we model three formation processes, namely the annealing from a liquid droplet; the solid growth proceeding via the addition of single atoms; and the coalescence of two nanoparticles. We explore the size range between 1.5-2.5 nm. Our model analyses the evolution of the generalised coordination number during the formation process and employs an available structure-energy relationship to estimate the specific and the mass activities. We show that each formation process leads to a different size-behaviour for the activity. The obtained mass activities range between 5.2-11.2 mA/mg. There is a clear evidence that surface roughness and defects improve catalytic performance of Cu nanoparticles for the CO protonation. Quite surprisingly, the activity has a different size-trend depending on the formation process. While the annealing has a monotonic decrease with the nanoparticle size, larger and more defected nanoparticles obtained via the one-by-one growth - although depending on the shape of the initial seed - are the most active. Coalescence has a non-monotonic behaviour with size strongly depending on how fast necks and interfaces of the individual nanoparticles rearrange.

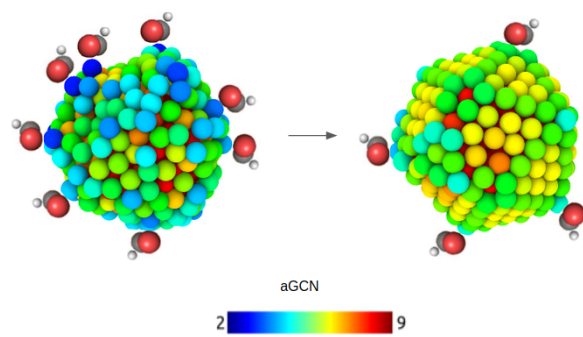


Figure 1: CHO adsorption on low coordinated sites of a Cu₅₆₁ nanoparticle in its liquid state (left) and after a liquid-solid phase transition (right). The legend symbolises how coordinated each site is, from low (2) to high (9).

Acknowledgements

I thank Dr. Francesca Baletto for helping and supporting me all the way through the project, and for introducing me to this exciting research area. Ideas and concepts also derive from insightful discussions with Matteo Tiberi, Robert Jones, Laia Delgado and Armand Auquier.

Contents

1	Introduction	9
1.1	A brief summary on CO ₂ conversion	9
1.2	Copper Nanoparticles	11
2	Methodology	15
2.1	NanoCHE model for CO ₂ RR	15
2.2	LoDiS Simulations	18
2.2.1	Freezing	20
2.2.2	Growth	20
2.2.3	Coalescence	20
2.2.4	Choosing the starting configuration	21
2.3	Analysis	23
2.3.1	Energetic Analysis	24
2.3.2	Geometric Analysis	24
2.3.3	Catalytic Analysis	28
3	Results and Discussion	31
3.1	Energy Considerations	31
3.2	atop Generalized Coordination Number	41
3.2.1	Discrete Histograms	41
3.2.2	Visual Representations	46
3.3	Catalytic Activity	55
3.3.1	Setting the NanoCHE	55
3.3.2	Current Density	58

3.3.3	Surface Area	64
3.3.4	Mass Activity	65
4	Conclusions	69
5	Further Extensions	71
	Bibliography	71
	Appendices	80

List of Figures

1	CHO adsoption on low coordinated sites of a Cu ₅₆₁ nanoparticle in its liquid state (left) and after a liquid-solid phase transition (right). The legend symbolises how coordinated each site is, from low (2) to high (9).	2
2.1	Workflow. The formation process (freezing, growth, coalescence) is investigated by means of CMD. Various shapes and sizes are produced. They are geometrically characterized through a CNA and by analysing their aGCN distribution. By combining our data with other studies (reported in the  box) the current density j produced by the NPs' surfaces is calcualted, to then measure the clusters' mass activity and quantify their catalytic properties.	16
2.2	Initial structures for MD. <i>a</i>) Cu ₁₁₀ (bh), <i>b</i>) Cu ₁₃₀ (bh), <i>c</i>) Cu ₁₄₆ (Oh), <i>d</i>) Cu ₁₄₇ (Ih), <i>e</i>) Cu ₂₀₁ (To), <i>f</i>) Cu ₂₅₀ (bh), <i>g</i>) Cu ₂₇₀ (bh), <i>h</i>) Cu ₂₈₅ (bh), <i>i</i>) Cu ₄₀₅ (To), <i>j</i>) Cu ₄₃₄ (mDh), <i>k</i>) Cu ₅₆₁ (Ih), <i>l</i>) Cu ₅₈₅ (mDh), <i>m</i>) Cu ₅₈₆ (To), <i>n</i>) Cu ₈₉₁ (Oh), <i>o</i>) Cu ₉₇₆ (To).  is representative of Ih structures,  of FCC and  of Dh.	22
2.3	Visual representation of aGCN on a mDh (Cu ₅₈₅). Low-coordinated sites are colored in blue, highly-coordinated, bulk-like sites in red.	26
2.4	Snapshots at specific times (time evolution going left to right) are taken for <i>i</i>) a freezing of Cu ₁₄₇ , <i>ii</i>) a freezing of Cu ₉₇₆ , <i>iii</i>) a growth from Cu ₁₄₇ to Cu ₉₉₇ and <i>vi</i>) a coalescence of Cu ₄₃₄ +Cu ₂₈₅ . Atoms are colored according to their aGCN, to show that aGCN values between 2 and 9 belong to the NPs' surfaces.	27

3.1	Excess energy development in freezing processes at a rate of <i>i</i>) 50 K/ns, <i>ii</i>) 10 K/ns and <i>iii</i>) 5 K/ns. The legend represents the number of atoms, namely the size of the NP.	32
3.2	How initial random parameters affect structure formation in freezing processes (5 K/ns). From top left to bottom right: Cu ₁₄₇ , Cu ₂₅₀ , Cu ₅₆₁ , Cu ₅₈₅ , Cu ₅₈₆ , Cu ₈₉₁ , Cu ₉₇₆ . The different colors represent the four simulations run for each system.	34
3.3	How initial random parameters affect structure formation in a growth process. From left to right, initial structures are Cu ₁₄₆ , Cu ₁₄₇ , Cu ₂₀₁ . The different colors represent the four simulations run for each system.	36
3.4	Excess energy evolution in growth processes.	38
3.5	How initial random parameters affect structure formation in coalescence processes. From top left to bottom right: Cu ₂₄₀ , Cu ₅₂₀ , Cu ₅₈₁ , Cu ₇₁₉ , Cu ₈₃₉ . The different colors represent the four simulations run for each system.	39
3.6	Excess energy evolution in coalescence processes.	41
3.7	aGCN occurrence in freezing processes. From top left to bottom right: Cu ₁₄₇ , Cu ₂₅₀ , Cu ₅₆₁ , Cu ₅₈₅ , Cu ₅₈₆ , Cu ₈₉₁ , Cu ₉₇₆ . The label colors represent different time steps of the simulation.	42
3.8	aGCN occurrence in growth processes. From left to right, the initial geometries are To, Ih and FCC. The label colors represent different time steps of the simulation, and therefore different number of atoms in the cluster.	43
3.9	aGCN occurrence in coalescence processes. The label colors represent different time steps of the simulation	44
3.10	aGCN occurrence at 600K for different processes (■ freezing, ■ growth and ■ coalescence) and different cluster dimensions.	45
3.11	aGCN occurrence time evolution in the freezing of Cu ₁₄₇ (left) and Cu ₂₅₀ (right). Figures' snapshots are taken at 0 ns, 160 ns and at the time corresponding to the freezing temperature.	47

3.12 aGCN occurrence time evolution in the freezing of Cu ₅₆₁ (top left), Cu ₅₈₅ (top right), Cu ₅₈₆ (bottom left) and Cu ₈₉₁ (bottom right). Figures' snapshots are taken at 0 ns, 160 ns and at the time corresponding to the freezing temperature.	48
3.13 aGCN occurrence time evolution in the freezing of Cu ₉₇₆ . Figure's snapshots are taken at 0 ns, 160 ns and at the time corresponding to the freezing temperature.	49
3.14 aGCN occurrence time evolution in growth processes. From top left, the evolution of an Oh, of an Ih and of a To (FCC). Snapshots of the structure are taken at three different moments (0 ns, 125 ns, 250 ns) for each process.	50
3.15 aGCN occurrence time evolution in coalescence processes. Cu ₁₁₀ +Cu ₁₃₀ (left) and Cu ₂₇₀ +Cu ₂₅₀ (right). Structures' snapshots are taken at initial, collision and final times.	51
3.16 aGCN occurrence time evolution in coalescence processes. Cu ₁₄₇ +Cu ₄₃₄ (left) and Cu ₂₈₅ +Cu ₄₃₄ (right). Structures' snapshots are taken at initial, collision and final times.	52
3.17 aGCN occurrence time evolution in coalescence processes. Cu ₄₀₅ +Cu ₄₃₄ . Structure's snapshots are taken at initial, collision and final times.	53
3.18 Database of resulting structures from different formation processes. The freezing gives spherical shapes, the growth ends up in flatter shapes, and coalescence in elongated structures.	54
3.19 First attempts to find the constant.	57
3.20 Current density produced by frozen Cu ₅₆₁ calculated with C2 as a constant.	58
3.21 Current density for applied potential V in freezing processes. From top left to bottom right: Cu ₁₄₇ , Cu ₂₅₀ , Cu ₅₆₁ , Cu ₅₈₅ , Cu ₅₈₆ , Cu ₈₉₁ and Cu ₉₇₆ . The yellow ■ lines represent the current produced by the liquid structures, while the red ■ ones the color produced by the frozen ones.	59

3.22	Current density for applied potential V in growth processes. From top left to bottom right: growth of an Oh, Ih and FCC geometry. The different colors represent the number of atoms making up the NP: ■ for 250, ■ for 561, ■ for 719, ■ for 976.	60
3.23	Current density for applied potential V. From top left to bottom right: $\text{Cu}_{110} + \text{Cu}_{130}$, $\text{Cu}_{270} + \text{Cu}_{250}$, $\text{Cu}_{147} + \text{Cu}_{434}$, $\text{Cu}_{285} + \text{Cu}_{434}$ and $\text{Cu}_{405} + \text{Cu}_{434}$. The yellow ■ lines represent the initial system, while the red ■ ones the final elongated structure.	61
3.24	IV curves for $\text{CO} \rightarrow \text{CH}$. (top) freezing process, dashed line refers to the melted phase and solid-line for the frozen object; (middle) growth one-by-one, different colours refers to different initial seeds; (bottom) coalescence after 0.05 ns.	63
3.25	Surface area time evolution for the various processes.	64
3.26	Mass activity evolution in mA/mg. The lines have been smoothed using a Gaussian fit to make them more readable. The plots refer to (top) freezing process, (middle) growth one-by-one and (bottom) coalescence. The legends for freezing and coalescence represent the number of Cu atoms.	67
5.1	CNA pattern evolution for Cu_{561} , leading to an Ih, Cu_{891} , leading to a dOh, and Cu_{976} , leading to a dTo with FCC facets.	81
5.2	CNA pattern evolution for an initial Oh, Ih and FCC, which are grown.	82
5.3	CNA pattern for final structures resulting from growth processes. . .	83

List of Tables

2.1	Cu RGL potential parameters.	19
3.1	Table showing the final excess energy for fast (f), medium (m) and slow (s) rates.	33
3.2	Outcomes of different structure processes during slow freezing depending on the initial condition. dFCC, dIh and dDh are defected structures, meaning their CNA pattern is up to 70% identical to the one corresponding to a perfectly ordered geometry of that kind. . . .	35
3.3	Outcomes of different structure processes during slow freezing depending on the initial condition. dFCC, dIh and dDh are defected structures, meaning their CNA pattern is up to 70% identical to the one corresponding to a perfectly ordered geometry of that kind. . . .	37
3.4	Outcomes of different structure processes during coalescence depending on the initial condition. dFCC, dIh and dDh are defected structures, meaning their CNA pattern is up to 70% identical to the one corresponding to a perfectly ordered geometry of that kind. Amorphous structures do not present any kind of geometry.	40
3.5	aGNC related to Cu Miller indices [32]. The last two lines refer to adatoms, namely trimers and dimers.	56
3.6	Different Cu foil compositions to calculate the constant.	57

Introduction

1.1 A brief summary on CO₂ conversion

Carbon dioxide (CO₂) is the most prominent greenhouse gas, released by both natural and artificial processes. In an ideal scenario, the CO₂ produced on Earth should be balanced with what is consumed, so that the level of CO₂ remains constant to maintain environmental stability. Unfortunately, with the intensification of human industrial activities – primarily from use of fossil fuels and deforestation –, this balance has gradually been disrupted, leading to more CO₂ production and making global warming a pressing issue. Therefore, reducing CO₂ production and converting CO₂ into useful materials seems to be necessary, indeed critical, for environmental protection [1–3].

The different proposed technologies follow one of two major approaches: (i) to capture and geologically sequestrate CO₂; (ii) to convert CO₂ into useful low-carbon fuels [4]. The latter approach is going to be investigated.

As CO₂ is thermodynamically stable and kinetically inert [5, 6], its efficient conversion requires the use of catalysts. A catalyst is a substance that enables a chemical reaction to proceed at a usually faster rate or under different conditions (as at lower temperature) than otherwise possible, lowering the activation barrier of the chemical reaction.

In recent years, CO₂ conversion using electrochemical catalysis approaches has attracted great attention for its several advantages: (1) the process is controllable by electrode potentials and reaction temperature; (2) the supporting electrolytes can be fully recycled so that the overall chemical consumption can be minimized to water only; (3) the electricity used to drive the process can be obtained by employing re-

newable energies — sources include solar, wind, hydroelectric, geothermal, tidal, and thermoelectric processes - ; (4) the electrochemical reaction systems are compact, modular, on-demand, and easy for scale-up applications [7] and ; (5) electrochemical conversion using electrocatalysis offers a means of producing transportation fuels and commodity chemicals using intermittent renewable electricity [8–10].

This means that CO₂ hydrogenation to hydrocarbons is becoming a hot topic in the field of renewable energies, being employed in the production of fuel cells, which convert chemical energy into electrical energy. Fuel cells offer a high-efficiency and low-emission alternative to internal combustion engines (ICE) in vehicle applications, producing smaller quantities of greenhouse gases and none of the air pollutants (such as nitrogen oxides) that create smog and cause health problems. It has been proven that up to 40% less fuel fuel energy is required from the fuel cell compared to an ICE to cover the same distance, and that a fuel cell can match the performance of an ICE range extender with up to twice the rated power output [11].

The CO₂ Reduction Reaction (CO₂ RR) activity and selectivity are impacted by the catalyst surface structure, morphology, composition, the choice of electrolyte ions and pH, and the electrochemical cell design. A major goal of applied electrocatalysis research is the development of electrode materials and conditions that are selective and active (as well as cheap and stable) for production of desired products [12].

The CO₂ electro-chemical conversion requires more than two electrons ($> 2e^-$ products), e.g., methane, methanol, ethylene, etc. [13, 14]. Therefore, developing catalysts that are effective for CO₂RR to $> 2e^-$ products would greatly improve prospects for utilization, and such an endeavor requires a deeper understanding of the relevant surface chemistry.

In general, the CO₂RR is described by the Equation 1.1.



As can be noticed, the only biproducts of this reaction are low-carbon fuel, hydrocarbons or other non-harmful products, and water. However, the use of catalysts is needed for this reaction to happen. Nanoparticles (NPs) are deemed to be likely candidates for this purpose, as explained in the following section.

1.2 Copper Nanoparticles

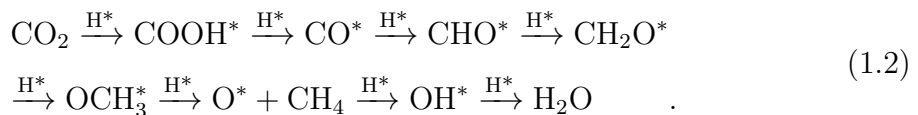
Nanoparticles can be defined as objects having characteristic length scale lying within the nanometric range, that is, in the range between one and several hundreds of nanometers. They are interesting for surface and material science given their large surface area per unit volume [15]. In particular, metallic NPs - composed of metals, i.e. Ni, Cu, Pd, Ag, Pt, Au, Pd, Ir - hold great promise for heterogeneous catalysis in electrochemical reactions, due to (1) their electric properties; (2) their high dispersion; (3) the fact that they are structurally dynamic objects [17, 18]; (4) their potential to tune the catalytic performance by adjusting their shape, size and chemical composition; (5) the large concentration of highly under-coordinated sites on their surface; and (6) the presence of quantum confinement effects, which can drastically alter their reactivity [16]. In this view, the use of metallic NPs to catalyse more efficiently and selectively chemical reactions has the potential to trigger a revolution in the green economy.

Two factors should be simultaneously taken into account: (i) the variety of adsorption sites per each isomer [19], which influences its activity and selectivity, and (ii) the coexistence of different geometries, eventually related to their formation process [20]. Numerical guidelines enable researchers to pursue the synthesis of samples with a well defined and optimal architecture (size, shape, chemical composition and ordering) avoiding a costly and ineffective trial-and-error procedure. Usually each electrochemical reaction requires a specific metal to act as a catalyst.

Out of the polycrystalline metals, copper (Cu) is the only heterogeneous catalyst that has shown a propensity to produce valuable hydrocarbons, aldehydes and alcohols, such as ethylene and ethanol, from electrochemical CO₂RR [5]. It is also the only one that has shown a propensity for CO₂ reduction to $> 2e^-$ products at considerable rates and selectivity [21, 22]. To date, its uniqueness is reflected by how nearly all work on catalysts with improved activity and selectivity for $> 2e^-$ products is based on Cu [23, 24]. However, poly-crystalline Cu is not particularly selective toward any one $> 2e^-$ reduction product [25]. Thus, studies have been performed to understand which active site motifs lead to this unique selectivity for

further reduced products and to apply this knowledge to develop new materials with this electrocatalytic behavior. These examinations involve plasma treatments [26], annealing Cu foil in air [27] and employing electrolyte solutions [28].

Copper produces a variety of hydrocarbon species because it can protonate adsorbed CO intermediates. In fact, protonation of adsorbed CO has been predicted to be a key step in hydrocarbon formation. In this study we focus on CO₂ reduction to methane (CH₄), although other products can be examined similarly. The reaction pathways from CO₂ to CH₄ on Cu have been established by Peterson et al. [30,31] and are summarized below:



The seven adsorbed intermediate species are denoted by *. Along each elementary step, a proton - electron pair is transferred from one intermediate to the next until the final product of H₂O is obtained [32]. Two intermediate reactions are key in the methane pathway. In the first, CO₂ and a proton-electron pair react to form adsorbed carboxyl, COOH. This is the key step involved in forming CO from CO₂. The second key step in the methane pathway is the limiting elementary step of the reaction; it involves the protonation of adsorbed CO to make adsorbed CHO [33]. The binding energy difference between the two adsorbates will dictate the relative activity of each NP's facet.

To understand if a material is a good catalyst for the reaction, the reaction rate on top of it is analyzed. As Density Functional Theory (DFT) calculations have shown, CO₂ RR is structure sensitive [35]. The catalytic performance is therefore closely associated with the electronic structure of the active site [34,36]. The activity of a site, or of a NP, is the rate of a specific reaction happening on its surface. It is reported in two distinct ways in the literature: specific activity (SA), which is the reaction rate normalized to the real surface area of the catalyst, and mass activity (MA), which is the rate normalized to the mass of the catalyst employed. The specific activity determines how much current is achieved at a certain applied overpotential. The overpotential of a reaction is the absolute difference between the actual potential needed to make a product and the thermodynamic potential. A

more active catalyst achieves a given current density at low overpotential or provides large current density at given overpotential.

The prediction of the catalytic activity of Cu by means of a geometrical analysis finds an accurate result upon the suitable choice of a geometrical descriptor. The necessary condition is that the descriptor correctly classifies all the different nanoparticle adsorption sites, as a function of its size and shape [37]. For the case of the electrochemical reduction of carbon dioxide to CH₄, which involves the atop adsorption of CO, the generalized coordination number, GCN, has been proven to be a robust descriptor, as demonstrated by Zhao et al. [32]. The core assumption of this model is that the reaction free energy ΔG of the rate limiting step of the reaction can be written as a function of the generalized coordination number. The latter should uniquely classify every adsorption site of a metallic nanocluster, count its occurrence and relate the energetics of the adsorbate, in this case CO₂, to the local atomic environment of the site. The ensemble of geometric descriptors becomes, in a way, the isomer's 'genome'.

It is known, and proven again in this work, that sites with a low GCN, meaning surface sites which are loosely coordinated to each other, lead to more active structures. An example of this concept is given by the liquid-solid phase transition: liquid NPs (disordered, with many low-coordinated sites) are much more active than solid ones. In the bulk, for example, the lower coordinative unsaturation leads to narrowing of the d-band, which results in an upward shift of the band's energy and, consequently, in stronger adsorption of reaction intermediates [38]. Especially, small-sized Cu clusters with low-coordinated surface atoms are more favorable for CO₂ dissociation than larger particles. This trend is consistent with Brønsted-Evans-Polanyi (BEP) principle - which relates the activation barrier to the enthalpy of an elementary reaction step -, as lower activation barriers go together with more exothermic nature of the CO₂ dissociation reaction [38].

Observations also clearly indicate that the enhanced activity and selectivity of Cu for CO₂ reduction to CHO and COOH (Equation 1.2) over H₂O reduction is associated with the formation of more active low-index Cu facets [10]. It is suggested that COOH, the key intermediate involved in CO₂ reduction to CO, binds to open

facets of Cu (e.g., (100) and (211)) much more strongly than close-packed (111) facets. This would lower the overpotential required for producing CO from CO₂ reduction [33]. The limiting potential at which Cu catalyzes the electro-chemical reduction of CO₂ to CH₄ is predicted to be lowest on the (211) surface. This suggests that most of the hydrocarbon formation that takes place on Cu is taking place on stepped surfaces, or the related kinks and defects [33]. Surface morphology effects in CO₂ electro-reduction were also explored by Tang and Hori et al. [39, 40]: steps on roughened Cu surfaces show a significant influence on the selectivity for CO₂ reduction.

This study tries to take a step further in the CO₂RR framework. Even if copper has already largely been used as a catalyst to reduce the CO₂ concentration in the atmosphere, many devices are still expensive and require a long time to be produced - such as fuel cells -. It is still a challenge to reach higher efficiencies [28]: as of today, the electrochemical reduction of CO₂ into fuels and other useful products yet requires high overpotentials, close to 1 V. This value is high compared to the 0.57 V required for the O₂ Reduction Reaction (O₂RR) on Pt, for instance [41].

Thus, we are interested in investigating the catalytic activity of a range of structures. These are explored through the lens of Classical Molecular Dynamics (CMD). They are subjected to three main processes: freezing, growth and coalescence. The current density produced by their surface at various moments of time is quantified and compared, to find which are eventually the most active shapes and sizes. We anticipate that our results may be of interest to the experimental communities - who could use our findings to engineer tailored experiments.

Methodology

The workflow of this study is visually represented in Figure 2.1. We follow the strategy outlined in [42] to understand how the formation process of NPs could lead to more active Cu-NPs. We set up a NanoCHE (Computational Hydrogen Evolution) model to do this, by combining data from Zhao et al. [32] and Loiudice et al. [43] mainly. A nanocatalyst design process [44] is made possible by the fact that suitable descriptors significantly promote the classification of catalyst structures into more or less defined geometries. We model different formation processes (freezing, growth, coalescence) through CMD simulations and we use a Common Neighbour Analysis (CNA) [46, 47] to quantify and classify structural changes and defects formation, i.e. re-entrances and elongated concavities, and the formation of twin planes, grain boundaries, and five-fold axes. To estimate the evolution of the mass activity for various nanoparticle shapes, we employ the relationship between the atop Generalised Coordination Number (aGCN) and the overpotential for the limiting step of CO₂ reduction reaction to CH₄ on Cu surfaces investigated by Zhao et al. [32].

2.1 NanoCHE model for CO₂RR

The NanoCHE approach pioneered by Norskov and co-workers represents a very promising way to enable modeling of electrochemistry by quantitatively incorporating insights from first-principles calculations [68]. The inclusion of quantum mechanical data imparts predictive capability and eliminates the need to make drastic simplifying assumption in the model. At the core of this approach is a specified reaction mechanism and the evaluation of the free energy of the corresponding elementary steps, $\Delta G = \Delta H - \Delta S$, where H is the enthalpy and S is the entropy

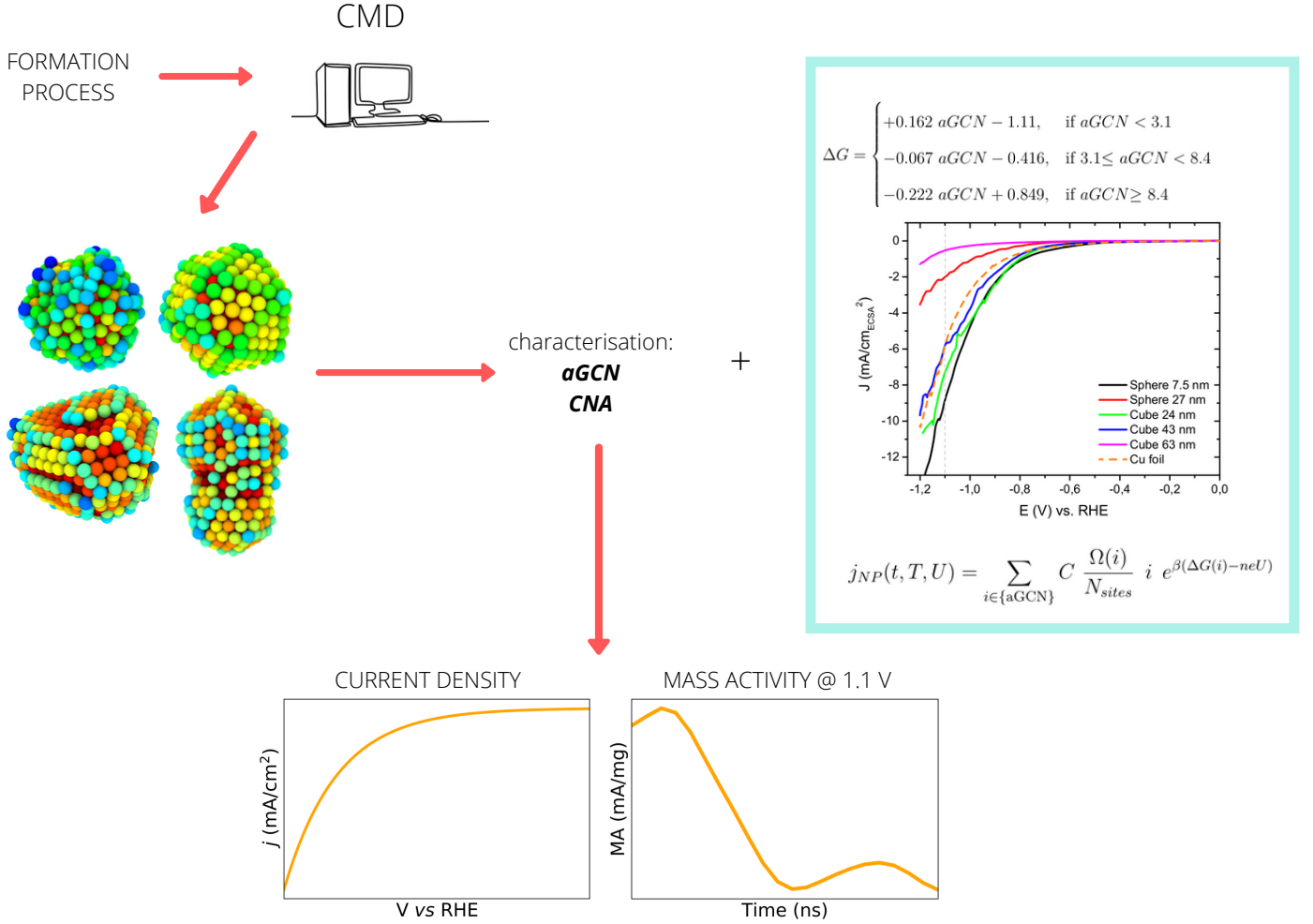


Figure 2.1: Workflow. The formation process (freezing, growth, coalescence) is investigated by means of CMD. Various shapes and sizes are produced. They are geometrically characterized through a CNA and by analysing their aGCN distribution. By combining our data with other studies (reported in the ■ box) the current density j produced by the NPs' surfaces is calculated, to then measure the clusters' mass activity and quantify their catalytic properties.

of the reaction. The key gateway to introduce electronic structure information into the model is via the free energy of individual component in each of the elementary step [78].

The other assumption for this model is that ΔG can be related to some descrip-

tor. From an early stage, d-band centers have been an important concept in the field of catalysts design; however, the necessity of density functional theory based calculations for d-band studies further stimulated the identification of more affordable descriptors [49]. To this end, conventional coordination numbers, counting the number of first nearest neighbors of the active sites, yield appropriate scaling relations for catalytic activities of extended surfaces [50, 51]. However, activity trends for nanoparticle catalysts remain out of scope due to finite size effects [52]. In recent studies, Calle-Vallejo et al. extended the concept of coordination number to the second nearest neighbors by means of generalized coordination numbers (GCN), which have been proven simple descriptors for catalytic activities of various reactions [44], and are therefore included in the NanoCHE model. A linear scaling relationship between the binding energy and the aGCN for each step of the CO₂ reduction reaction is taken from the work by Zhao et al. [32]. The relation seems particularly strong for the intermediates which bond with the active site through a carbon atom, such as CO* and CHO*.

The limiting potential U_L for a reaction step is defined as the difference between the free energies of the involved reactants, minus the chemical potential of a proton-electron pair calculated as half of the chemical potential of gas-phase H₂ at 0 V. U_L can be plotted as a function of the aGCN, as can be seen in [32]. The distances between the U_L=0 line and the most negative U_L line represent the minimum potentials required to guarantee all reaction steps to be exothermic. The three most negative U_L lines outline the so-called volcano plot. The intersection between the first and the second line at GCN = 3.1 defines the volcano top, which represents the lowest possible overpotential for CO₂ → CH₄ on Cu surfaces. The equations which relate the limiting step reaction free energies ΔG to the aGCN are as follow:

$$\Delta G = \begin{cases} +0.162 \text{ } aGCN - 1.11, & \text{if } aGCN < 3.1 \\ -0.067 \text{ } aGCN - 0.416, & \text{if } 3.1 \leq aGCN < 8.4 \\ -0.222 \text{ } aGCN + 0.849, & \text{if } aGCN \geq 8.4 \end{cases}, \quad (2.1)$$

where the first line corresponds to the reaction step OH* $\xrightarrow{\text{H}^*}$ H₂O, the second

line to the reaction $\text{CO}^* \xrightarrow{\text{H}^*} \text{CHO}^*$, and the third to $\text{CO}_2 \xrightarrow{\text{H}^*} \text{COOH}^*$.

Once this relation is set up, the aim of this study is to calculate the current density, j , produced by each nanocluster. This is achieved through Equation 2.2 [68].

$$j_{NP}(t, T, U) = \sum_{i \in \{\text{aGCN}\}} C \frac{\Omega(i)}{N_{sites}} i e^{\beta(\Delta G(i) - neU)} . \quad (2.2)$$

The current density measurement appears at a certain temperature T which determines the Maxwell-Boltzmann factor. $\{\text{aGCN}\}$ refers to the aGCN fingerprint. Each aGCN fingerprint appears with a specific occurrence Ω , and N_{sites} corresponds to the number of surface sites for which the coordination number is calculated. The number of sites which participate in the reaction each time is defined by n , and is therefore equivalent to 1 since we are only considering atop sites; e is the electron charge and U is the applied potential, measured in eV/e. The pre-factor C is a constant fitted to reproduce the known specific current of low-Miller index surfaces and has units of mA/cm².

The Equation is going to be investigated in detail in the next section, but it can be seen how (1) the chemical problem is treated as a thermodynamical one, by adding a perturbation of neU to the free energy ΔG , as required by the NanoCHE model, and (2) the current density, which determines the catalytic activity of the nanocluster, is dependent on a geometric descriptor, namely the aGCN.

To forecast the correlation between catalytic activity of copper and structural changes upon a timescale of nanoseconds, various molecular dynamics tools available in the LoDiS package [54] are employed to monitor the evolution of the atop coordination number, and then the mass activity during the formation process of Cu-NPs.

2.2 LoDiS Simulations

Classical Molecular Dynamics is a computational algorithm which integrates Newton's equation of motion according to a finite difference method to simulate the time evolution of a system from certain initial conditions. A Velocity-Verlet algorithm [53] is exploited to evolve Newton's Equation of motion. It is an energy-conserving, time

reversible, order four error on position algorithm where positions and velocities are calculated throughout a Taylor expansion of both [54].

$$\begin{aligned} r(t + \Delta t) &= r(t) + v(t)\Delta t + \frac{F(t)}{2m}\Delta T^2 + \mathcal{O}(\Delta T^3) \\ v(t + \Delta t) &= v(t) + \frac{F(t) + F(t + \Delta T)}{2m}\Delta T^2 + \mathcal{O}(\Delta T^3) \end{aligned} \quad . \quad (2.3)$$

F represents the force on the particle, r its position and v its velocity. ΔT is the time step of the algorithm, which is equivalent to 5 fs in our study; this is approximately the typical phonon frequencies (1 to 7 fs). In this study, the software utilised to run MD simulations is LoDiS (Low Dimensional System), a FORTRAN90 computational engine specifically tailored to the study of processes at the nanoscale in finite-size systems. The LoDiS package allows different processes to take place, according to the initial parameters given. In this study we investigate the freezing, the growth and the coalescence of Cu clusters. For each different process the nanoparticles (NP) are placed in vacuum. The atomic interaction is described by the RGL potential (Rosato-Guilope-Legrand potential [54]), which is dictated by the Equation 2.4:

$$E_i = \sum_{j \neq i}^n A e^{-p(\frac{r_{ij}}{r_0} - 1)} - \sqrt{\sum_{j \neq i}^n \xi^2 e^{-2q(\frac{r_{ij}}{r_0} - 1)}} \quad , \quad (2.4)$$

A and ξ are related to the cohesive energy, p and q tune the stickiness of the potential, while r_0 is the bulk nearest neighbor distance and r_{ij} is the set of all atomic coordinates. The parameters values for monoatomic Cu clusters are displayed in Table 2.1.

p	10.55
q	2.43
A[eV]	0.089
ξ [eV]	1.28
r_0 [\AA]	2.56
E_{coh} [eV]	3.50

Table 2.1: Cu RGL potential parameters.

All the simulations are conducted under an Andersen thermostat which is used to mimic the interaction of the system with a heat bath that allows the temperature of the system to fluctuate around a selected temperature through virtual instantaneous interactions. Its frequency is set at $5 \cdot 10^{11}$, which is the limit needed to have an efficient thermostat where the particle's diffusive properties are not affected.

2.2.1 Freezing

Freezing (itMD - iterative Molecular Dynamics) processes are characterized by concatenated canonical NVT runs, where the temperature is lowered. The temperature is lowered by a factor of ΔT every time step $\Delta\tau$, resulting in a freezing rate of $\rho = \Delta T / \Delta\tau$ [55]. The ratio ρ tunes the cooling/heating parameter which impacts the kinetics of the liquid-solid transitions. This process allows to get caloric curves, to determine freezing points and to investigate liquid-solid transitions kinetics.

2.2.2 Growth

Atom by atom deposition happens on an initial metallic nucleus, thermalization and relaxation of the cluster are allowed between two depositions. This is a simulation where the temperature is fixed and on the original NP cluster, n atoms, one at the time, are deposited every τ steps and allowed to thermalize for 2τ steps. Atoms are shot towards the center of mass from a sphere 3 times larger of the NP with a velocity extracted from a Boltzmann Distribution coherent with the temperature of the source.

2.2.3 Coalescence

Coalescence is the process by which two clusters are brought into contact along the z axis. Following thermalization, one of the clusters can be translated towards the other with kinetic energy comparable to the system's initial temperature. Once in contact, the clusters are left to evolve and aggregate under the potentials with a temperature lower than the initial one, tuned by the Anderson thermostat. The impact velocity plays a significant role in the formation process of the final aggregate.

Whereas growth involves a step by step increase in total energy and atomic number allowing for thermalization between depositions, coalescence is an immediate process with an aggregation time shorter than the time scale to equilibrate.

2.2.4 Choosing the starting configuration

The dynamic changes in shape, symmetry, and atomic coordination of atoms within clusters occurring in the picoseconds regime are suited to simulate the catalyst properties of a structure; this is due to the fact that this time scale corresponds to the duration of chemical reactivity. The change of coordination of the metal in the same time scale as that of chemical reactivity is called dynamic structural fluxionality, and should in principle allow structural adaptation towards the most favorable free-energy path. Fluxionality is an important contributing factor to the catalytic activity of metal nanoclusters, since transition state activation barriers of catalyzed reactions are lowered by structural deformations of the cluster in the course of reaction [56–58]. For this reason, different CMD processes are used to investigate NPs’ activity.

The structures employed in this study vary from a size of 110 to 976 atoms, all categorized under spherical geometries, since the molecular dynamics simulation potential is symmetric. The diameters range between values of 1.5 and 2.5 nm. We sequence the aGCN kind and occurrence in different structural motifs commonly observed in experiments. The geometries used are FCC structures, namely Octahedra (Oh) and their regular truncation (To), Icosahedra (Ih), marks-Decahedra (mDh) and defected Icosahedra resulting from a basin-hopping process (bh). The latter is obtained from an algorithm which allows to have transitions from a potential energy basin to another, by a canonical Monte Carlo simulation at constant T on the transformed cluster. In this framework, the transformation amounts to lowering the barriers between basins to the maximum possible extent, while keeping the levels of the minima unchanged [59]. The initial structures utilized for the CMD simulations are represented in Figure 2.2. The legend colors are an approximation to the nearest group (Ih, FCC or Dh) the clusters belong to.

Far from exhaustive of all available structural motifs, the ensemble of morpholo-

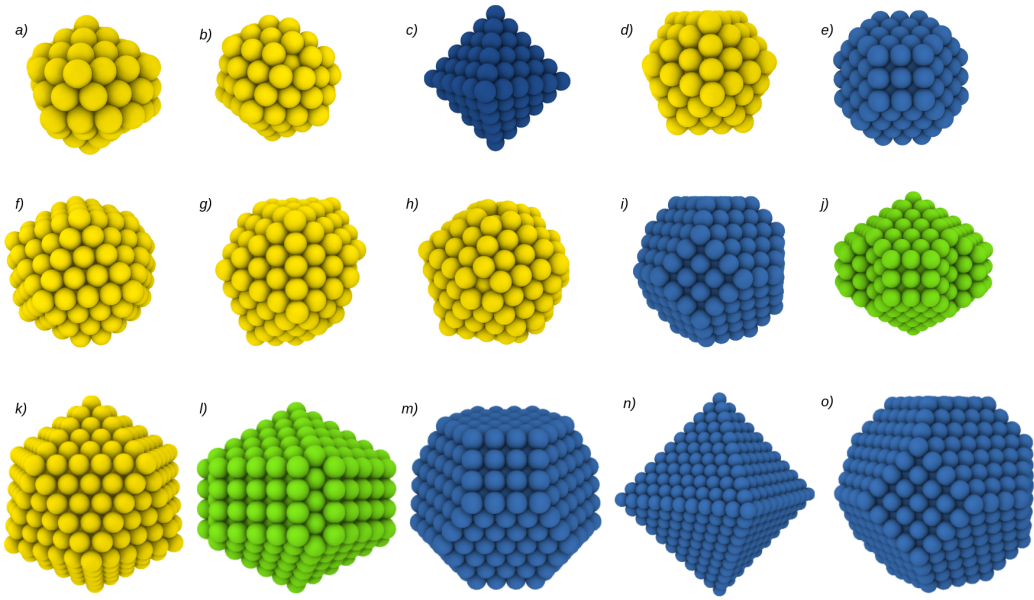


Figure 2.2: Initial structures for MD. *a)* Cu₁₁₀ (bh), *b)* Cu₁₃₀ (bh), *c)* Cu₁₄₆ (Oh), *d)* Cu₁₄₇ (Ih), *e)* Cu₂₀₁ (To), *f)* Cu₂₅₀ (bh), *g)* Cu₂₇₀ (bh), *h)* Cu₂₈₅ (bh), *i)* Cu₄₀₅ (To), *j)* Cu₄₃₄ (mDh), *k)* Cu₅₆₁ (Ih), *l)* Cu₅₈₅ (mDh), *m)* Cu₅₈₆ (To), *n)* Cu₈₉₁ (Oh), *o)* Cu₉₇₆ (To). ■ is representative of Ih structures, ■ of FCC and ■ of Dh.

gies under scrutiny provides a sufficient structural variety to test the effectiveness of our approach: the study of the nanoparticle geometrical genome to predict its catalytic activity.

For freezing processes, the initial temperature is set to 1200 K. At this point the structure has already been melted with a fast (itMD) melting, so it lacks any structure. The temperature is lowered by 25 K at every time step, until a minimum of 400 K. The freezing is conducted over a time of 160 ns at different rates to see if the speed of the simulation affects the phase transition: the fast rate is composed of 100000 time steps, which corresponds of a freezing rate of 50K/ns, the medium rate is composed of 500000 time steps (10K/ns), and the slow rate corresponds to 1 million steps (5K/ns). The structures analyzed are Cu₁₄₇, Cu₂₅₀, Cu₅₆₁, Cu₅₈₅, Cu₅₈₆, Cu₈₉₁ and Cu₉₇₆, which can be seen in Figure 2.2.

Growth processes are run at a fixed temperature of 600 K for 60000 steps for a total of 255 ns. Three initial structure are taken as the starting point: Cu₁₄₆, Cu₁₄₇,

to which 850 atoms are added, and Cu₂₀₁, which receives 795 deposited atoms. This choice is motivated by the will to start from three different structures (a Decahedron, an Icosahedron and a FCC structure), and analyze how this factor influences the evolution of the system.

Coalescence processes are run for a shorter amount of time, since the focus is on the structural analysis at some specific time steps, namely when the two NPs are placed at a distance from each other, when they collide and when they merge together, forming one elongated structure. The simulations are started when the two NPs are at a distance of 6 nm along the z axis, and are run at a temperature of 600 K for 10000 time steps, resulting in a total simulation time equivalent to 0.05 ns. The combinations are: Cu₁₁₀+Cu₁₃₀, Cu₂₇₀+Cu₂₅₀, Cu₁₄₇+Cu₄₃₄, Cu₂₈₅+Cu₄₃₄ and Cu₄₀₅+Cu₄₃₄. These sizes are comparable to the ones employed in the previous processes, so that a full comparison between the three of them is achievable.

To the extent of gathering relevant statistics, four simulations are run for the same system. This is accomplished by exploiting Lyapunov instabilities, which state that atoms' trajectories are extremely sensitive to small differences in initial conditions. Changing the variable *irand* in the input file enables to generate different initial atomic coordinates, and therefore to produce uncorrelated simulations.

2.3 Analysis

After trajectory and energy files are obtained from the CMD simulations, an analysis needs to be performed on each output. Firstly, an energetic analysis is conducted on each structure to explore which are the most energetically favourable processes and structures, and if this factor is ultimately connected with the reaction activity of the cluster. A common neighbor analysis is performed to classify the geometries into FCC, Ih and Dh. Secondly, a geometric analysis is employed: each atom is assigned an aGCN, the evolution of this descriptor with time is taken into consideration, with a highlight on the simulations' crucial moments (freezing temperatures for freezing, collision for coalescence), and its occurrence is analysed through time. Thirdly, the

aGCN is related to the reaction free energy of CO₂ reduction; the cluster's surface current density is analysed, considerations on the surface area are discussed, and finally the NP's mass activity is calculated.

2.3.1 Energetic Analysis

The shape of a nanocluster is strictly connected to its stability, since the binding energy is proportional to the volume and to surface parameters. A low surface energy suggests a quasi-spherical shape. However, a spherical shape would increase the internal strain of the cluster, thus increasing the volume energy contribution. Volume and surface energies are therefore in "competition" [59]. Comparative energetic analysis of structural stability can be carried out by looking at the excess energy, ΔE , evolution. It is defined as the energy in excess with respect to having N atoms in the bulk, weighted by the number of atoms in the surface, as in Equation 2.5:

$$\Delta E = \frac{E_{coh} - E_{pot}}{N^{2/3}}, \quad (2.5)$$

Where N is the number of atoms in the cluster, E_{coh} is the cohesive energy of the atoms in the bulk and E_{pot} is the potential energy of the relaxed nanocluster. Due to the different thermalisation processes, clusters with N atoms born from coalescence will have a larger ΔE compared to clusters with the same N components that are simply grown.

Since each simulation is run four times, the excess energy evolution through time of each of the four resulting structures is shown and discussed, and a brief analysis is performed to understand how different the features of each structure are. To get a physical result, the four excess energies are averaged into a $\langle \Delta E \rangle$, which is also plotted against time for each process. The energy comparisons between freezing, growth and coalescence mainly come from this last characterisation.

2.3.2 Geometric Analysis

The most important geometric descriptor to categorise nanoparticles is, in this specific case, the coordination number. The coordination number of an atom j, CN_j , is

the number of metallic atoms lying within a sphere of radius r_{cut} and centred around it, calculated in an analytic way:

$$CN_j = \sum_{i \neq j} f(r_{ij}), \quad f(r_{ij}) = \begin{cases} 0, & \text{if } r_{ij} \leq r_{cut} \\ 1, & \text{if } r_{ij} > r_{cut} \end{cases}. \quad (2.6)$$

The cut-off distance r_{cut} is the minimum distance between the atoms in the cluster, and in this case it is set equal to the first noticeable minimum of the pair-distance distribution function (PDDF) of each cluster.

The coordination number's precision can be expanded by considering the contributions from the second nearest neighbors: extending the information on the local structure can capture the structure sensitivity more accurately. This extension of the CN leads to the Generalized Coordination Number (GCN). For a reaction to happen, a molecule can interact and bind to the surface via an atop, bridge or hollow site. Atop sites are characteristic of a one-to-one relationship between the molecule and the metallic site, on bridge sites the molecule is anchored between two metallic atoms, and hollow sites involve three atoms on a (111) surface or four on a (100) surface. For a site i , GCN_i is calculated as the sum of the coordination number CN_j of each j nearest-neighbour of the underneath metallic atom, normalized with respect to the bulk coordination CN_{max} .

$$GCN_i = \sum_j \frac{CN_j}{CN_{max}}. \quad (2.7)$$

The bulk coordination number is equivalent to 12 in the case of an atop site on a face centered cubic lattice, it is 18 for a bridge site, 22 for a hollow site composed of three atoms and 24 for a hollow-four-atoms site. Since the CO₂ reduction reaction involves atop adsorption, in this study only atop sites and their atop Generalized Coordination Numbers (aGCNs) and their contribution to the chemical reaction are studied and taken into account. An algorithm which calculates the nearest neighbors' distances, and from then outputs the aGCN for each atom in the simulation for each time step is written, employing the Atomic Simulation Environment (ASE), and a package for large-scale molecular dynamics within it, the Atomic SimulAtion Program 3 (ASAP3) [60]. A column is added to the movie file containing all the

atoms' trajectories, in a way readable by Ovito, the open visualisation tool employed to visually analyze the results [61]. An example of characterization of a nanocluster in terms of its aGCN created with Ovito is represented in Figure 2.3, a perfectly ordered copper cluster composed of 585 atoms.

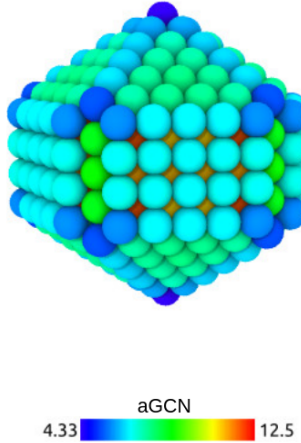


Figure 2.3: Visual representation of aGCN on a mDh (Cu_{585}). Low-coordinated sites are colored in blue, highly-coordinated, bulk-like sites in red.

The most highly coordinated sites are in the bulk, while the least coordinated sites are represented by the vertices.

It seems reasonable to assume, by reading Zhao et al. [32], that the sites which actively contribute to the activity of the cluster are the ones with a corresponding aGCN between 2 and 9. The assumption would be that highly uncoordinated atoms ($\text{aGCN} < 2$) are unlikely to appear in any structure, and the contribution to the free energy coming from atoms with an aGCN higher than 9 is negligible, because they are usually found in the bulk. An analysis is performed on all the Cu types to ensure this assumption is a reasonable one. The main outcomes are reported in Figure 2.4, created with the Primiplotter ASE package.

We conclude that the assumption of surface atoms corresponding to an atop GCN smaller than 9 is acceptable. The reaction free energy is therefore calculated using the same limits as the ones proposed by Zhao et al. [32].

Another descriptor used to determine NPs' geometries evolution is the common neighbor analysis (CNA), which is accomplished by examining the local connectivity

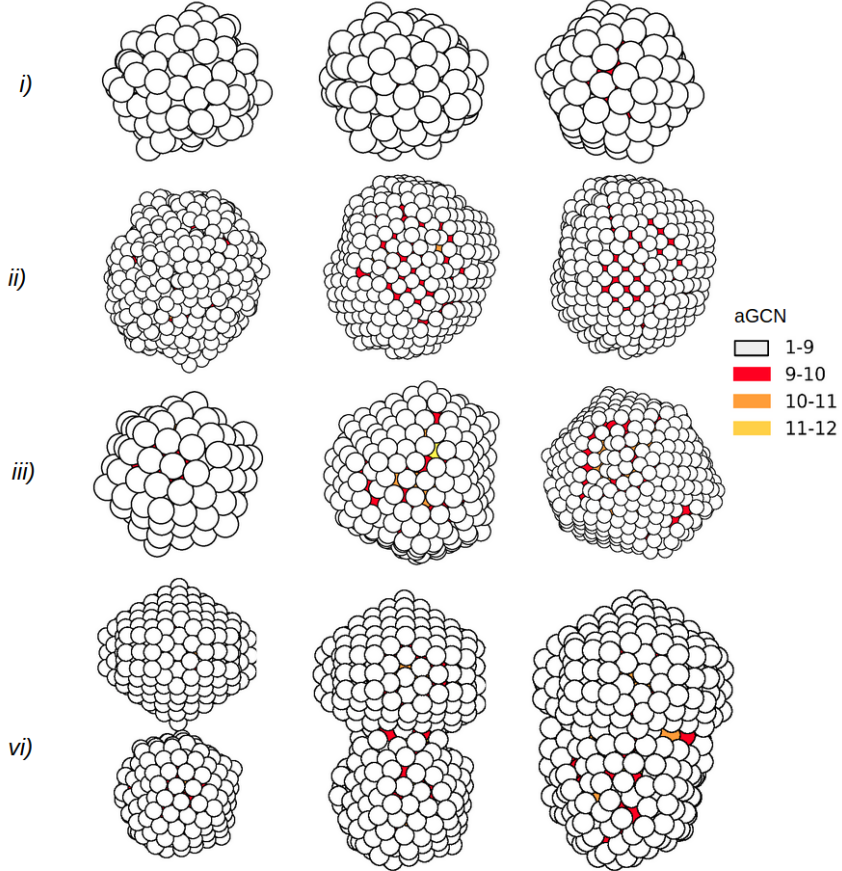


Figure 2.4: Snapshots at specific times (time evolution going left to right) are taken for *i)* a freezing of Cu₁₄₇, *ii)* a freezing of Cu₉₇₆, *iii)* a growth from Cu₁₄₇ to Cu₉₉₇, and *vi)* a coalescence of Cu₄₃₄+Cu₂₈₅. Atoms are colored according to their aGCN, to show that aGCN values between 2 and 9 belong to the NPs' surfaces.

of each pair of nearest neighbors (see Armand Auquier's MSci thesis [45]). Each pair is associated a specific signature: (jkl) , where j is the number of common nearest neighbors, calculated by looking at the first minimum of a pair distribution function, k is the number of bonds between the common nearest neighbors and l is the length of the longest chain between them [46]. The geometrical shape of both the bulk and the surface can be deduced by looking at these signatures. The structures outputted from each different process are categorised by looking at the CNA signatures into three main groups: FCC, Ih and Dh. The FCC identity group includes Oh and To. Some examples of how to interpret the CNA pattern are:

1. a (555) signature characterizes a five-fold symmetry axis, and will be therefore

abundant in an Ih structure. It will be in part present in a Dh NP as well, but should be absent in an ideal FCC.

2. (421) is the signature for an FCC environment, but it is always abundant in the bulk, and is therefore present in each structure.
3. a (422) symbolizes twinning planes and represents a grain boundary. It is therefore absent in an ideal FCC.
4. a (200) signature suggests the formation of square facets, and should be absent in an ideal Ih.
5. (100) is absent in an ideal Oh, but present in a To.
6. (111) and (311) signatures are representative of an FCC environment.

These rules are taken into account when dividing the final structures resulting from the freezing, growth and coalescence processes in groups (FCC, Ih or Dh). The structures are considered defected (dFCC, dIh, dDh) when less than 70% of the CNA pattern is not in line with the expected group's ideal geometry.

2.3.3 Catalytic Analysis

After having found the relationship between the geometric descriptor and the reaction free energy ΔG for the CO₂ limiting step, the NP's current density needs to be found in terms of ΔG , as in the NanoCHE model descriptor. The current is an important figure-of-merit to assess the reaction rate for electrochemical reactions. Because the current increases with increasing Cu electrode surface area, to make comparisons between electrodes, it is necessary to normalize the current using the surface area of the Cu electrode. Performing this normalization gives the current density, measured in mA/cm². The normalization is usually carried out in terms of the geometric surface area, resulting in j_{geom} , in terms of the electrochemical surface area, resulting in j_{ECSA} , or in terms on the nanocrystal surface areas, resulting in j_{NC} , as in [43]. Usually j_{geom} is a more practical metric as it is easily computed; however, j_{ECSA} is more representative of the true electrochemical system , although

its measurement is not trivial, and the reader is advised to read the review on this topic by Trasatti [62]. Typically, ECSA can be measured by double-layer capacitance measurements, hydrogen underpotential deposition measurements, or integration of cyclic voltammetric peaks [63, 64]. In this study, the current density produced by the NP is taken as a function of the geometric descriptor, and is calculated through Equation 2.2, already encountered when the NanoCHE model was first introduced. The current density j is measured at 300 K, since catalysis usually occurs at room temperature. The temperature used in the CMD simulations should be considered as a tool to accelerate rate events. The Maxwell-Boltzmann factor β is therefore equivalent to 38.68 eV. Low coordinated sites boost the free energy factor ΔG to a more negative value, immediately leading to a more negative current density - to a more active NP - , given the exponential form of Equation 2.2.

All the variables in Equation 2.2 can be found by writing a code which counts each aGCN occurrence, and calculates its corresponding ΔG through Equation 2.1. The current density is then calculated at each time step for an applied potential between -1.299 V and 0 V. The values are then summed over all aGCN signatures. The final information is contained in a 2-dimensional array, which contains a $N \times M$ array for each time step, N being the length of the i values in Equation 2.2(90 in our case, from 0 to 9 every 0.1), and M being the binning of the voltage(1299 in this study, to reach -1.299 V). For a better understanding, see the function ‘catalytic_activity’ in the appended Python script.

The most delicate task involves finding the constant C , which is obtained by solving some initial conditions, which are extracted from the work by Loiudice et al. [43]. By knowing that at an applied potential of -1.1 V the current density of a 63 nm cube is equivalent to -0.3 mA/cm², and by knowing the occurrence of specific aGCN values on that geometry, the constant is found to be $-1.53 \cdot 10^{12}$. The data for the aGCN occurrence for large cubes are taken from the PhD Thesis research project of K. Rossi and from the Msc Thesis project of H. Moerkved [65, 66]. A more detailed description of all the steps to reach this conclusion can be found in the next chapter.

Once the variation of the current density in terms of the applied potential is

found, the specific activity (SA), meaning the current density j at a specific applied potential U , can be easily found. It is then used to measure the mass activity (MA) of a cluster, which is calculated through Equation 2.8 by definition.

$$MA = \frac{SA \cdot A_{surf}}{M} , \quad (2.8)$$

where the mass M of an isomer equals the number of atoms in the nanoparticle times their atomic mass, i.e. 63.546 a.u. for Cu, while the surface area A_{surf} is assumed to be quantifiable as a function of the aGCN too. Within the approximation of atoms as spheres, the following expression can be utilized [67]:

$$A_{surf} = \sum_i^N 4\pi r_{atomic}^2 \left(1 - \frac{aGCN(i)}{12} \right) , \quad (2.9)$$

where the sum is over all atoms i in the nanoparticle, and r_{atomic} is the atomic radius of the particle, namely 0.128 nm for Cu. Within this approximation, the surface contribution from each atom is greater for low coordinated atoms than for highly coordinated ones, as expected from a geometric argument.

Results and Discussion

This section reports all the relevant results necessary to understand the concepts explored, to analyse the general trends, to make appropriate comparisons and to motivate research directions taken throughout the project. Considerations within each formation process are made (i.e. how the size and shape affect the NP activity), and the three procedures are compared, to see if they lead to more or less active NPs. The order follows the analysis steps outlined in the Analysis section above. All the following plots have been smoothed out with a Python one-dimensional Gaussian Filter, to present the results more cleanly.

3.1 Energy Considerations

The energetic behaviour of the NPs tells a lot about the nature of the process: a structure which have a lower excess energy is more energetically favourable, and therefore more likely to be observed in the natural world. It is already known how a structure born from coalescence will have a bigger excess energy than one born from growth, as explained in section 2.3.1. Once all the processes are run, it is evident that more ordered structures (mainly ones resulting from a freezing process) are the most energetically favourable ones. The discussion, supported by graphs, can be found below.

The initial structures for the freezing simulations are amorphous ones, deriving from a fast melting previously undergone by the NPs. Three different freezing rates are investigated to find out if the liquid-solid phase transition happens at all rates, and if it happens at different times. The excess energy evolution, averaged over the four simulations, can be seen in Figure 3.1.

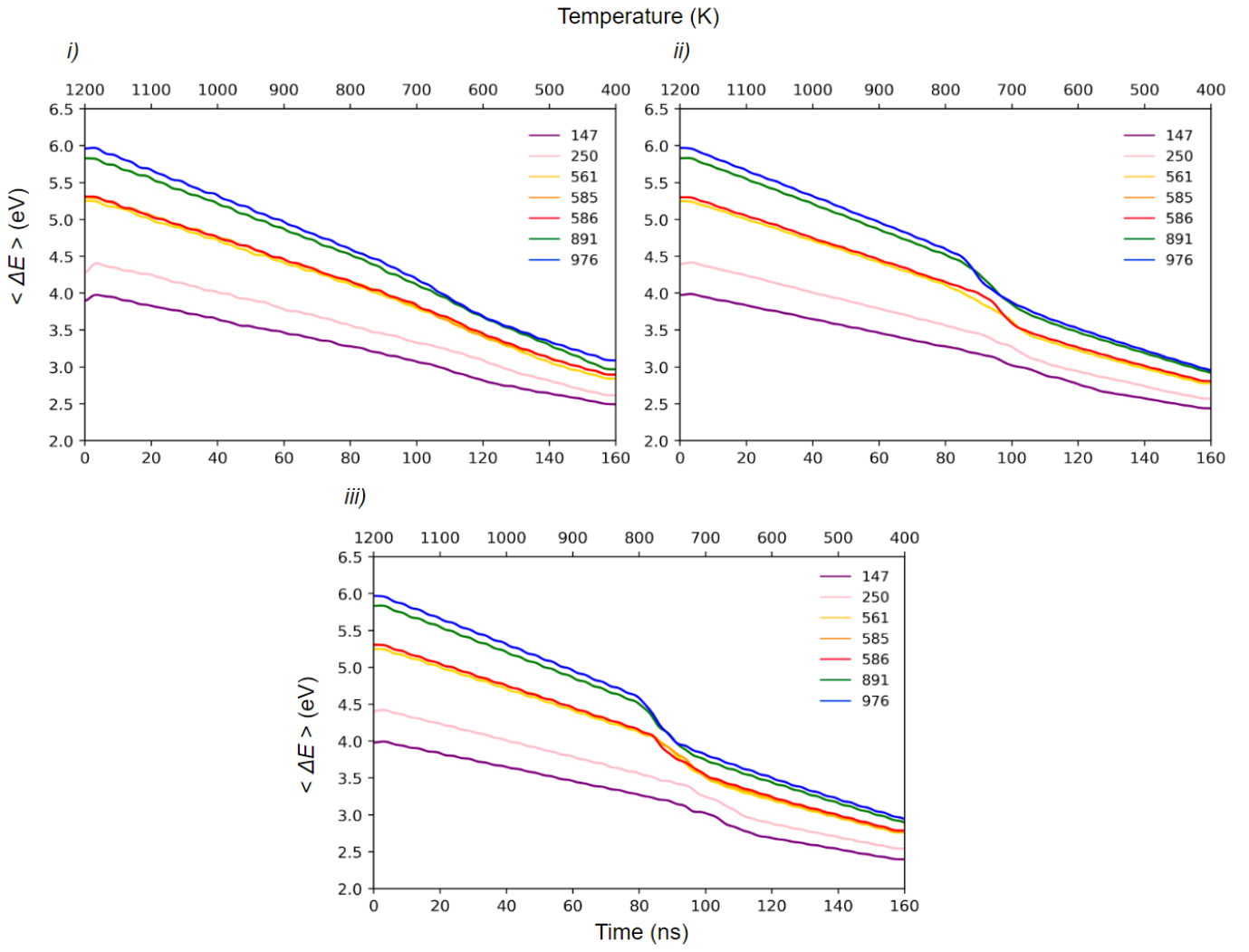


Figure 3.1: Excess energy development in freezing processes at a rate of *i*) 50 K/ns, *ii*) 10 K/ns and *iii*) 5 K/ns. The legend represents the number of atoms, namely the size of the NP.

The excess energy increases monotonically with the NP's size. The inflection point in the energy function identifies a phase transition: over a short time period, the excess energy is drastically lowered due to the structural change. The phase transition from liquid to solid is evident when the temperature is changed at a slow and medium rate, respectively 5 K/ns and 10 K/ns, but it does not happen when the rate is fast, leading to a disordered frozen NP. For smaller sizes, namely for Cu₁₄₇ and Cu₂₅₀, the structural transition is barely noticeable also at slower rates, especially for Cu₁₄₇ at 10 K/ns. The transition happens earlier in time the bigger the structure

is, and later in time the slower the rate is. The freezing temperature, useful for later calculations and representations, is agreed to be the temperature corresponding to the first inflection point, meaning when the gradient of the function first changes considerably. This point is found by using the rpy2 Python package [71] and by running a semi-machine learning algorithm on the energy function. The final excess energies $\langle \Delta E \rangle_{fin}$ of each structure for each freezing rate are reported in Table 3.1, to see which rate leads to a more energetically favourable structure.

Cu	rate	$\langle \Delta E \rangle_{fin}$ (eV)
147	f	2.50
	m	2.44
	s	2.40
205	f	2.61
	m	2.57
	s	2.54
561	f	2.84
	m	2.77
	s	2.76
585	f	2.90
	m	2.81
	s	2.77
586	f	2.90
	m	2.81
	s	2.79
891	f	2.97
	m	2.95
	s	2.92
976	f	3.08
	m	3.00
	s	2.98

Table 3.1: Table showing the final excess energy for fast (f), medium (m) and slow (s) rates.

As can be deduced, the slow rate always leads to a lower excess energy, meaning the final structures are more energetically favourable, and will then be kept for the later investigations. The four simulations for each structure at a slow freezing rate are displayed in Figure 3.2, to show how the phase transitions do not all happen at

the same time.

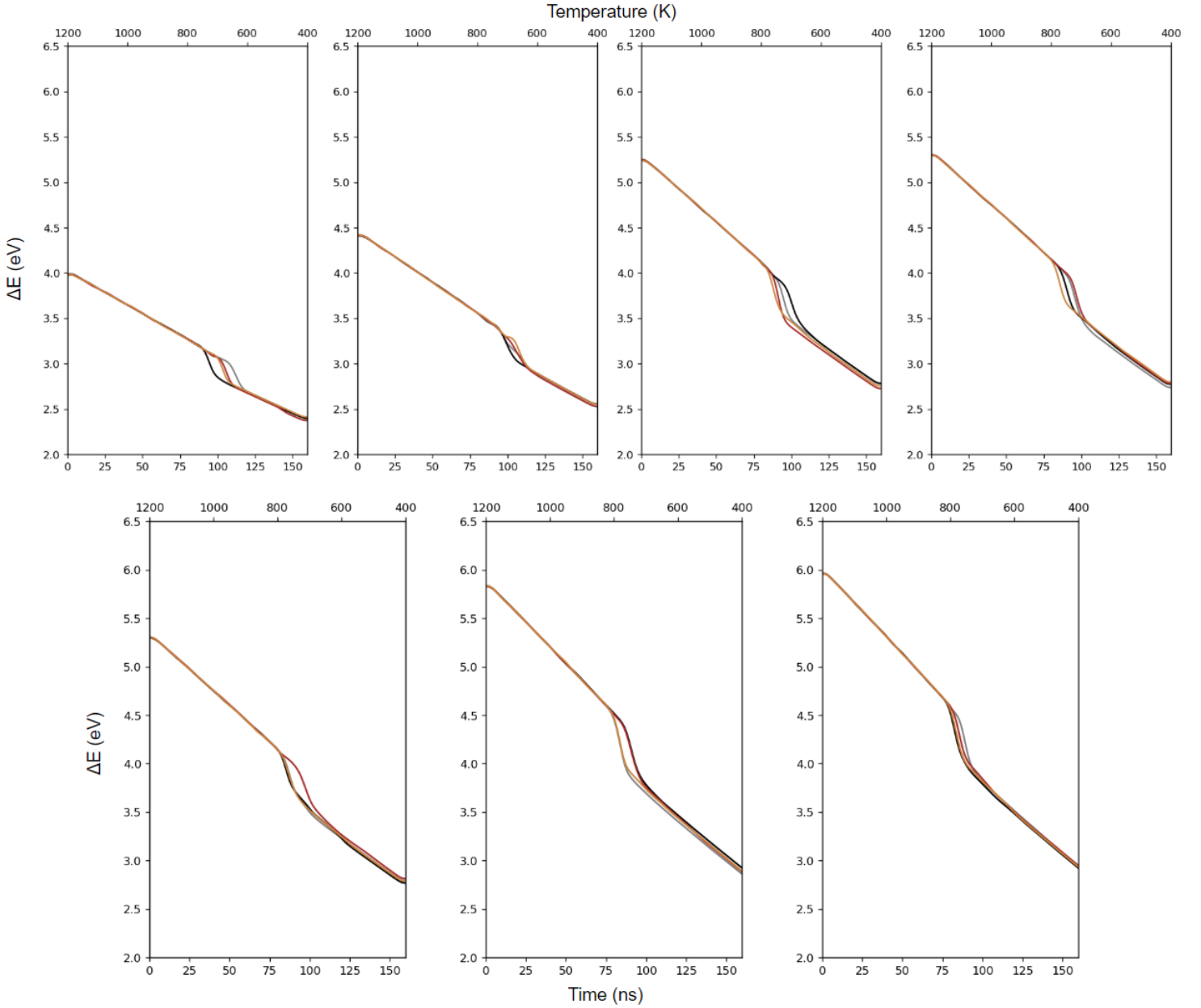


Figure 3.2: How initial random parameters affect structure formation in freezing processes (5 K/ns). From top left to bottom right: Cu_{147} , Cu_{250} , Cu_{561} , Cu_{585} , Cu_{586} , Cu_{891} , Cu_{976} . The different colors represent the four simulations run for each system.

Even if the transitions happen at different moments for each simulation within the same structure, the final excess energies are not very different. As a general trend, the structures which undergo a phase transition earlier are more likely to be

more energetically favourable, and therefore end up in a more ordered structure, as expected. For instance, in Cu₁₄₇ (Figure 3.2) the black line represents an earlier transition, and in fact the resulting structure is a defected Ih (dIh) structure, for Cu₅₆₁ the brown and orange lines also represent more ordered final structures, and so on. This concept is conveyed in the following Table 3.2, where the structures are grouped into Ih, FCC (To) and Dh by looking at the CNA pattern, some examples of which can be found in the Appendices.

N atoms	■	■	■	■
147	dIh	Ih	Ih	dIh
250	dIh	dIh	dIh	dIh
561	dFCC	dFCC	FCC	FCC
585	dIh	Ih	dIh	Ih
586	dFCC	FCC	dFCC	FCC
891	Dh	dDh	dDh	Dh
976	dFCC	FCC	dFCC	FCC

Table 3.2: Outcomes of different structure processes during slow freezing depending on the initial condition. dFCC, dIh and dDh are defected structures, meaning their CNA pattern is up to 70% identical to the one corresponding to a perfectly ordered geometry of that kind.

As the excess energy increases when the structures are liquid because more cohesive energy is required to keep them together, for the same reason ΔE grows as structures get bigger. In growth processes , where more than 800 atoms are added to the core NP, the resulting structures are always defected, presenting extended uniform (111) and (100) facets. In order to investigate growth processes in an appropriate way, three different structures belonging to different geometrical groups are taken as a starting point. The following Figure 3.3 displays all the simulations performed.

When the initial structure is an Oh (Cu₁₄₆), the energy seems to drop in three out of four cases, to then keep on increasing until a structure with 996 atoms is reached;

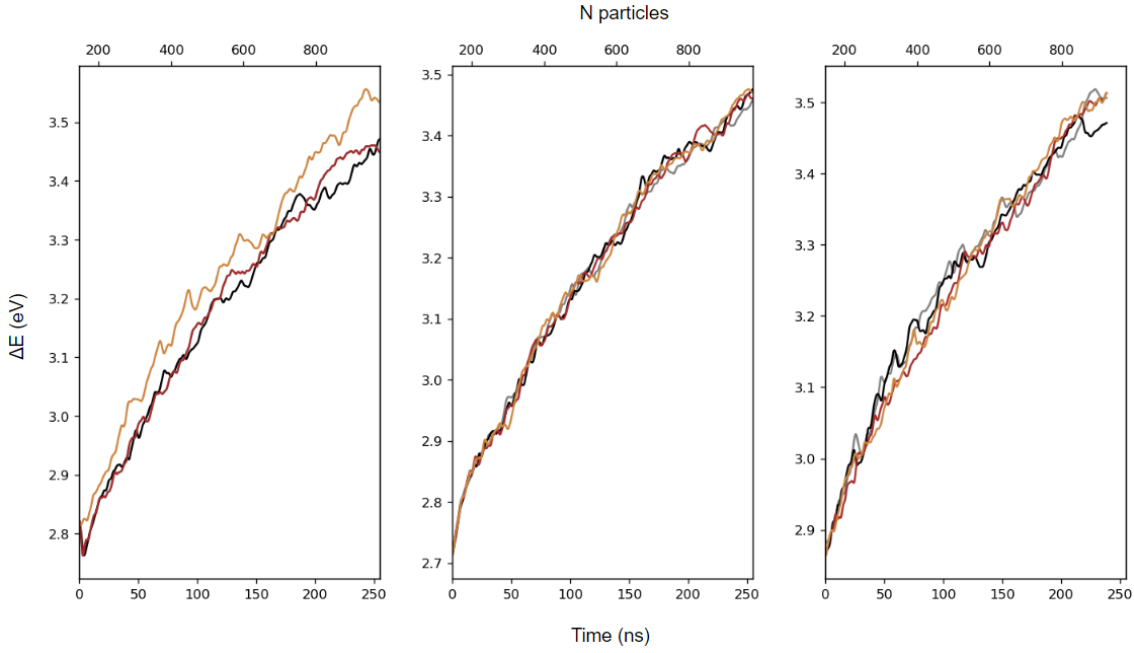


Figure 3.3: How initial random parameters affect structure formation in a growth process. From left to right, initial structures are Cu_{146} , Cu_{147} , Cu_{201} . The different colors represent the four simulations run for each system.

only one of the simulations does not follow this behaviour, and its final excess energy is considerably greater. The Ih (Cu_{147}) follows a comparable behaviour in all four simulations, while the To (Cu_{201}) behaves differently only one time (black line) towards the end. This exception contributes to lowering the energy of the averaged excess energy, $\langle \Delta E \rangle$. The following Table 3.3 analyses the structure geometry evolution following the same procedure described for the freezing. Only specific sizes are taken into account for simplicity.

Again, the more ordered the structure, the lower its excess energy. It is interesting to notice that the orange line in the first plot of Figure 3.3, the one corresponding to the evolution of an Oh, is much less energetically stable: this structure evolution, in fact, ends up in a disordered FCC structure, while the other ones form dIh, which seem to be the most energetically stable structures for the growth processes in general, as can be seen in Figure 3.4, where the average excess energy is plotted as a function of time and of number of atoms composing the NP.

One may observe from Figure 3.4 that the Ih structure is the most energetically

NP initial geometry	N atoms				
Oh	250	dFCC	dIh	dIh	dFCC
	561	dFCC	dIh	dIh	dFCC
	719	dFCC	dIh	Ih	dFCC
	976	dFCC	dIh	dIh	dFCC
Ih	250	Ih	Ih	Ih	Ih
	561	Ih	dIh	Ih	Ih
	719	dIh	dIh	dIh	dIh
	976	dIh	dIh	dIh	Ih
FCC	250	dFCC	dFCC	dFCC	dFCC
	561	dFCC	dFCC	dDh	dFCC
	719	dFCC	dFCC	dDh	dFCC
	976	dFCC	dFCC	dDh	dFCC

Table 3.3: Outcomes of different structure processes during slow freezing depending on the initial condition. dFCC, dIh and dDh are defected structures, meaning their CNA pattern is up to 70% identical to the one corresponding to a perfectly ordered geometry of that kind.

favourable one throughout the whole size range, apart from a limited amount of time for sizes between 650 and 700 atoms, where it is outclassed by the Oh one, probably due to a finite sample effect. The FCC remains the least favourable one for the whole simulation.

When freezing and growth processes are compared over the same sizes and at the same temperature of 600 K, it is found that grown structures are more energetically favourable than frozen ones, since they are allowed more time to stabilize. For example, for a structure of 891 atoms (Oh), the freezing process leads to an excess energy of 3.6 eV at 600 K, while a grown Oh structure presents an excess energy of about 3.4 eV. An Ih Cu₅₆₁ frozen at 600 K has an excess energy of 3.4 eV, while a grown Ih presents an excess energy of 3.2 eV when grown to 561 atoms. The difference is less noticeable for smaller particles, since they are closer to the very

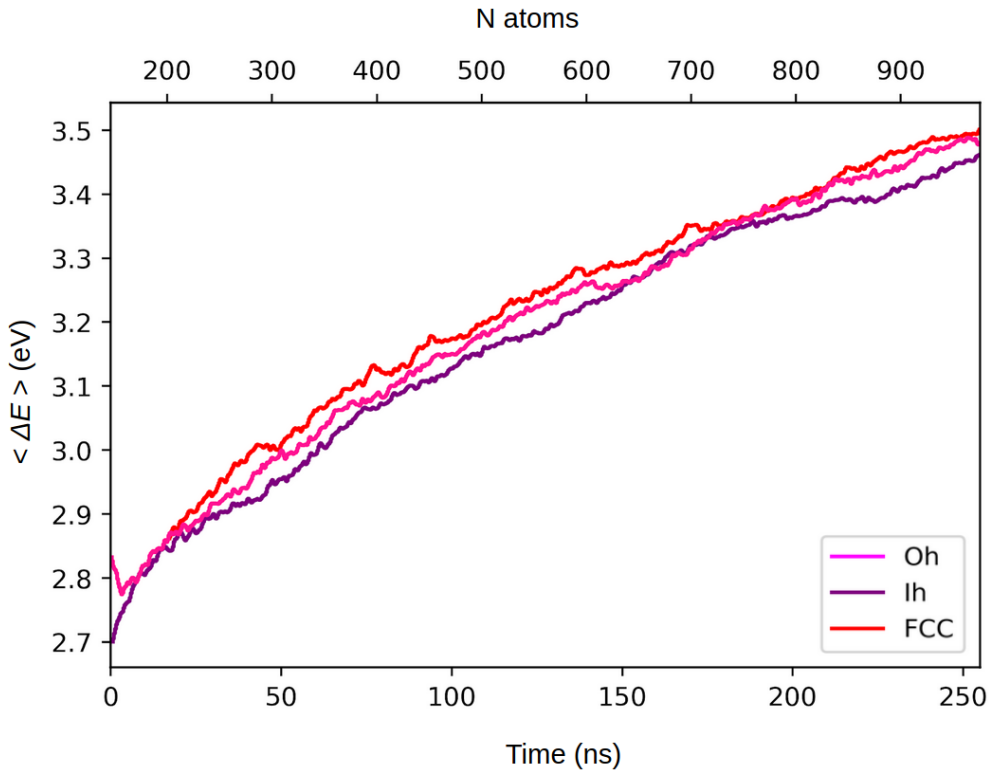


Figure 3.4: Excess energy evolution in growth processes.

beginning of the growth evolution. The Ih is usually more energetically favourable, as it maintains its shape and grows layer by layer; however, the Oh's excess energy drops down to the Ih values at sizes of around 160 atoms and between 600 and 700 atoms.

As already stated, NPs resulting from a coalescence process will be less energetically favourable than grown ones. An investigation is performed to see if this is the case with respect to frozen structures as well. The following Figure 3.5 depicts the coalescence simulations performed.

Apart from random fluctuations which distinguish the four simulations for each case, which are more noticeable because the time range is shorter, the trend is that the structures have the maximum excess energy at the beginning of the simulation, when they are at a distance apart. This consideration makes sense in light of the fact that the structures taken into account by the energy calculators are two, and the corresponding ΔE s are added together. The collision happens in all cases very early in the simulation process. With the exception of the small structure ($\text{Cu}_{110} + \text{Cu}_{130}$),

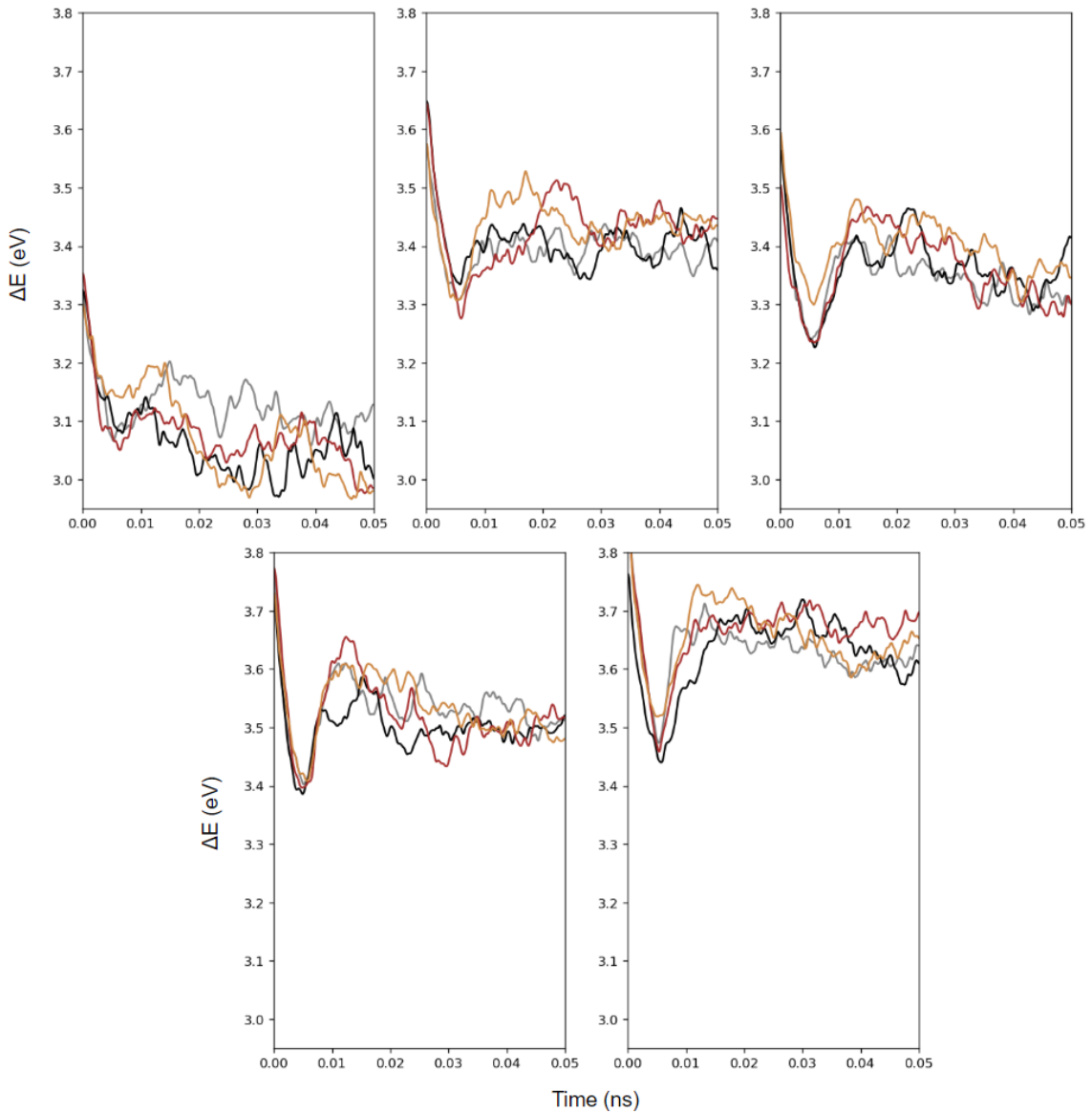


Figure 3.5: How initial random parameters affect structure formation in coalescence processes. From top left to bottom right: Cu₂₄₀, Cu₅₂₀, Cu₅₈₁, Cu₇₁₉, Cu₈₃₉. The different colors represent the four simulations run for each system.

all the other ones reach a minimum energy when they collide, since the system is at its lowest potential energy state. After the collision the excess energy is risen again, but it never reaches the starting energy, since there is only one elongated structure.

A CNA analysis is performed on the final structures as in the previous processes, in order to individuate their geometries. The results are displayed in Table 3.4

Again, it is observed how a more ordered geometry leads to lower excess energies.

N atoms	■	■	■	■
240	amorphous	amorphous	dIh	dIh
520	amorphous	dDh	amorphous	amorphous
581	dDh	dDh	amorphous	amorphous
719	amorphous	amorphous	amorphous	dDh
839	dDh	dDh	dFCC	dFCC

Table 3.4: Outcomes of different structure processes during coalescence depending on the initial condition. dFCC, dIh and dDh are defected structures, meaning their CNA pattern is up to 70% identical to the one corresponding to a perfectly ordered geometry of that kind. Amorphous structures do not present any kind of geometry.

In Cu₂₄₀, for instance, the last two simulations (brown and orange lines in Figure 3.5) end up with a lower excess energy, therefore resulting in somehow more ordered structures (they are still very defected, but their geometry could be associated to a defected Ih). For Cu₈₃₉ it is remarkable to see how the final excess energy is lower when the mDh remains unchanged, and the To becomes more disordered. On the contrary, the structure is the least energetically favourable when its geometry resembles a To, where the mDh bends off from the symmetry axes and starts merging into the side of the To.

The average energy $\langle \Delta E \rangle$ of the coalescence processes is given in Figure 3.6.

It is seen how when two structures of around 100 atoms collide the excess energy keeps being lowered even after the collision. Another feature to be noticed in Figure 3.6 is that Cu₂₇₀+Cu₂₅₀ makes up to 520 atoms, while Cu₁₄₇+Cu₄₃₄ to 581 atoms; however, the latter seems to have a lower excess energy from the very beginning. This is due to the fact that, as seen in freezing processes, more ordered structures have a lower excess energy. The initial Cu₄₃₄ is a mDh, while both Cu₂₇₀ and Cu₂₅₀ are dIh, deriving from a basin hopping procedure, and therefore with a higher initial excess energy, even if smaller in size.

The excess energies of the final structures resulting from the coalescence process are similar to the frozen NPs at 600 K.

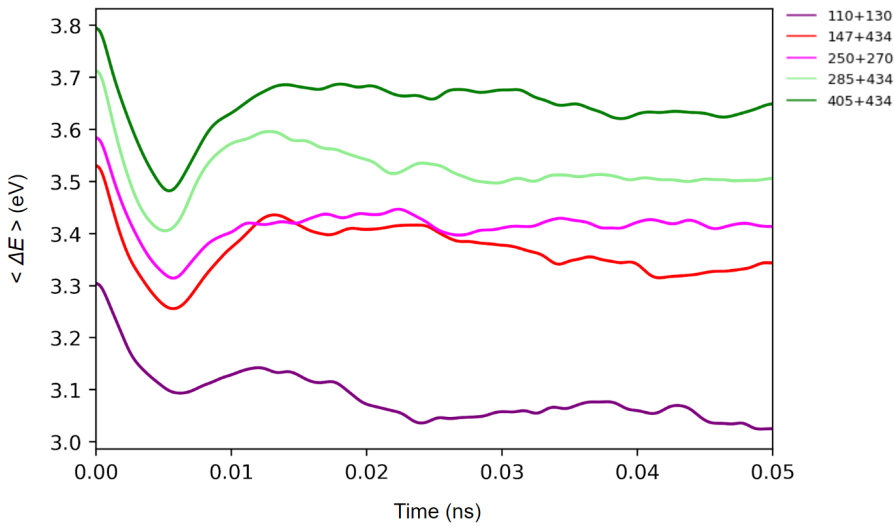


Figure 3.6: Excess energy evolution in coalescence processes.

However, if the final structures for each process are taken into account, it is found that frozen, ordered structures resulting from a freezing (if brought to 400 K) are the most energetically favourable ones, followed by the grown ones, and finally, by the collided ones.

The results in the next sections are averaged over the four simulations as stated in the previous sections, but the most energetically favourable ones are employed when NPs representations are required, since they are the most likely to happen in nature.

3.2 atop Generalized Coordination Number

Once the most energetically favourable structures are found, a python algorithm - found in the Appendices - is written to calculate the NPs' coordination. It reads the .xyz movie file generated by LoDiS, and for every time step it calculates the aGCN of each atom constituting the NP.

3.2.1 Discrete Histograms

From plotting histograms of the atop Generalised Coordination Number distribution at the initial, middle and final time steps the 'genome' evolution can be pinned

through its most important moments. Some features need to be remembered when analysing the histograms. An aGCN of 3.1 corresponds to the highest CO₂ reduction activity, followed by all the aGCN around this value. As discovered by Zhao et al. [32], an aGCN of 5.5 corresponds to (211) surfaces, one of 6.67 to (100) surfaces, and one of 7.5 to (111) surfaces. An aGCN higher than 8 usually corresponds to rientrances on the surface. Only aGNCs above 2 and below 9 are reported, in order to be consistent with the experimental values we are referring to. The first process to be analyzed is the freezing of clusters from a liquid to a solid phase. The seven different cases for each size analysed are displayed in Figure 3.7.

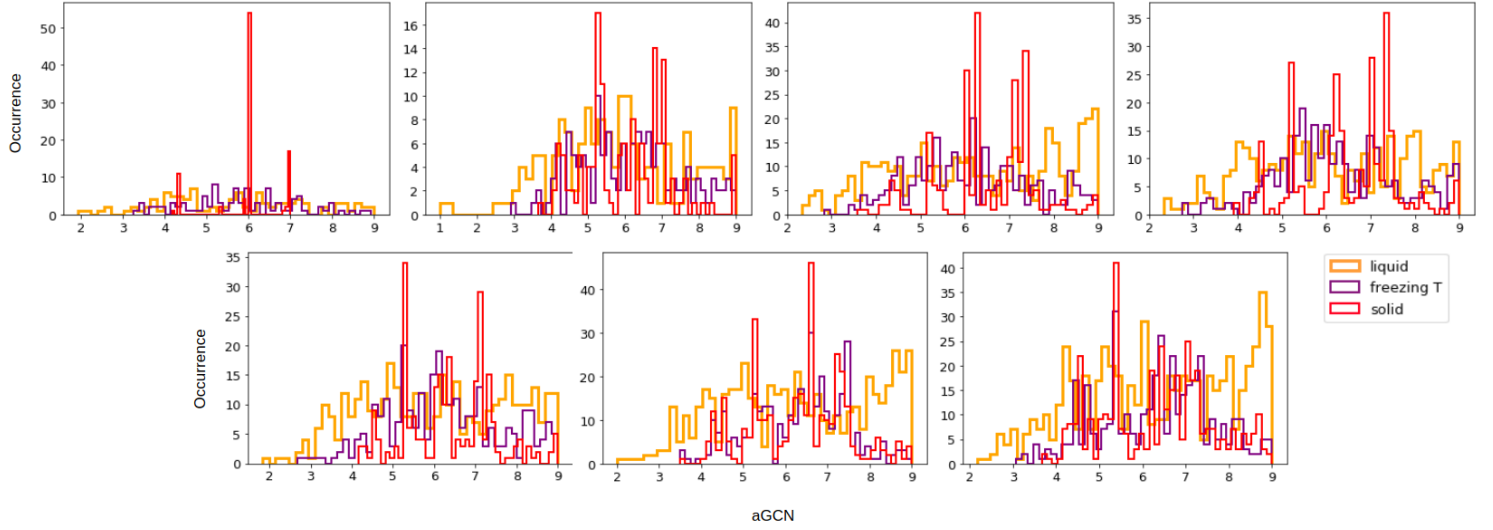


Figure 3.7: aGCN occurrence in freezing processes. From top left to bottom right: Cu₁₄₇, Cu₂₅₀, Cu₅₆₁, Cu₅₈₅, Cu₅₈₆, Cu₈₉₁, Cu₉₇₆. The label colors represent different time steps of the simulation.

In all cases, the aGCN distribution is more widely spread for liquid structures - as the yellow lines demonstrate - and it narrows down to specific signatures with the decreasing of temperature. The distribution at the freezing temperature - represented by the purple lines - already starts concentrating around the central values. For all sizes, it can be seen how aGCNs from 1 to 3 are more likely to happen in a liquid structure than in a solid one. This makes sense in light of the fact that liquid structures are more disordered, thus less coordinated. It can be noticed how Cu₁₄₇, being a small structure, has the time to significantly change over the freezing period,

reaching an aGCN distribution with steep peaks at around 4.3, 6 and 7. The frozen structure does not present any aGCN smaller than 4, hence we expect a structure which is not particularly active. Cu_{250} , being an opened structure, presents a less defined difference between the liquid and the solid phase, but it is still evident how the yellow lines at an aGCN distribution of 1, 2 and 3 will massively contribute to the activity of the liquid cluster. The solid structure presents peaks at around 5.5 and 7, meaning the NP will have an abundance of (211) facets. Cu_{561} , Cu_{585} and Cu_{586} all have similar behaviours, in the sense of a liquid structures with an abundance of low coordinated sites and a solid one with aGCN peaks at around 5.5, 6.5 and 7.5, meaning the structure will become more ordered, with (211), (100) and (111) surface facets. The aGCN distribution for both Cu_{891} and CU_{976} shows a high occurrence of aGCN between 8 and 9, due to their bigger sizes, and therefore to the higher likelihood of finding surface rientrances and imperfections. They will both be more active in the liquid phase, with a frozen structures with peaks at an aGCN around 6.7 for Cu_{891} and 5.5 for CU_{976} .

The coordination number distribution for grown structures is depicted in Figure 3.8.

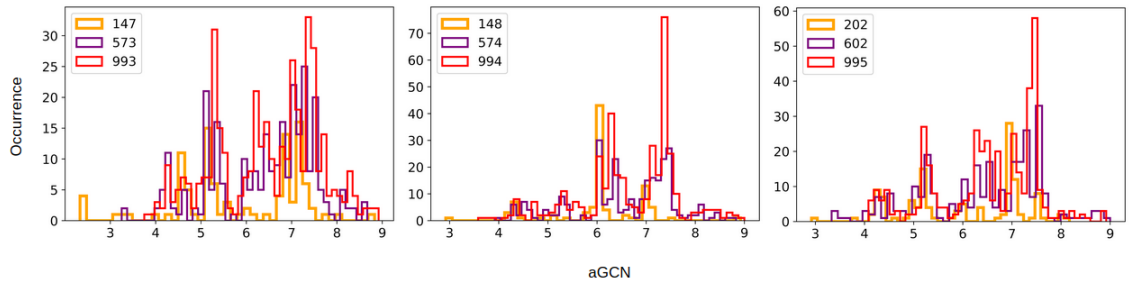


Figure 3.8: aGCN occurrence in growth processes. From left to right, the initial geometries are To, Ih and FCC. The label colors represent different time steps of the simulation, and therefore different number of atoms in the cluster.

The initial structures - yellow lines - present a higher occurrence of low coordinated sites, in favour of the idea that smaller NPs' surfaces produce a higher current density, as supported by A. Loiudice et al. [43]. Since three initial geometries are investigated, it is interesting to see how the initial geometry does not massively affect

the genome's evolution. The smaller structures present more low-coordinated sites, and the bigger structures have an aGCN occurrence with peaks at around 7.5, 6. 5 and 7.5. The To structure's distribution, starting form 147 atoms, is more spread, while the other two have pronounced peaks at around 7.5, indicating (111) surfaces. Focusing on the final structures - red lines -, it seems like the Ih NP's evolution would lead to a more active surface, since the lower-coordinated sites seem to happen with more frequency. When comparing the growth and freezing processes, it is observed how liquid small structures present an aGCN occurrence of low coordinated sites comparable to the grown structures; however, once they are frozen their small-aGCN occurrence drops, and grown structures seem to be more promising in terms of activity. When bigger sizes are taken into consideration, it is noticed how both liquid and frozen NPs seem to have fewer low-coordinated sites than the grown ones (red lines in Figure 3.8 and last histograms in Figure 3.7).

The last process to be analyzed is the coalescence. Its aGCN distribution is represented in Figure 3.9.

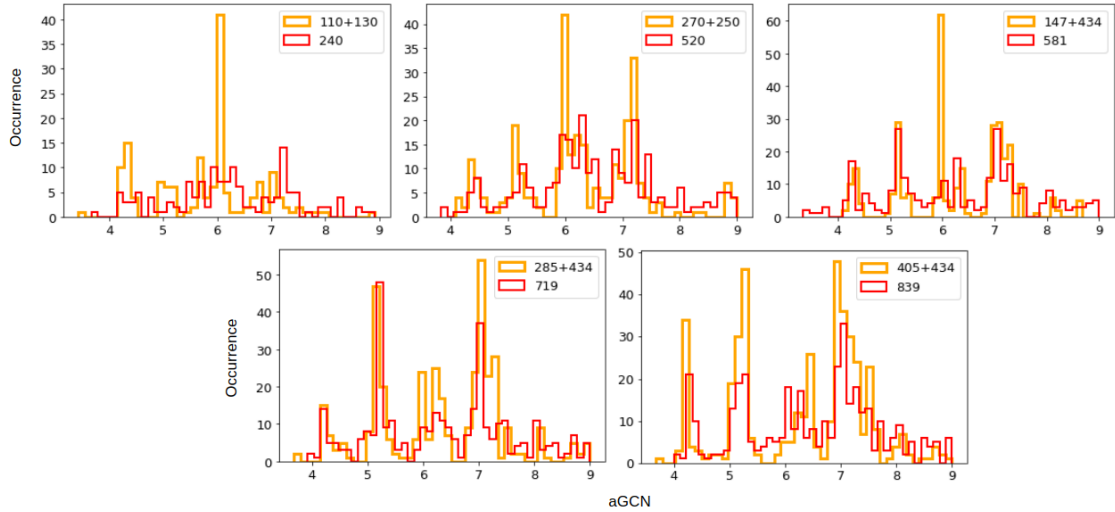


Figure 3.9: aGCN occurrence in coalescence processes. The label colors represent different time steps of the simulation

It can be seen how the initial, separated structures present more peaks at around 5.5, 6 and 7.5, being more ordered structures with (211), (100) and (111) facets. For the smallest system and for the two biggest ones, when the structures are separated

the lower-coordinated sites are more abundant than in the collided structures, leading to a higher system's current density. As concerns $\text{Cu}_{270} + \text{Cu}_{250}$ and $\text{Cu}_{147} + \text{Cu}_{434}$, it seems like the distribution does not present considerable differences, and it could be that the final structures will have a higher current densities.

A 3D graph is plotted to compare the aGCN distribution evolution for the three different processes, over different size ranges. Different sizes during the freezing process at 600 K are compared to the grown NPs, and to the collision of two NPs. The plot can be seen in Figure 3.10.

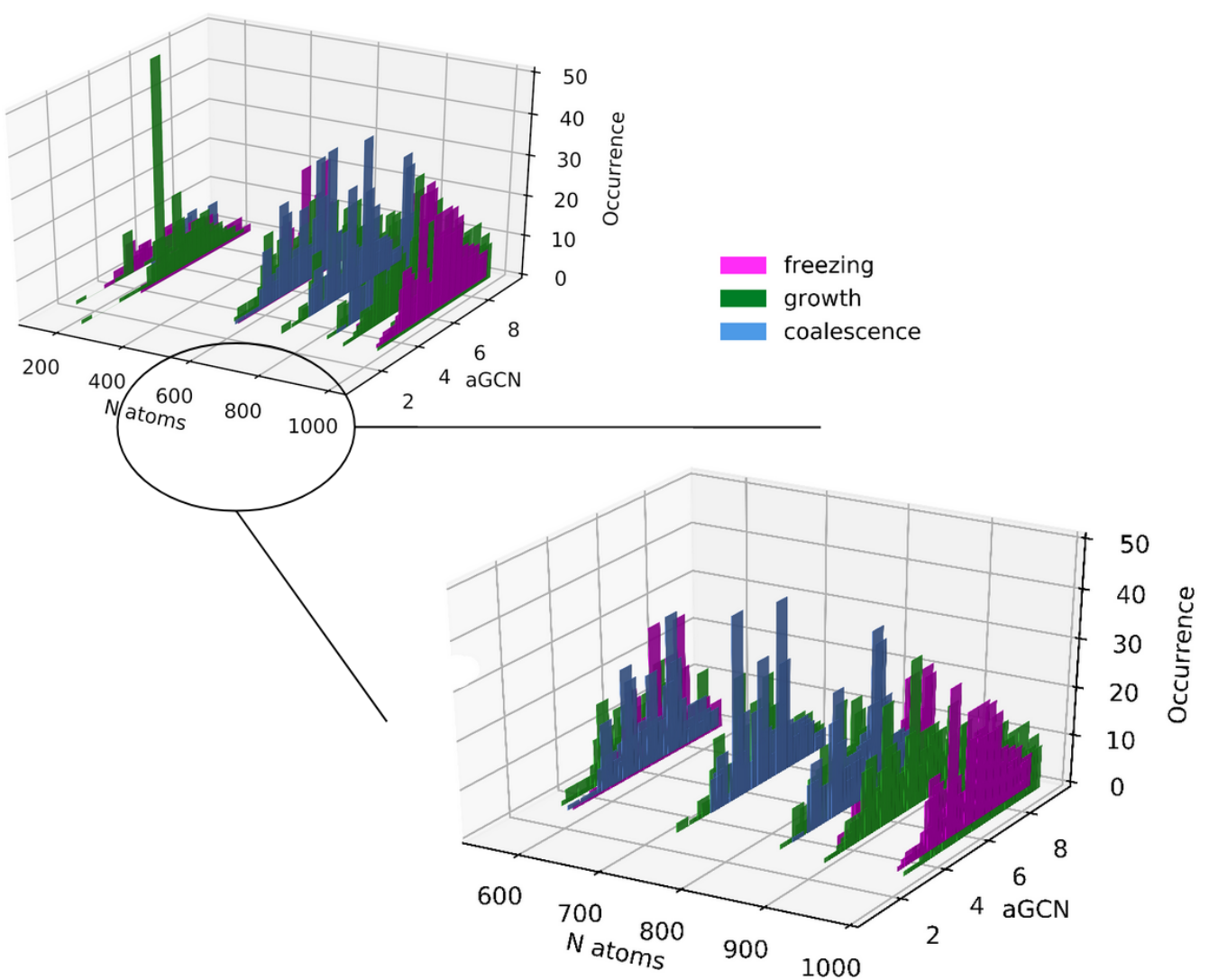


Figure 3.10: aGCN occurrence at 600K for different processes (■ freezing, ■ growth and ■ coalescence) and different cluster dimensions.

The spike for the growth of small NPs stands out over all the others, correspond-

ing to the Ih structure. It can also be noticed how, at 600 K, the growth process seems to be the most favourable one for smaller structures in terms of current density, since the occurrence of sites with aGCN around 2 is evident. The 3D plot is zoomed in to better scrutinize the bigger structures.

The growth process still leads to structures with smaller aGCN values at 600 K. For structures of around 500 atoms, the aGCN occurrence at around 3.1 is higher for the growth than for the freezing or coalescence. Instead, spikes of around 7.5 are more pronounced in the latter processes, since the structures are more ordered, especially the frozen ones. The same happens for greater NP sizes, where the collided structures (resulting from coalescence) are more ordered than the grown ones. The genome distribution is comparable for the frozen Cu₉₇₆ and for the Oh grown to around the same size, especially for the distribution of the low-coordinated sites.

3.2.2 Visual Representations

In the previous sections, snapshots of the aGCN distributions were taken, leading to a discrete analysis of the results at phase transition and collision moments. To extend the coordination number analysis, Ovito [61] is used to visualize the clusters' geometry evolution and to read the updated movie file with the aGCN information of each atom. Moreover, a more continuous analysis is performed on the aGCN evolution, namely the occurrence is plotted for each time step, for each genome value. The results are the heat maps depicted in Figures 3.11, 3.12 and 3.13.

The phase transition is noticeable on the plots, being the moment in which the aGCN occurrence, normalized in this case, stabilises on specific values. In the liquid phase the occurrence is much more spread, and it is hard to identify specific signatures. The aGCN legend is displayed in Figure 3.13, and it takes into account values between 2 and 9, as explained before. Three snapshots of each size are taken at three different times: at 0 ns, when the structure is liquid, at the time corresponding to the freezing temperature (which varies according to the size), and at 160 ns, when the structure is frozen. The liquid initial structures present more low-coordinated sites, coloured in blue. Cu₁₄₇ especially, being a small structure, is expected to be very active in its liquid phase, being its surface prevalently low-coordinated. It is

surprising how the simulation time is sufficient to bring it to a perfect Ih, which was the original geometry used at the very beginning of the process (when the NP was melted quickly), and the formation it can be found in nature at.

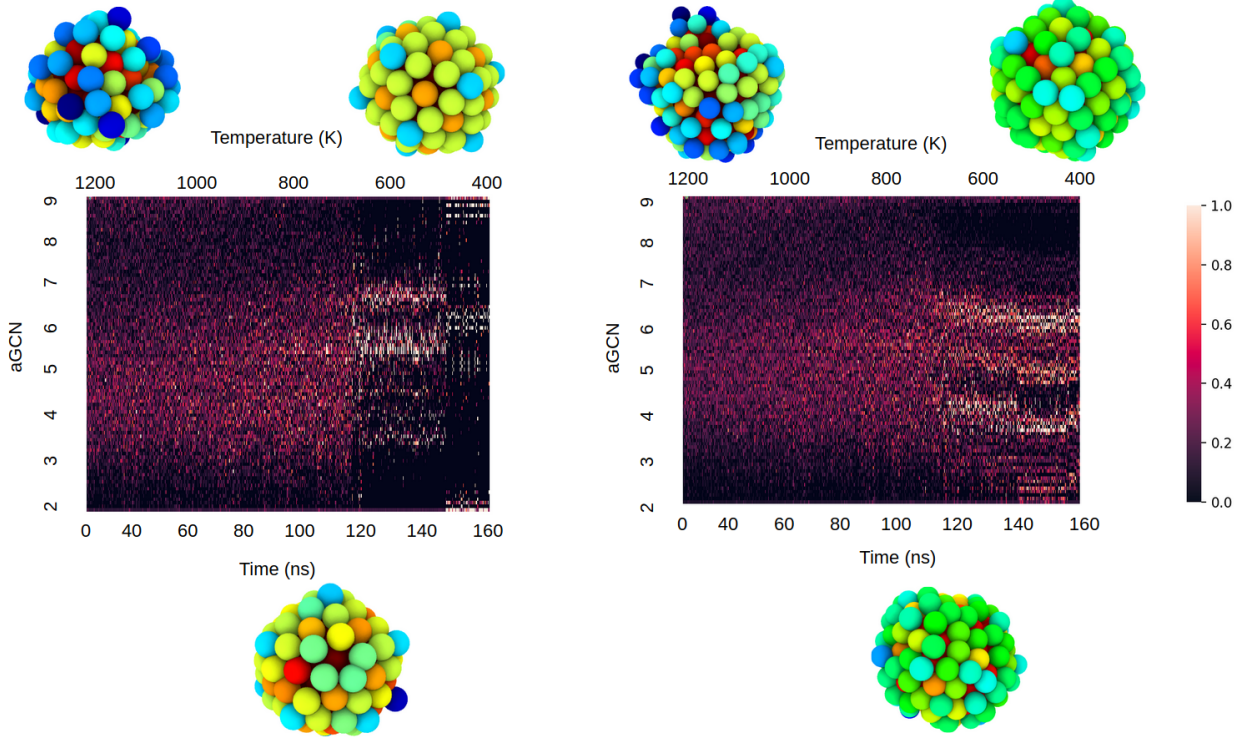


Figure 3.11: aGCN occurrence time evolution in the freezing of Cu₁₄₇ (left) and Cu₂₅₀ (right). Figures' snapshots are taken at 0 ns, 160 ns and at the time corresponding to the freezing temperature.

All the bigger NPs follow the same trend, with bigger structures becoming more ordered towards the end of the simulation. Cu₅₆₁ and Cu₅₈₆ evolve towards FCC geometries, Cu₅₈₅ in an Ih, Cu₈₉₁ in a dDh, and Cu₉₇₆'s frozen structure resembles a To.

A similar analysis is performed on the growth processes. The aGCN distribution does not seem to change considerably between the three initial geometries, as expected from the histogram analysis. The genome distribution is more uniform for smaller structures, expected therefore to produce a stronger current density; it evolves towards specific signatures as the size grows, with peaks in the occurrence at values of around 7.5, corresponding to (111) facets. The structure geometries at time frames of 0 ns, 125 ns and 250 ns are taken: the initial geometries are perfect

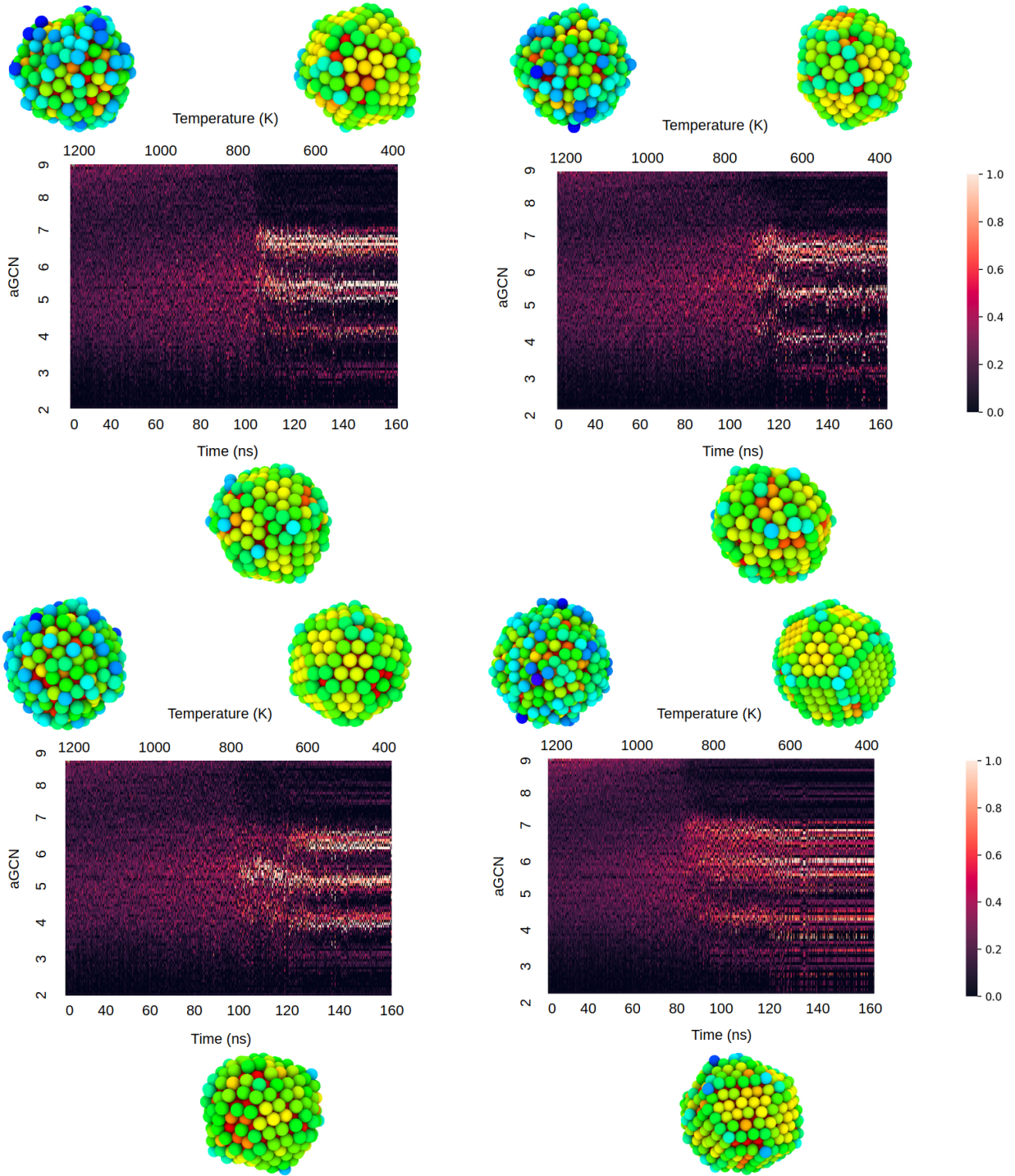


Figure 3.12: aGCN occurrence time evolution in the freezing of Cu₅₆₁ (top left), Cu₅₈₅ (top right), Cu₅₈₆ (bottom left) and Cu₈₉₁ (bottom right). Figures' snapshots are taken at 0 ns, 160 ns and at the time corresponding to the freezing temperature.

structures. The evolution is very different for the Ih case, which resembles the same

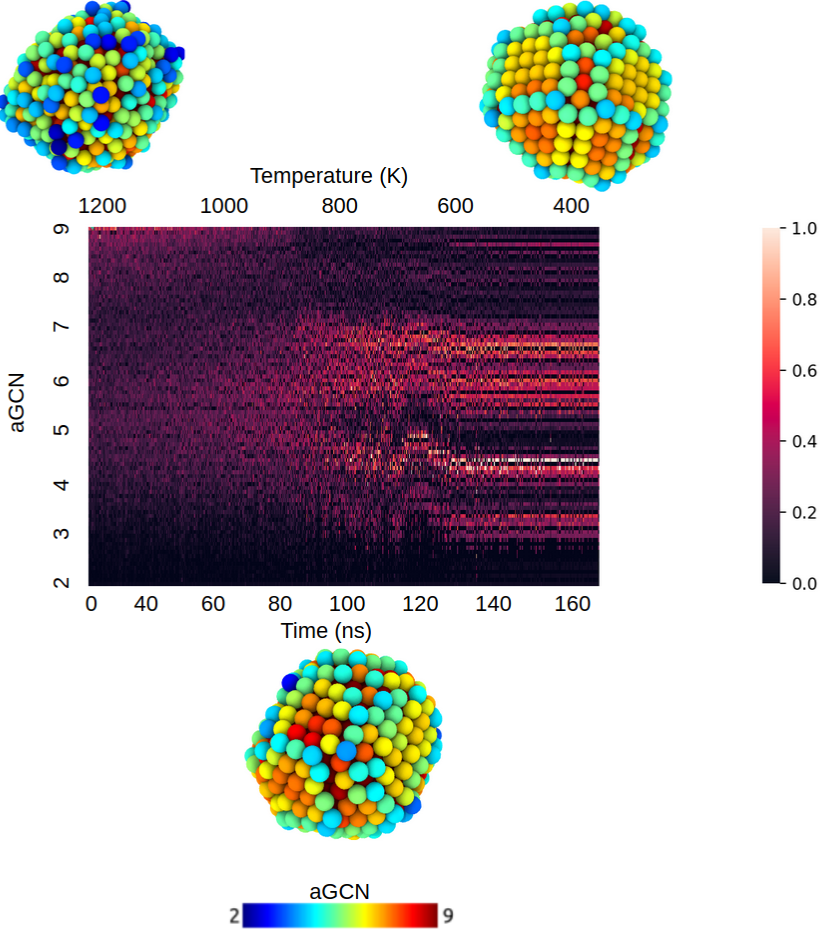


Figure 3.13: aGCN occurrence time evolution in the freezing of Cu₉₇₆. Figure's snapshots are taken at 0 ns, 160 ns and at the time corresponding to the freezing temperature.

geometry all the way throughout the simulation, ending up in an Ih Cu₉₉₇. Both the Oh and the FCC evolve in structures with many (111), (100) and (211) facets with undefinable shapes: the ones coming from the Oh evolution seem to exhibit triangular facets, while the To evolution ones are hexagonal, as expected. In their final configuration, the NPs do not present many low-coordinated sites.

The evolution of the aGCN occurrence when the structures are collided can be seen in Figures 3.15, 3.16 and 3.17. Snapshots are taken at the initial time, at the collision time (usually around 0.01 ns), and at the final time, corresponding to 0.05 ns. Before the two distinct structures collide, the system is made up of two ordered structures, so the aGCN occurrence presents spikes typical of a solid structure. At

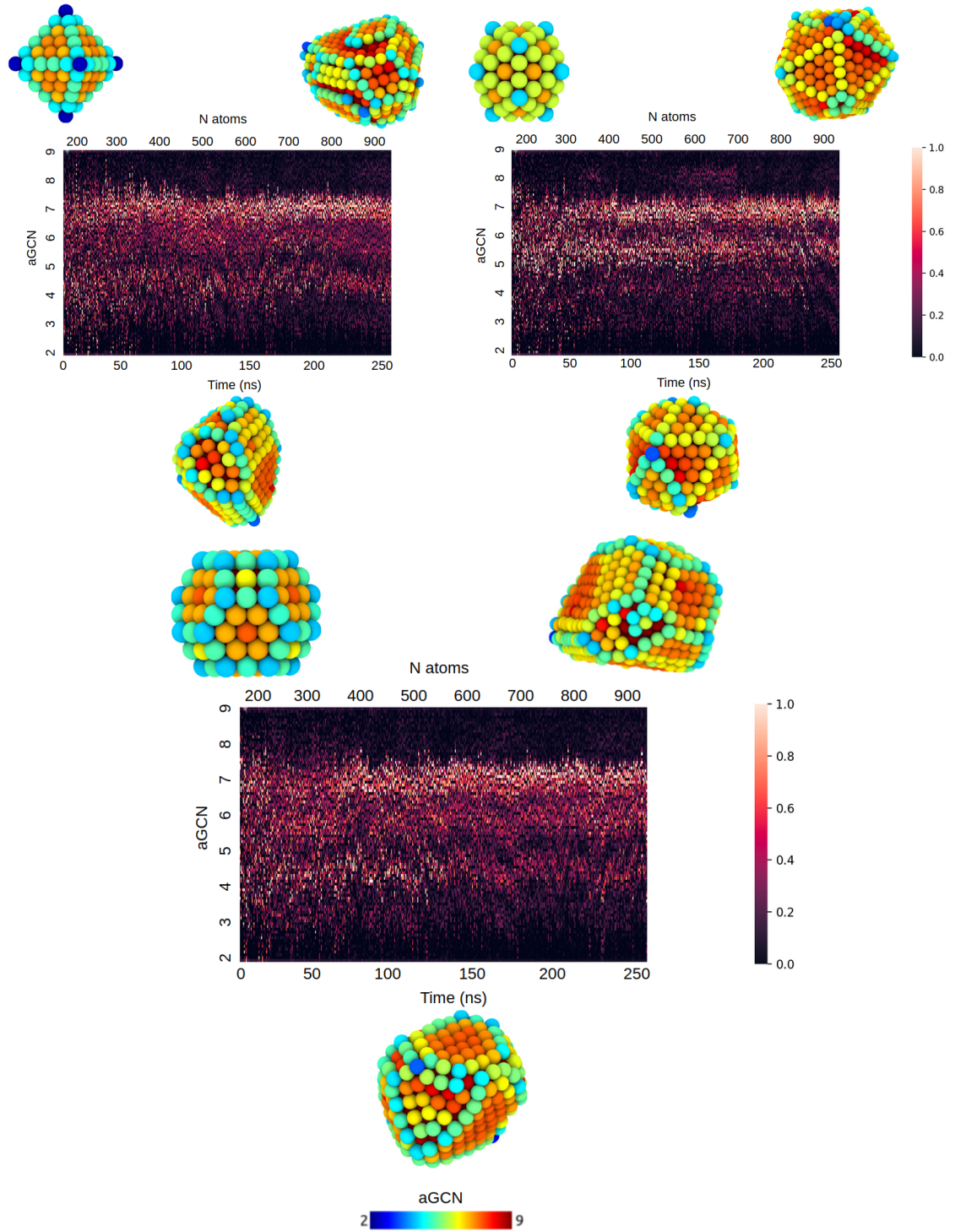


Figure 3.14: aGCN occurrence time evolution in growth processes. From top left, the evolution of an Oh, of an Ih and of a To (FCC). Snapshots of the structure are taken at three different moments (0 ns, 125 ns, 250 ns) for each process.

the moment of collision, the distribution changes considerably, and is indicative of a highly defected or amorphous structure in most cases. The simulations are run for a time too short for the structures to completely merge together; however, it is interesting to notice how the neck generated by the first moment of the collision is always very high coordinated, represented by the atoms colored in red in Figures 3.15, 3.16 and 3.17. The occurrence after the collision is very disordered and spread out, but it still shows some preferred aGCN values, more visible than in the growth evolution. Such values are around 5 and 6.5, coming from the part of the structure which are still not affected by the collision.

Some snapshots of structures resulting from different processes at various sizes are displayed in Figure 3.18 in order to perform useful comparisons.

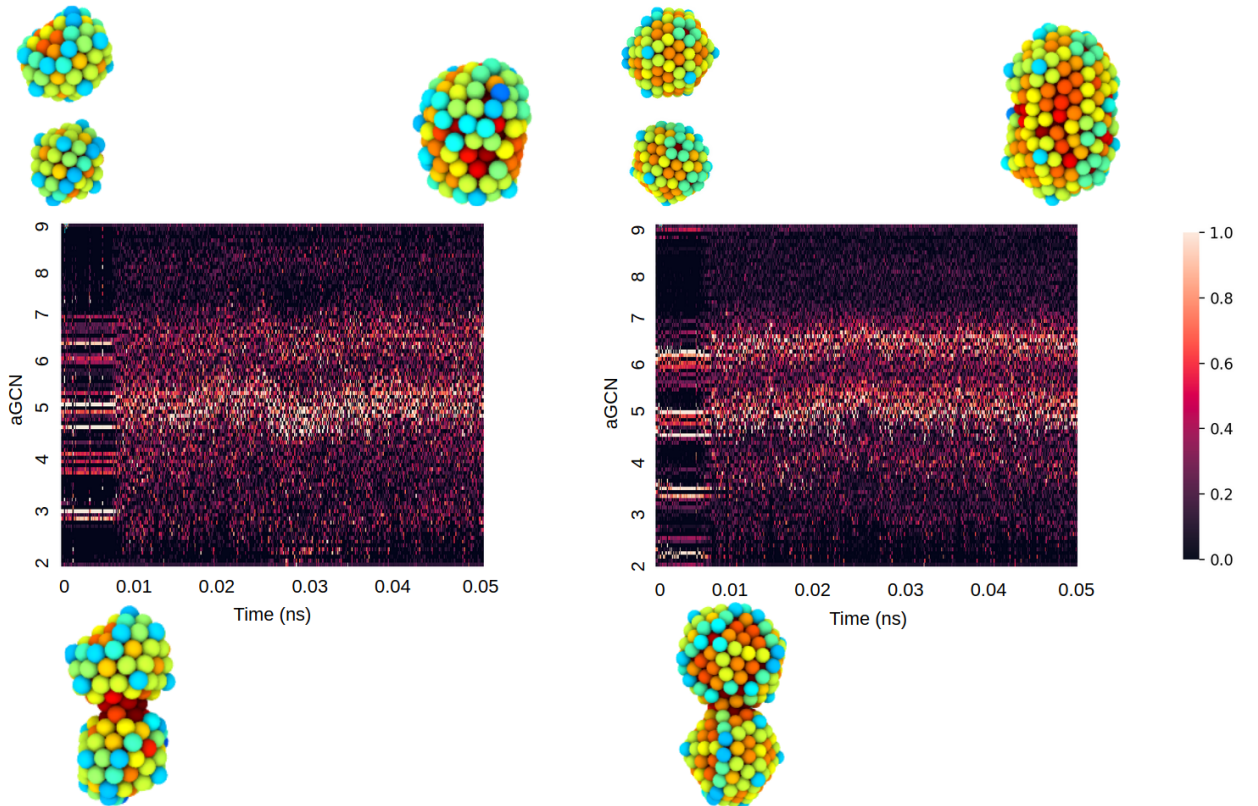


Figure 3.15: aGCN occurrence time evolution in coalescence processes. $\text{Cu}_{110} + \text{Cu}_{130}$ (left) and $\text{Cu}_{270} + \text{Cu}_{250}$ (right). Structures' snapshots are taken at initial, collision and final times.

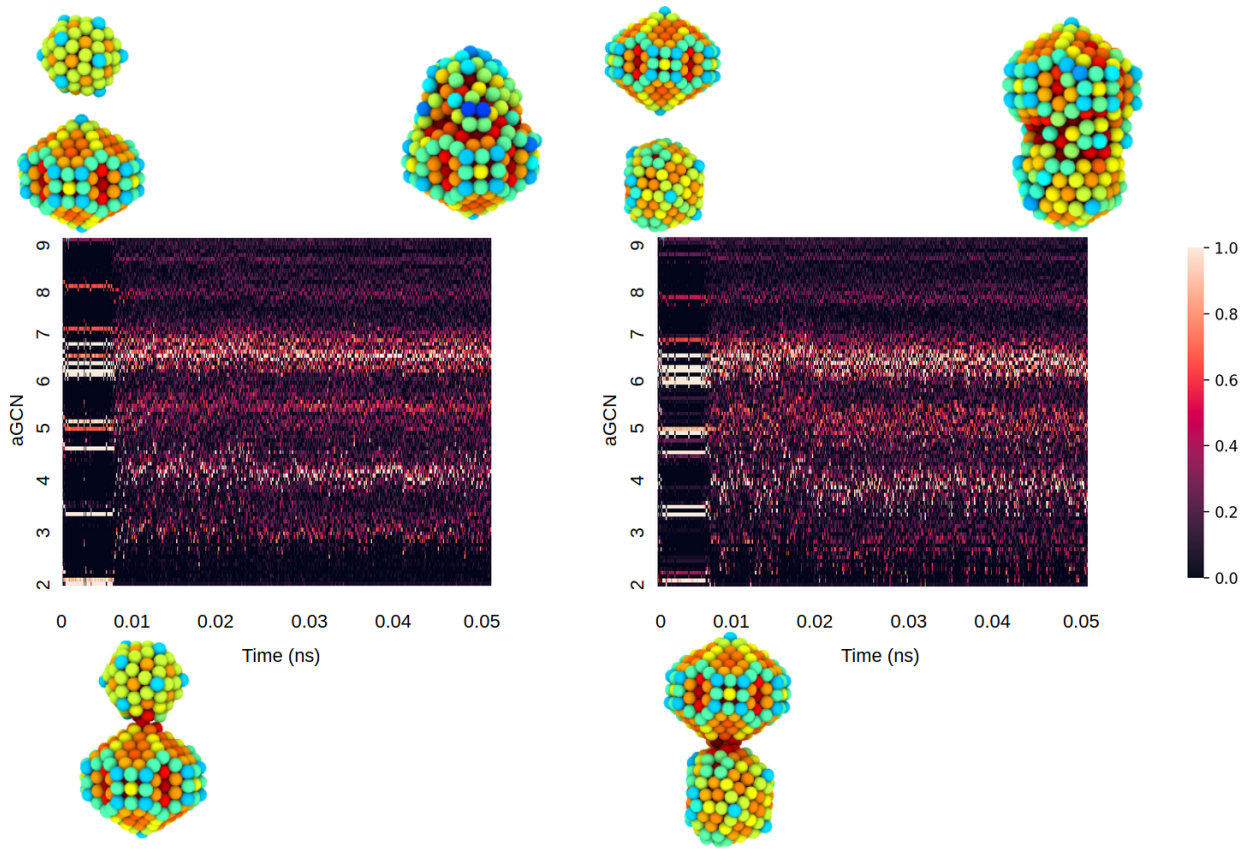


Figure 3.16: aGCN occurrence time evolution in coalescence processes. $\text{Cu}_{147} + \text{Cu}_{434}$ (left) and $\text{Cu}_{285} + \text{Cu}_{434}$ (right). Structures' snapshots are taken at initial, collision and final times.

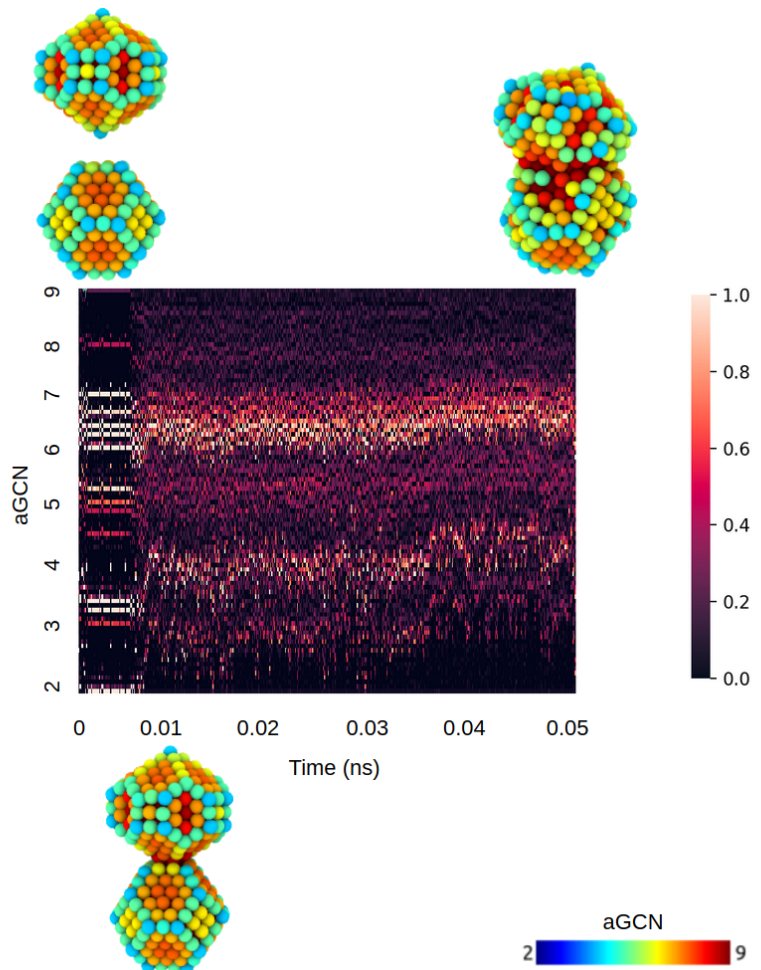


Figure 3.17: aGCN occurrence time evolution in coalescence processes. $\text{Cu}_{405} + \text{Cu}_{434}$. Structure's snapshots are taken at initial, collision and final times.

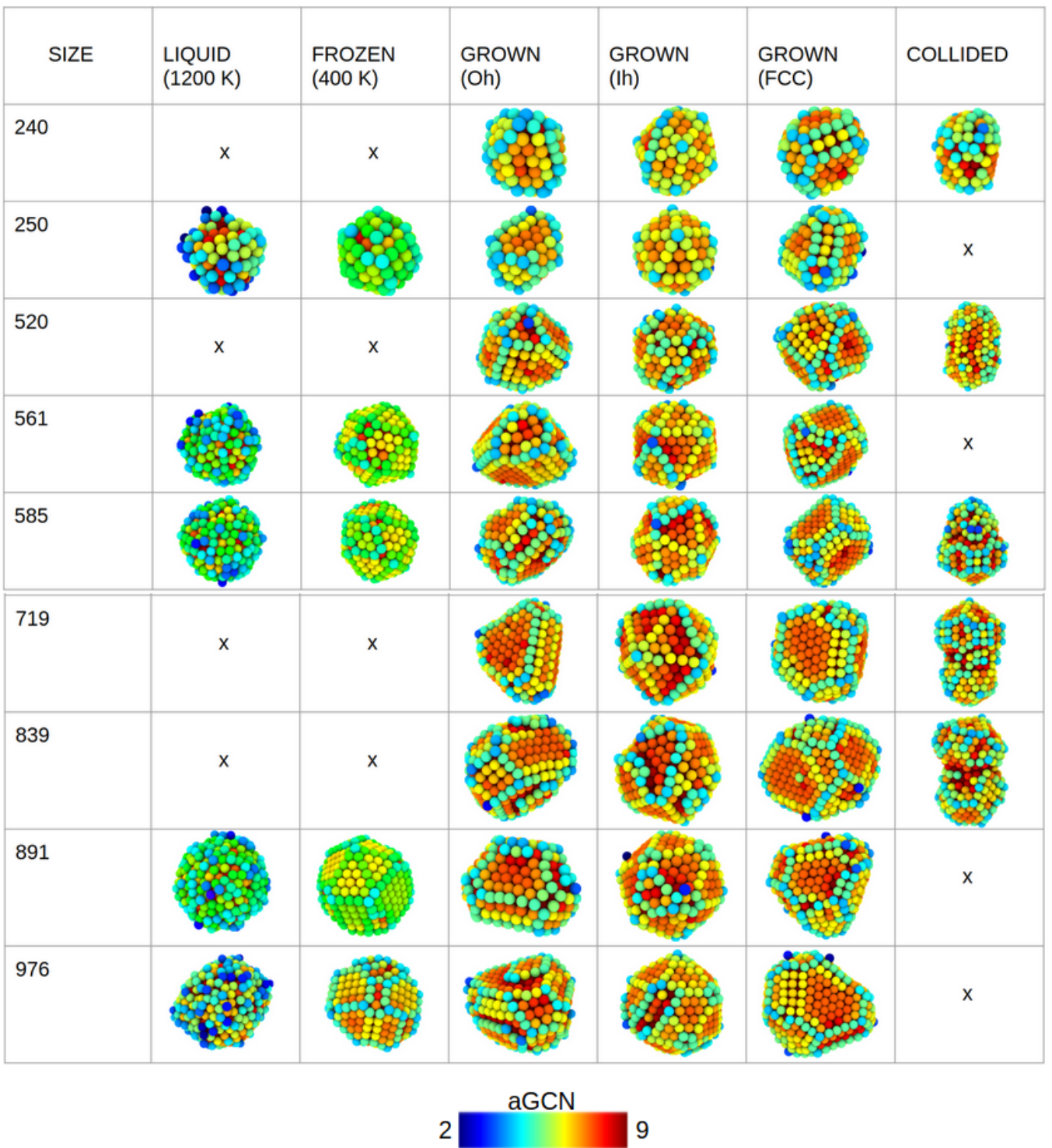


Figure 3.18: Database of resulting structures from different formation processes. The freezing gives spherical shapes, the growth ends up in flatter shapes, and coalescence in elongated structures.

3.3 Catalytic Activity

Once an aGCN distribution is obtained for each structure, the relations by Zhao et al. [32] are employed to determine the most active sites for the CO₂ reduction to CH₄. The current density is calculated by fitting Equation 2.2 to our specific study. The surface area is calculated from Equation 2.9, to then evaluate the mass activity at a specific applied potential is.

3.3.1 Setting the NanoCHE

It is worthy to know that various attempts were made to calculate the constant in Equation 2.2, which is eventually set equal to $-3.01 \cdot 10^{14}$ mA/cm².

The most consistent method which leads to this value makes reference the work by Loiudice et al. [43], where the current density j produced by Cu nanocubes of different sizes is calculated. Since j is normalized in three different ways (geometric, electrochemical and nanocrystal area), the current density used is averaged over all the three normalisations. The 24 nm cube is chose due to its smaller size. It is known from [65] that large-sized cubes present 8 sites with aGCN equivalent to 2 (0.044% of sites in the case of a 24 nm cube) and 24 sites with an aGCN of 5.08 (0.131% of sites for a 24 nm cube). The rest of the composition for a 24 nm cube is; 2.498% of sites with an aGCN equal to 3.67, 4.865% with aGCN 5.83 and the majority of sites, 92.462%, presenting an aGCN signature of 6.67. The percentages corresponding to the aGCN of 3.67 and 5.83 scale linearly with the cube's size, while the higher aGCN composition increases quadratically with the NP's size. The current density - averaged across j_{geom} (-9.1 mA/cm²), j_{ECSA} (-7.2 mA/cm²) and j_{NC} (-5.7 mA/cm²) - produced by such cube at an applied potential of -1.1 V in 0.1 M KHCO₃ and at room temperature is -7.33 mA/cm², where the glassy carbon background signal has already been subtracted [43]. The relation between the aGCN values and ΔG is employed 2.1, and Equation 2.2 is reversed in order to find the constant C , which results in a value of $-3.01 \cdot 10^{14}$ mA/cm².

The procedure which has been just described was adopted after attempting a more cumbersome method: since the value for j in [43] varies considerably depend-

ing on the normalization technique adopted, particular attention was payed to the Cu foil, since it produced a constant current density of -5.56 mA/cm^2 at -1.1 V independently of the normalisation technique.

However, the geometric composition of foil is not specified anywhere in the paper, and there is no common scientific consensus on what it should be. Relations between Miller indexed surfaces - since the foil is supposed to be an infinite crystal - and aGCN on Cu were found in [32]. The relevant ones are reported in Table 3.5.

Miller ind.	aGCN
(111)	7.500
(100)	6.667
(211)	5.500
3AD @ (111)	3.500
2AD @ (111)	2.917

Table 3.5: aGNC related to Cu Miller indices [32]. The last two lines refer to adatoms, namely trimers and dimers.

Sites with low coordination numbers, namely adatoms [69, 70], are found to be the most active, and it is known from previous sections that (100), (111) and (211) surfaces are found to be the reasonably active sites on Cu nanoclusters. By reading [33], it was known that FCC(100) facets produce a current density of -5 mA/cm^2 at an applied potential of -0.99 V at room temperature.

Consequently, a first attempt was made to find a value for C which would reproduce a current density of -5 mA/cm^2 once Equation 2.2 is fitted to a 100% FCC(100) plane. Different compositions for foil, are theorised, as represented in Table 3.6. The values for j and U used to calculate the constant were respectively -5.56 mA/cm^2 and -1.1 V

The resulting current density for FCC(100) facets is reported in Figure 3.19, and compared to the expected one of -5 mA/cm^2 from [33].

The value for the constant seemed to be reasonable in light of these observations, but when inputted in the code to measure the current density produced by the NPs,

	C1	C2	C3
(111)	80%	90%	
(100)	10%	7%	91%
(211)	4%		3.2%
3AD	6%	2%	5.8%
2AD		1%	
value	$-9.878 \cdot 10^{30} \text{ mA/cm}^2$	$-1.007 \cdot 10^{31} \text{ mA/cm}^2$	$-1.016 \cdot 10^{31} \text{ mA/cm}^2$

Table 3.6: Different Cu foil compositions to calculate the constant.

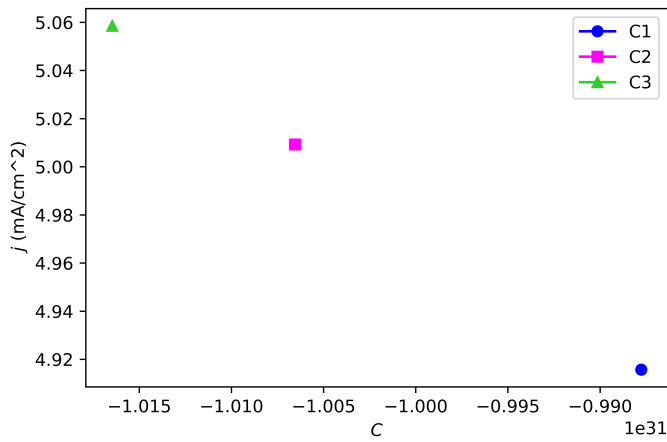


Figure 3.19: First attempts to find the constant.

values of around -10^{20} mA/cm^2 were returned by the algorithm, as Figure 3.20 reports. These values were considered too massive to be produced by a NP with dimensions of 1-2 nm, especially compared to the -5.56 mA/cm^2 produced by the Cu foil.

In addition to leading to extremely high activity values, this latter method used to reproduce the constant was not very accurate, since it combined the data from three different studies, namely [33, 42, 43], where the experimental conditions might have been different or not specified in the papers.

Thus, it was discarded, and another procedure was adopted: considering the cube's composition, as described at the beginning of this chapter.

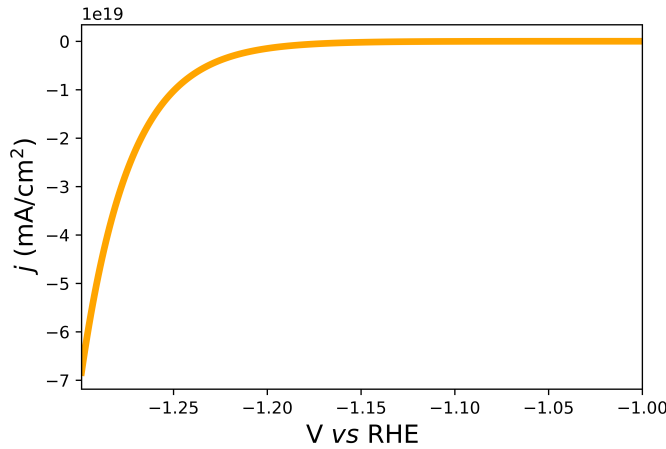


Figure 3.20: Current density produced by frozen Cu₅₆₁ calculated with C2 as a constant.

3.3.2 Current Density

The current density j distribution over an applied potential between 0 V and -1.299 V (with spacing of 1 mV) is calculated with the code described in section 2.3. For the sake of consistency with all the studies taken into account throughout the project, the values for j are plotted against V vs RHE values. The Reversible Hydrogen Electrode scale (RHE) - as opposed to the Standard Hydrogen Electrode (SHE), which only captures the free energy of the electrons - captures the free energy of both electrons and protons in the potential calculations, making them independent of the pH at which the reaction happens. The y values are capped at -15 mA/cm² in order to allow an easier comparison between sizes and processes. The current densities of structures produced with freezing are displayed in Figure 3.21. The current values are all negative, meaning the more negative the value is, the more easily the NP will carry current.

Only the plots corresponding to the initial (liquid) and the final (solid) configurations are reported, since they represent the limiting values. The NPs in the liquid phase always produce more current than the solid ones, even when the comparison is made across all sizes. The only exception is given by Cu₂₅₀, the only one which started with a non-perfectly ordered structure. In fact, if all the other clusters for the freezing processes had undergone a fast melting starting from Oh, To, Ih or

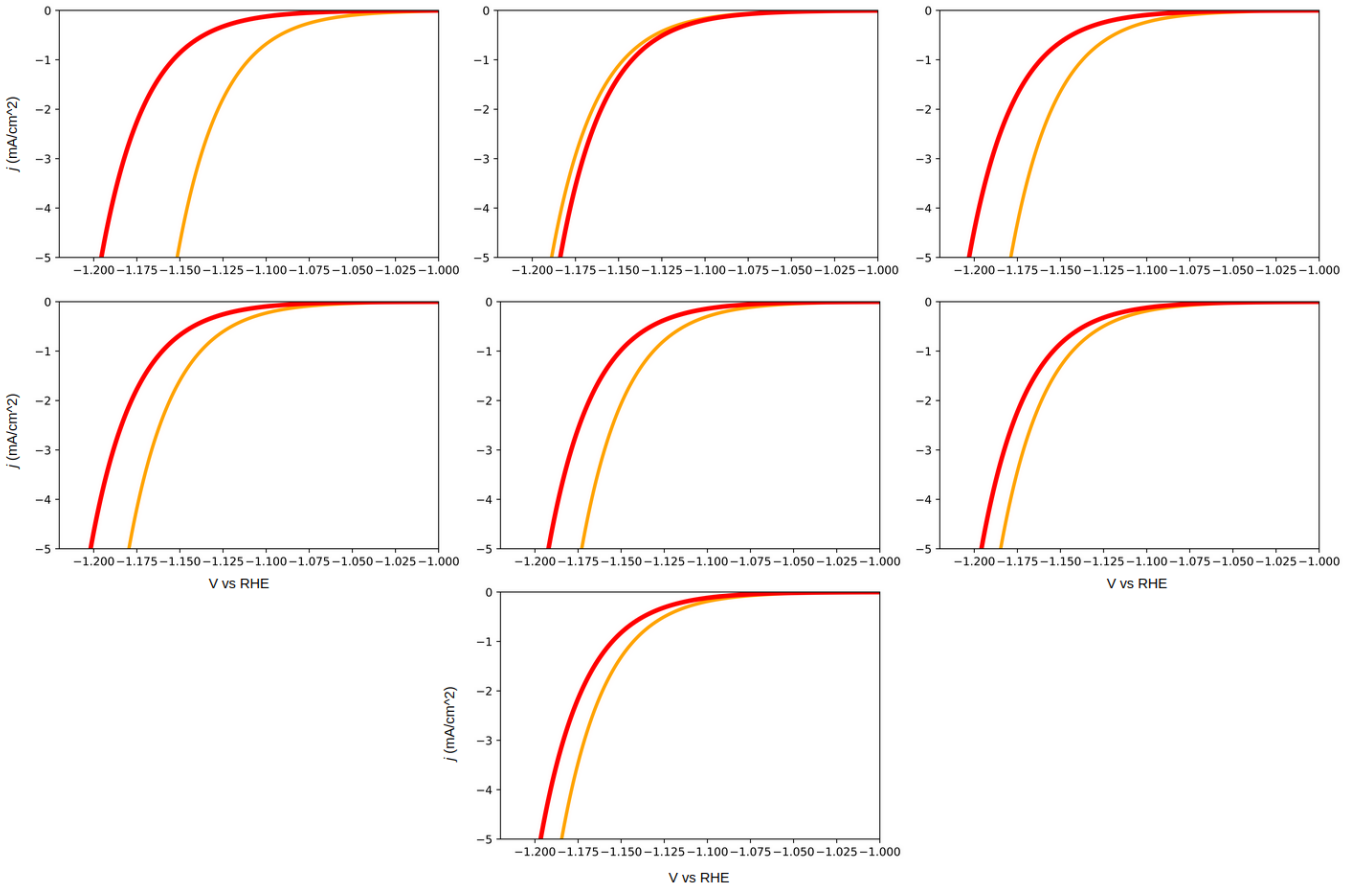


Figure 3.21: Current density for applied potential V in freezing processes. From top left to bottom right: Cu_{147} , Cu_{250} , Cu_{561} , Cu_{585} , Cu_{586} , Cu_{891} and Cu_{976} . The yellow ■ lines represent the current produced by the liquid structures, while the red ■ ones the color produced by the frozen ones.

Dh, Cu_{250} was melted from a structure which had undergone a basin hopping. For this reason, its final solid structure is less ordered than all the other ones, and its liquid structure is the most highly-coordinated one, leading to a lower current density. The shapes of the plots relating j to U are comparable; a higher activity is given by an earlier curvature of the plot towards more negative values at increasing applied potential. Cu_{561} and Cu_{585} carry a lower j , since their final shapes are more highly-coordinated. The liquid phase of Cu_{147} , being a very small structure with a high number of low-coordinated sites - as had already been noticed from the aGCN analysis - carries an extremely high current density, far off from all the other values. The structure being so small, some quantum effects are not to be excluded in this

case, such as atom excitations opening up a band gap and conducting more current. With the increase in size, the liquid structures carry less current density, especially Cu₈₉₁ and Cu₉₇₆, which present more highly-coordinated sites on their surfaces, and do not have time to reach a completely disordered state during the fast melting.

The activity of frozen clusters is compared to the one of grown ones, shown in Figure 3.22.

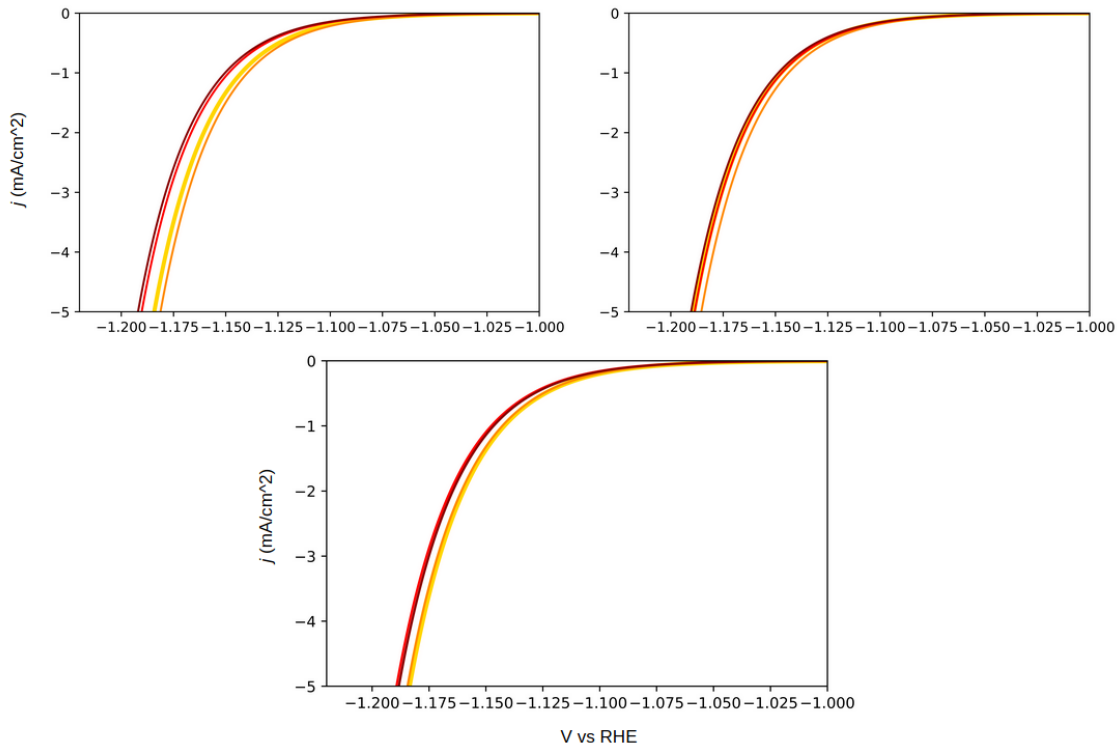


Figure 3.22: Current density for applied potential V in growth processes. From top left to bottom right: growth of an Oh, Ih and FCC geometry. The different colors represent the number of atoms making up the NP: ■ for 250, ■ for 561, ■ for 719, ■ for 976.

The smaller structures are less coordinated, and carry therefore a higher current density. The small Oh and To seem to be the most promising structures at the beginning. The Oh evolution produces a high current density at sizes equivalent to 561 atoms, to then lose its property to carry a higher current density for larger structures with 976 atoms. The Ih follows the same initial behaviour, but then at bigger sizes seems to be more active than the Oh. The To loses current density

along with its size evolution, starting with values similar to the Oh and ending up with the most negative current density value.

In coalescence processes, the current density does not depend on the NP's size like in the other two processes, as can be seen by the colors in Figure 3.23.

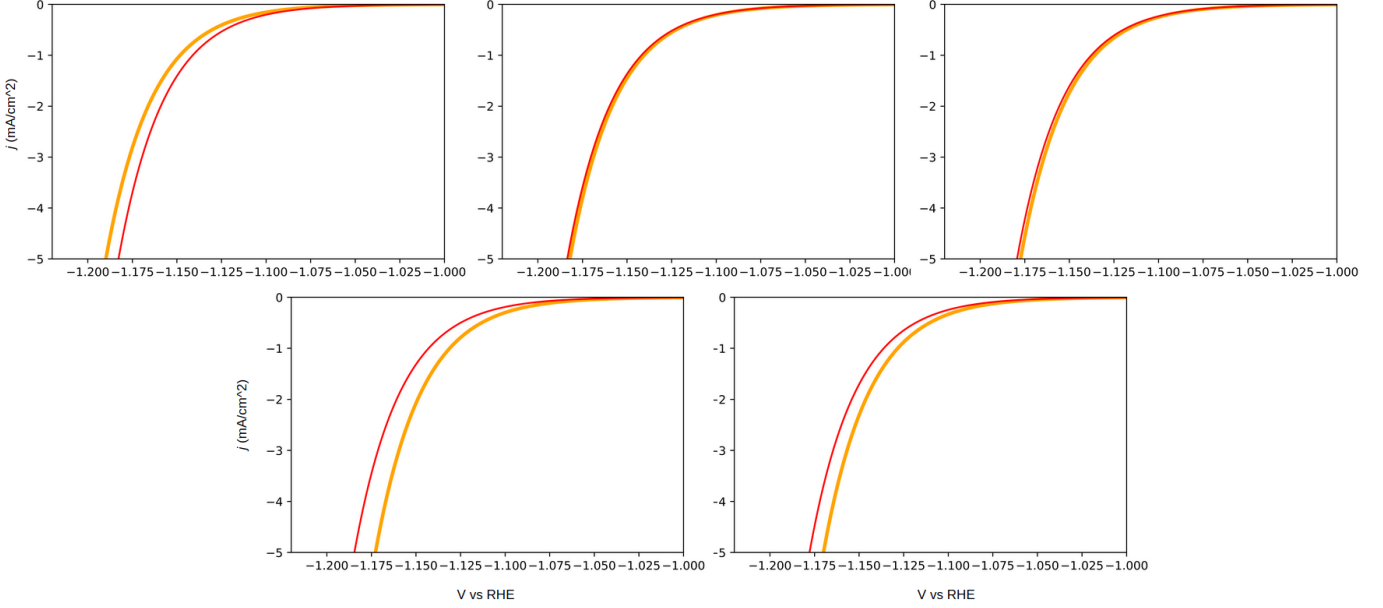


Figure 3.23: Current density for applied potential V . From top left to bottom right: $\text{Cu}_{110} + \text{Cu}_{130}$, $\text{Cu}_{270} + \text{Cu}_{250}$, $\text{Cu}_{147} + \text{Cu}_{434}$, $\text{Cu}_{285} + \text{Cu}_{434}$ and $\text{Cu}_{405} + \text{Cu}_{434}$. The yellow ■ lines represent the initial system, while the red ■ ones the final elongated structure.

The system seem to produce a higher current density at its final stage (when the two clusters are merging together) only at very small sizes ($\text{Cu}_{110} + \text{Cu}_{130}$), probably because it does not experience the formation of highly-coordinated sites after the collision. The latter is likely to happen in all the other cases, where the two separated clusters produce more current density when separated than when combined together. This behaviour makes sense, in light of the fact that a bigger structure, formed after the collision, would be composed of a higher percentage of high-coordinated sites, as can be seen from the atoms colored in red on the neck in the representations of the aGCN analysis.

The last three plots in Figure 3.23 represent a collision between Cu_{434} (a mDh) and Cu_{147} (an Ih), Cu_{285} (a dIh resulting from a basin hopping) or Cu_{405} (a To).

As the size of the whole system grows, the initial current density produced when the clusters are separated increases as well. When, instead, the focus is on the final structures, it can be noticed how the current density produced by the collision with Ih is more promising than the collision with a To. This factor will affect the mass activity of the cluster and is analyzed in the next section.

The current density results for each process are displayed all together in Figure 3.24. The x and y axes are enlarged in order to analyse the behaviour around an applied potential of -1.1 V. The specific activity at -1.1 V will be employed to measure the NPs' mass activity. This decision is made in light of previous studies taken into account [31,33,43], which measure the Cu CO₂RR activity at -1.1 V. The current density results range from -0.12 mA/cm² (frozen Cu₅₆₁) to -0.69 mA/cm² (liquid Cu₁₄₇) for an applied potential of -1.11 V, and they are displayed all together in Figure 3.24.

It can be seen how in the coalescence process the size does not influence the current density evolution. The collision of a mDh with Ih and dIh (sizes of 581 and 719 atoms) lead to NPs carrying more current density than other collided structures. Such high j_s are only achieved at liquid small NPs. The only frozen NPs that can be compared to other results are Cu₂₅₀ and Cu₅₈₆, which are disordered enough to exhibit low-coordinated sites: the first produces a current density equivalent an FCC grown to 250 atoms, while the latter to an Oh grown to 976 atoms. All the other frozen sizes produce less current than any other process. Liquid structures are better than grown ones at equivalent sizes (apart from Cu₂₅₀). Within the grown structures, the Ih evolution leads to less current density at every size considered. At very small (250 atoms) and very big (976 atoms) sizes the FCC evolution produces more current density, while at intermediate sizes the Oh seems to be more favourable for the CO₂ activity.

A first hint of which NPs are going to be more active for the CO₂RR was given in this section. However, to calculate the absolute activity of a NP, the mass activity needs to be considered; for its calculation, information on the surface area of each cluster (and its evolution) is required.

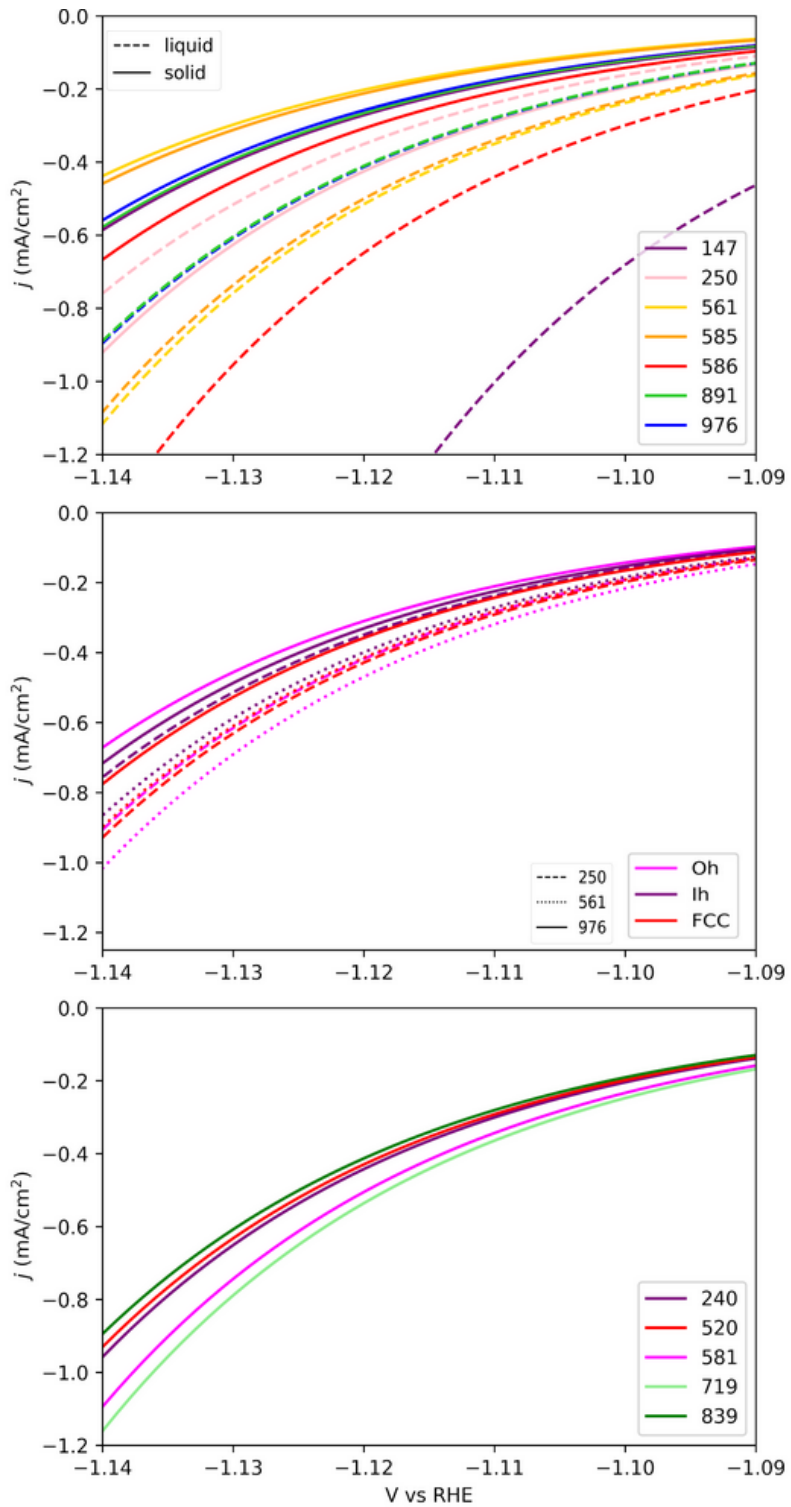


Figure 3.24: IV curves for $\text{CO} \rightarrow \text{CH}$. (top) freezing process, dashed line refers to the melted phase and solid-line for the frozen object; (middle) growth one-by-one, different colours refers to different initial seeds; (bottom) coalescence after 0.05 ns.

3.3.3 Surface Area

This section briefly reports the results of the surface area calculations from the aGCN through equation 2.9, where the less a site is coordinated, the more it contributes to the surface area. The surface area is comparable across the processes, with

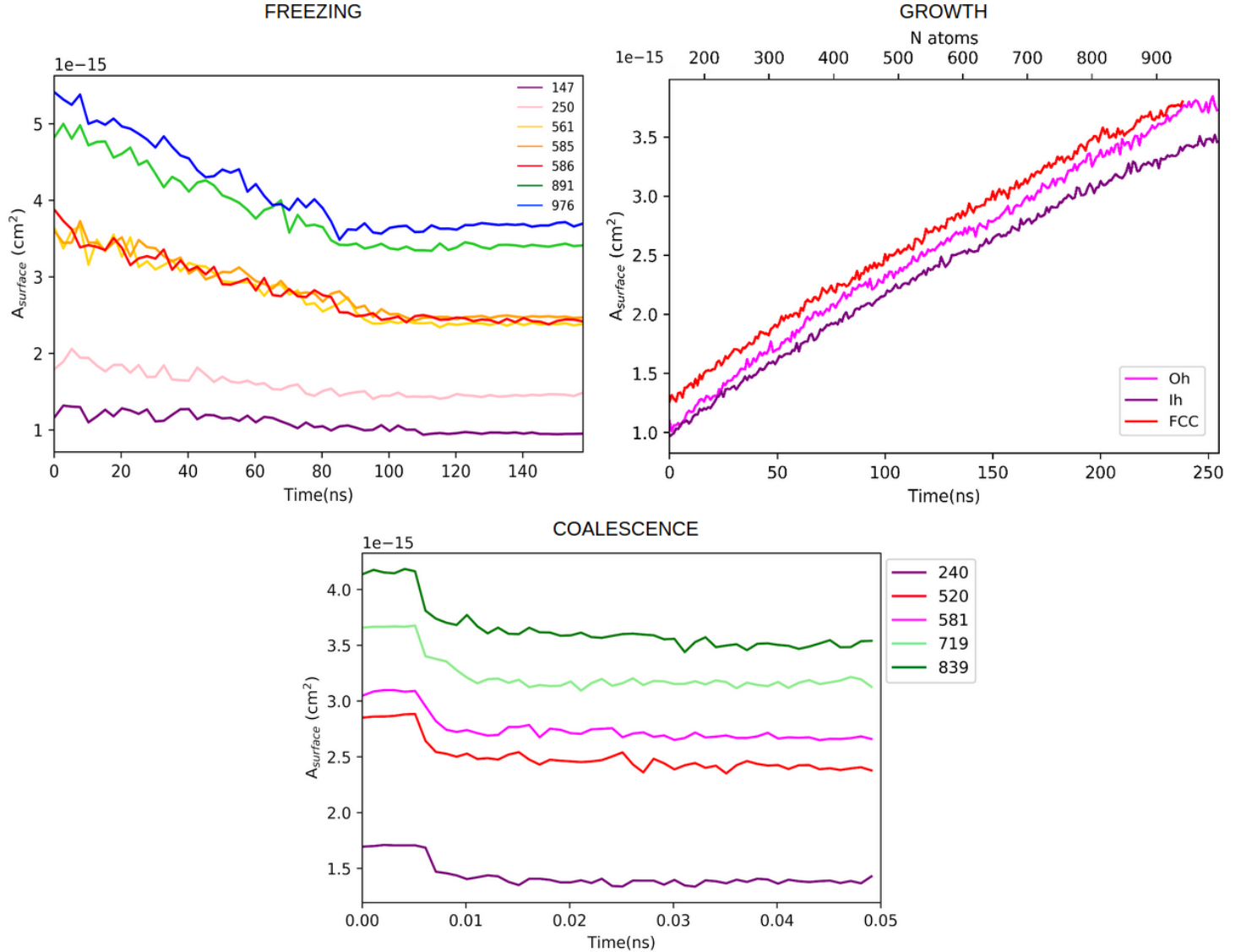


Figure 3.25: Surface area time evolution for the various processes.

values ranging from $1 \cdot 10^{-15}$ to $5.2 \cdot 10^{-15} \text{ cm}^2$. The liquid phase has the most extended surface area, as expected, considering all its low-coordinated surface sites. The surface area of the grown Ih is always lower, followed by the grown Oh and, ultimately, by the FCC. As concerns the coalescence, it is obvious that the surface

area is more spread when the structures are separated, to then decrease once the clusters collide. Once the structures are frozen or collided, their surface area's extension is equivalent to the grown structures at similar sizes.

Once the surface area is obtained, the last step of the analysis can be performed: the mass activity calculation.

3.3.4 Mass Activity

The mass activity of each nanocluster is calculated within the ‘catalyticanalysis’ part of the code. The surface area and the number of atoms (in the case of the growth processes) is updated at each time step, the specific activity SA at -1.1 V is collected for each time step, and the mass of the nanoparticle is obtained by multiplying the mass of Cu by the number of atoms. By applying equation 2.8 to each time step, plots of the mass activity evolution are produced as in Figure 3.26. The mass activity range resulting from the freezing formation processes is the widest, i.e. 6.7-29.4 mA/mg in the liquid phase, and 5.2-9.6 mA/mg in the solid one. Grown NPs’ MA span from 5.7 mA/mg to 11.2 mA/mg. Collided structures’ MA spans a narrower range of values, i.e. 8.1-10.3 mA/mg.

The liquid droplet of Cu₁₄₇ is extremely active compared to all the other NPs, as expected from its surprisingly high current density (with respect to all the other results). In general, liquid NPs are more active than solid ones due their lower-coordination: the only exception is, again, given by the freezing of a non-magical size obtained by a basin hopping, Cu₂₅₀. The low current density produced by large NPs and their larger mass result in a restricted mass activity of large structures produced by freezing, compared to smaller ones resulting from the same formation process. The MAs of Cu₁₄₇, Cu₂₅₀ and Cu₅₈₆ reach values of 7.5-9.6 mA/mg, higher than the 6 mA/mg produced by Cu₉₇₆. There are, however, a few exceptions to the monotonically increasing mass activity with the decrease of NP’s size in freezing processes: frozen Cu₅₆₁ exhibits a mass activity lower than Cu₅₈₆, for instance, or Cu₈₉₁ seems less active than Cu₉₇₆. These anomalies from the general trend originate from differently-coordinated structures. It is known how Cu₅₆₁ and Cu₅₈₅ especially, give rise to highly-coordinated structures, while Cu₅₈₆ is more highly

defected at the end of the simulation.

Quite surprisingly, the activity has a different size-trend depending on the formation process. While the freezing has a monotonic decrease with the nanoparticle size, the larger and more defected nanoparticles obtained via the one-by-one growth, although depending on the shape of the initial seed, are the most active.

This behaviour can be explained by the fact that the growth process disorders the structures, and the current density for growth formation did not particularly depend on the NPs' sizes, so the increase in surface area is not balanced by any other factor, leading to higher mass activities at bigger sizes. The Ih structures are more active than Oh, which are more active than FCC in the very first moments of the growth process. Small grown NPs made of around 250 atoms report a MA between 6.5 mA/mg and 7.5 mA/mg, noticeably lower than the activity of a frozen NP at the same size, which is about 9.6 mA/mg.

From sizes of 550 to 650 atoms the Oh evolution seems the most promising one, with a MA of around 8.5 mA/mg, high compared to the value of 7.5 mA/mg produced by frozen Cu₅₆₁. At this stage already, grown NPs appear to be more active than frozen ones. The FCC evolution leads to reasonably active structures for sizes of 300 and 400, and for structures between 700 and 800, but it then drops considerably to values of around 7 mA/mg for sizes of 900 atoms, which is still a greater activity than 6 mA/mg of frozen Cu₉₇₆. The same oscillatory behaviour is followed by the Oh evolution, which presents a peak in activity at 850 atoms sizes, to then suddenly increase to 11.2 mA/mg. The Ih growth produces structures which are active at large sizes: for instance, when they are composed of 891 atoms, their MA is 10 mA/mg, higher than the frozen Cu₈₉₁, which has a final MA of only 5.2 mA/mg. Growth process are deemed to be better formation processes than freezing ones for the larger catalysts, since their final shapes are more highly defected than the ordered geometries deriving from the liquid-solid phase transition in freezing processes. However, if the focus is on obtaining an extremely small catalyst, of around 1.5 nm, freezing a liquid droplet of Cu might be a better procedure to be adopted, due to the high abundance of low-coordinated sites deriving from the liquid phase.

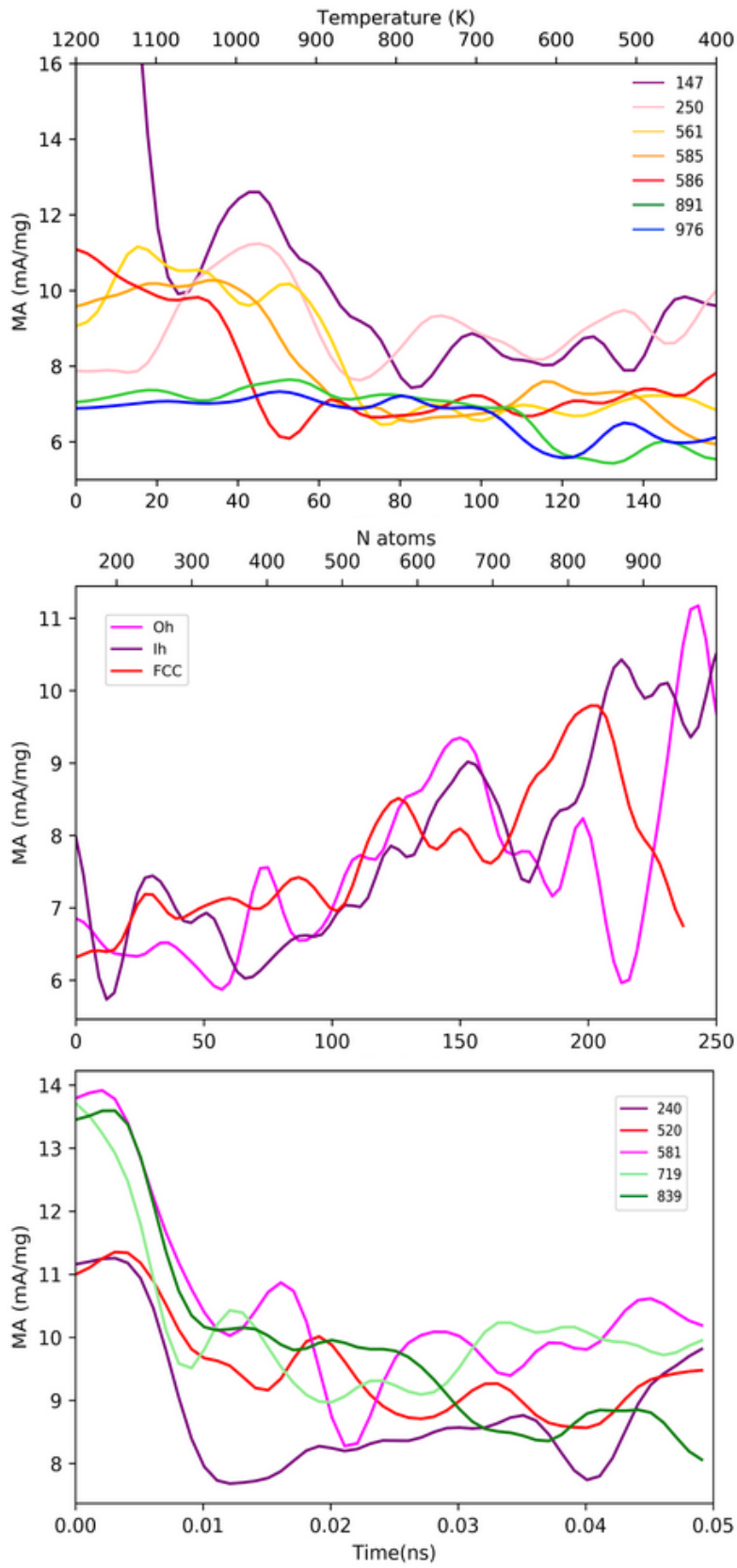


Figure 3.26: Mass activity evolution in mA/mg. The lines have been smoothed using a Gaussian fit to make them more readable. The plots refer to (top) freezing process, (middle) growth one-by-one and (bottom) coalescence. The legends for freezing and coalescence represent the number of Cu atoms.

In the case of coalescence formation processes, it is more challenging to find a relationship between mass activity and system's size. The activity is noticeably decreasing (from values of 14 mA/mg to 10.3 mA/mg for the case of Cu₅₈₁, for instance) as the two clusters collide, mainly because the surface area is as well. The smaller system, made of two dIh generated with a basin hopping presents the lowest mass activity for the whole simulation, becoming more active than the merged cluster of 839 atoms only on the last picoseconds of the process. Another example is given by the structure made up of a mDh and a perfect Ih, for a total of 581 atoms: its mass activity is initially very high, then it drops lower than many other structures, and eventually it rises up above all the other simulations, reaching a mass activity of around 10.3 mA/mg. The pink, light green and dark green lines in the bottom plot of Figure 3.26 require a few more comments. They represent a collision between a mDh (Cu₄₃₄) and 1) a perfectly ordered Ih (pink line), 2) a dIh coming from a basin hopping (light green line), 3) and a perfectly ordered To (dark green line). From the mass activity plots, it can be seen how an Ih collision is more favourable than a dIh collision, which again leads to a higher mass activity than a To. These observations lead us into thinking that the activity of NPs resulting from coalescence processes depends on the clusters' structural geometry more than on their sizes.

Conclusions

Three NPs formation processes - freezing, growth, coalescence - are investigated by means of CMD to individualise which are the ideal Cu sizes and shapes for CO₂ electrochemical catalysis to CH₄. An analysis on the final excess energies is performed, to conclude that frozen structures are more energetically favourable than grown or collided ones, under the same sizes. A CNA analysis shows how the frozen NPs preserve their spherical shape, and how after the liquid-solid phase transition they become more ordered. Ih growth progresses by adding one layer after the other, leading to large dIh structures, while the Oh and To evolution lead to more disordered structures composed by an abundance of (111) and (100) facets. Coalescence formation processes produce elongated NPs. The NanoCHE model is proven effective to calculate the current density produced by the clusters at -1.1 V; the results range from -0.12 mA/cm² (frozen Cu₅₆₁) to -0.69 mA/cm² (liquid Cu₁₄₇) for an applied potential of -1.11 V. Smaller clusters and low-coordinated clusters carry a higher current density, confirming the fact that surface roughness and defects improve catalytic performance of Cu nanoparticles for the CO protonation. Quite surprisingly, the mass activity has a different size-trend depending on the NP formation process. Freezing processes are characterised by a monotonically increase in mass activity with the decrease of NP's size. Small frozen droplets (1.6 nm) generate 9.6 mA/mg, while solid structures resulting from freezing present a mass activity between 6.5 mA/mg and 7.5 mA/mg at the same size. The opposite behaviour is observed in one-by-one growth processes, where larger and more defected NPs are the most active. At sizes of around 2.5 nm, Cu clusters grown from an Oh geometry produce 11.2 mA/mg, a high activity if compared to 5.2 mA/mg, the mass activity generated by the same-sized frozen Cu droplets. Growth process are deemed to be

better formation processes than freezing ones for larger catalysts. However, if a 1.5 nm catalyst needs to be built for CO₂RR, freezing a liquid droplet of Cu might be a better procedure to be adopted. Coalescence has a non-monotonic behaviour with size strongly depending on how fast necks and interfaces of the individual nanoparticles rearrange. Collision between a perfect Ih and a mDh produces 10.3 mA/mg, suggesting the fact that collided Ih would be better catalysts than other collided shapes.

Further Extensions

There is the potential for the generalised coordination number to be calculated for bridge and hollow sites as well, namely for adsorption sites composed of a couple or a triplet of atoms. Attempts to write a code to calculate the bridge GCN were made, but not accomplished due to time issues. The calculation of hollow GCN was also taken into account, by employing the MFF Python package [83], a machine learning tool to generate force fields. Also this idea should be expanded in further explorations. Only three of the formation processes available in LoDiS were investigated, but the attention could be focused on NVT and quenching as well. To get more accurate results, more than four simulations for each case should be taken into account; moreover, a wider range of sizes could be explored, especially for freezing processes with 250-561 atoms, and the simulations should be run for the same amount of time for sake of consistency, especially coalescence processes. More strategies could also be considered to find an accurate value for the constant in the current density equation (Equation 2.2). An even more accurate procedure, taking into account a wider range of current literature results and data, could potentially lead to a higher NP activity. Last but not least, the Cu NPs should be investigated not only in vacuum, but in a solution, or on top of a substrate. This factor is expected to improve their catalytic activity, and results could be compared to the to be compared, for instance, to the mass activity of 1.45 A/mg at an applied potential of -0.65 V vs RHE of Cu octahedra in 1M KOH [84].

Bibliography

- [1] J. Sawyer et al. *Carbon Dioxide and the “Greenhouse” Effect.* Nature, 1972, 239, 2.83.
- [2] T. Volk. *CO₂ rising: the world’s greatest environmental challenge.* MIT Press, 2008.
- [3] G. A. Olah et al. *Chemical Recycling of Carbon Dioxide to Methanol and Dimethyl Ether: From Greenhouse Gas to Renew-able, Environmentally Carbon Neutral Fuels and Synthetic Hydrocarbons.* J. Org.Chem., 2009, 74, 487-498.
- [4] D. Y. C.Leung et al. *An overview of current status of carbon dioxide capture and storage technologies* Renew. Sust. Energ. Rev., Vol. 39, 2014, 11, 426-443.
- [5] C. Hahn et al. *Engineering Cu surfaces for the electrocatalytic conversionof CO₂: Controlling selectivity toward oxygenates and hydrocarbons.* PNAS, 2017, 6, 114 (23) 5918-5923.
- [6] X. Kang et al. *Highly efficient electrochemical reduction of CO₂ to CH₄ in an ionic liquid using a metal–organic framework cathode.* Chem. Sci.,2016, 7, 266.
- [7] A. S. Agarwal et al. *The electrochemical reduction of carbon dioxide to formate/-formic acid: engineering and economic feasibility.* ChemSusChem, 2011, 4 , 1301-1310.
- [8] Y. Hori et al. *Electrocatalytic Process of CO Selectivity in Electrochemical Reduction of CO₂ at Metal Electrodes in Aqueous Media.* Electrochim. Acta 1994, 39, 1833-1839.

- [9] S. Min et al. *Low Overpotential and High Current CO₂ Reduction with Surface Reconstructed Cu Foam Electrodes.* Nano Energy 2016, 27, 121–129.
- [10] D. Raciti et al. *Highly Dense Cu Nanowires for Low-Overpotential CO₂ Reduction.* Nano Lett. 2015, 15, 10, 6829-6835.
- [11] S. Chubbock et al. *Comparative Analysis of Internal Combustion Engine and Fuel Cell Range Extender.* SAE Int.J.Alt. Power. 5(1) 2016.
- [12] S. Nitopi et al. *Progress and Perspectives of Electrochemical CO₂ Reduction on Copper in Aqueous Electrolyte.* Chem. Rev. 2019, 119, 7610-7672.
- [13] R. Kortlever et al. *Catalysts and reaction pathways for the electrochemical reduction of carbon dioxide.* J. Phys. Chem. Lett. 6:4073-4082.
- [14] Y. Hori. *CO₂ reduction using electrochemical approach. Solar to Chemical Energy Conversion: Theory and Application.* Springer Int., Cham, Switzerland, 191-211.
- [15] A. Alshammari et al. *Metal Nanoparticles as Emerging Green Catalysts.* <http://dx.doi.org/10.5772/63314>.
- [16] C. Anmin et al. *Stabilizing metal nanoparticles for heterogeneous catalysis.* Phys.Chem.Chem.Phys., 2010, 11, 12(41):13499-510.
- [17] R. Schlögl. *Heterogeneous Catalysis* Angew. Chem., Int. Ed., 2015, 54,3465-3520.
- [18] I. Lee et al. *Tuning selectivity in catalysis by controlling particle shape.* Nat. Mater., 2009, 8, 132-138.
- [19] J. B. A. Davis et al. *The Effect of Dispersion Correction on the Adsorption of CO on Metallic Nanoparticles.* J. Phys. Chem. A, 2015, 119, 9703–9709.84.
- [20] M. Foster et al. *Experimental determination of the energy difference between competing isomers of deposited, size-selected goldnanoclusters.* Nat. Commun., 2018, 9, 1323.

- [21] KP Kuhl et al. *Electrocatalytic conversion of carbon dioxide to methane and methanol on transition metal surfaces.* J Am Chem Soc 136:14107-14113.
- [22] K. Manthiram et al. *Enhanced electrochemical methanation of carbon dioxide with a dispersible nanoscale copper catalyst.* J.Am. Chem. Soc. 136:13319-13325.
- [23] FS Roberts et al. *High selectivity for ethylene from carbon dioxide reduction over copper nanocube electrocatalysts.* Angew Chem Int Ed Engl 54: 5179-5182.
- [24] D. Ren et al. *Selective electrochemical reduction of carbon dioxide to ethylene and ethanol on copper oxide catalysts.* ACS Catal., 5:2814-2821.
- [25] KP Kuhlet al. *New insights into the electro- chemical reduction of carbon dioxide on metallic copper surfaces.* Energy Environ. Sci. 5:7050–7059.82.
- [26] H. Mistry et al. *Highly Selective Plasma-Activated Copper Catalysts for Carbon Dioxide Reduction to Ethylene.* Nat. Commun.2016, 7, 1-9.
- [27] C. Liet al *CO₂ Reduction at Low Overpotential on Cu Electrodes Resulting from the Reduction of Thick Cu₂O Films.* J. Am. Chem. Soc. 2012, 134,7231-7234.
- [28] J. Qiao et al. *A Review of Catalysts for the Electroreduction of Carbon Dioxide to Produce Low-Carbon Fuels.* Chem. Soc. Rev. 2014,43, 631-675.
- [29] J. W. Vickers et al. *Electrochemical Carbon Dioxide Reduction at Nanostructured Gold, Copper, and Alloy Materials.* Energy Technol. 2017, 5, 775-795.
- [30] A. A. Peterson et al. *How copper catalyzes the electroreduction of carbon dioxide into hydrocarbon fuels.* Energy Environ. Sci. 2010, 3, 13111315.
- [31] A. A. Peterson et al. *Activity descriptors for CO₂ electroreduction to methane on transition-metal catalysts.* J. Phys.Chem. Lett. 2012, 3, 251258.
- [32] Z. Zhao et al. *Generalized Surface Coordination Number as an Activity Descriptor for CO₂ Reduction on Cu Surfaces.* J. Phys. Chem. C 2016, 120, 28125-28130.
- [33] W. J. Durand et a. *Structure effects on the energetics of the electrochemical reduction of CO₂ by copper surfaces.* Surf. Sci. 605 (2011) 1354-1359.

- [34] T. Bligaard et al. *Ligand effects in heterogeneous catalysis and electrochemistry*. *Electrochim. Acta* 52 (2007) 5512-5516.79.
- [35] J.K. Norskov et al. *Towards the computational design of solid catalysts*. *Nat. Chem.* 1 (2009) 37-46.
- [36] J. Kleis et al. *Finite Size Effects in Chemical Bonding: From Small Clusters to Solids*. *Catal.Lett.* 141 (2011) 1067-1071.
- [37] K. Rossi et al. *A genomic characterization of monometallic nanoparticles*. RSC, Issue 9, 2019.
- [38] X. Zhang et al. *Optimum Cu nanoparticle catalysts for CO₂ hydrogenation towards methanol*. *Nano Energy* 43 (2018) 200-209.
- [39] Y. Hori. *Electrochemical CO₂ reduction on metal electrodes*. Modern Aspects of Electrochemistry, Springer, New York, 2008, 89–189.
- [40] W. Tang et al. *The importance of surface morphology in controlling the selectivity of polycrystalline copper for CO₂ electroreduction*. *Phys. Chem. Chem. Phys.* 14 (2012) 76-81.
- [41] I. E. L. Stephens et al. *Understanding the electrocatalysis of oxygen reduction on platinum and its alloys*. *Energy Environ. Sci.*, 2012, 5, 6744.
- [42] K. Rossi et al. *Correlating Oxygen Reduction Reaction Activity and Structural Rearrangements in MgO-Supported Platinum Nanoparticles*. *Chem. Phys. Chem.* 2019, 20, 1 – 9.
- [43] A. Loiudice et al. *Tailoring Copper Nanocrystals towards C₂ Products in Electrochemical CO₂ Reduction*. *Angew. Chem. Int. Ed.* 2016, 55, 5789-5792.
- [44] M. Rück et al. *Oxygen Reduction Reaction: Rapid Prediction of Mass Activity of Un-strained Nanostructured Platinum Electrocatalysts*. *J. Phys. Chem. Lett.* 2018, 9, 15, 4463-4468.
- [45] Armand Auquier's MSci Thesis KCL, 2020, 4.

- [46] J.D. Honeycutt et al. *Molecular dynamics study of melting and freezing of small Lennard-Jones clusters.* J. Phys. Chem. 1987, 91, 4950-4963.
- [47] F. Baletto et al. *Structural properties of sub-nanometer metallic clusters.* J. Phys. Condens. Matter 2019, 31, 113001.
- [48] D. Alfonso et al. *First-Principles Modeling in Heterogeneous Electrocatalysis.* Catalysts, 2018, 8, 424.
- [49] F. Calle-Vallejo et al. *Fast Prediction of Adsorption Properties for Platinum Nanocatalysts with Generalized Coordination Numbers.* Angew. Chem. Int. Ed. 2014, 53, 8316–8319.
- [50] F. Calle-Vallejo et al. *Finding optimal surface sites on heterogeneous catalysts by counting nearest neighbors.* A. S. Science, 2015, 350, 185-189.
- [51] F. Calle-Vallejo et al. *Why conclusions from platinum model surfaces do not necessarily lead to enhanced nanoparticle catalysts for the oxygen reduction reaction.* Chem. Sci. 2017, 8, 2283–2289.
- [52] P. Strasser et al. *Electrochemical processes on solid shaped nanoparticles with defined facets.* Chem. Soc. Rev. 2018, 47, 715–735.81.
- [53] D. Frenkel et al. *Understanding Molecular Simulation* Academic Press, Inc. 6277, Sea Harbor Drive Orlando, FL, United States.
- [54] F. Baletto. *LoW-Dimensional Systems Molecular Dynamics.* 2019; <https://github.com/orgs/kcl-tscm/teams/lodis>.
- [55] K. Rossi et al. *Thermodynamics of Cu Pt nanoalloys.* Sci. Rep. 2018, 8, 9150.
- [56] H. Zhai et al. *Fluxionality of Catalytic Clusters: When It Matters and How to Address It.* ACS Catal. 2017, 7, 19051911.
- [57] X. Xing et al. *Dynamicfluxionality and enhanced CO adsorption in the presence of coadsorbed H₂O on free gold cluster cations.* IJMS 377 (2015)393–402.

- [58] A. Vargas et al. *Fluxionality of gold nanoparticles investigated by Born-Oppenheimer molecular dynamics*. Phys.Rev. B, 2009, 07, 80(19), 195421.
- [59] F. Baletto et al. *Structural properties of nanoclusters: Energetic, thermodynamic, and kinetic effects*. Review. Mod. Phys., Vol.77, 2005, 1.
- [60] A. Larsen et al. *The atomic simulation environment - a Python library for working with atoms*. J. Phys. Condens.Matter 2017, 29, 273002.
- [61] A. Stukowski. *Visualization and analysis of atomistic simulation data with OVITO – the Open Visualization Tool*. Modelling Simul. Mater. Sci. Eng. 18(2010), 015012.
- [62] S. Trasatti et al. J. Electroanal. Chem., 1992, 327, 353–376.
- [63] C. W. Li et al. *Electroreduction of carbon monoxide to liquid fuel on oxide-derived nanocrystalline copper*. Nature, 2014, 508 , 504—507.
- [64] X. Feng et al. *Grain-Boundary-Dependent CO₂ Electroreduction Activity*. J. Am. Chem. Soc., 2015, 137 , 4606 —460.
- [65] K. Rossi. *Multiscale modelling of metallic nanoparticles structural and catalytic properties*. PhD Thesis, KCL (2018).
- [66] H. Moerkved. *Exploring CO₂ reduction on Cu from a geometrical perspective with the NanoCHE model*. MSc Thesis, KCL (2019).
- [67] K.Rossi et al. *Screening and Designing Pt-nanoparticle isomers for Oxygen Reduction*. ACS Catal. 2020, 10, 6, 3911-3920.
- [68] JK. Nørskov et al. *Origin of the Overpotential for Oxygen Reduction at a Fuel-Cell Cathode*. J. Phys. Chem. B 2004, 108, 17886–17892.
- [69] M.Ichimura. *Atomic Structure of Surface Steps and Reconstruction*. Encyclopedia of Materials: Science and Technology, 2001, 383 - 387.
- [70] J.Suzanne et al. *The Structure of Physically Adsorbed Phases*. Handbook of Surface Science, Vol. 1, 1996, 503-575.

- [71] L. Gautier <https://pypi.org/project/rpy2/>, 2020, 3.
- [72] KP. Kuhl et al. *New Insights into the Electrochemical Reduction of Carbon Dioxide on Metallic Copper Surfaces*. Energy Environ. Sci. 2012, 5, 7050-7059.
- [73] E.L. Clark et al. *Standards and Protocols for Data Acquisition and Reporting for Studies of the Electrochemical Reduction of Carbon Dioxide*. ACS Catal. 2018, 8, 6560 -6570.
- [74] S. Lewis et al. *Powering the Planet: Chemical Challenges in Solar Energy Utilization*. Proc. Natl. Acad. Sci. 2006, 103, 15729-15735.
- [75] S. Chuet al. *Opportunities and Challenges for a Sustainable Energy Future*. Nature 2012, 488, 294-303.
- [76] Z. Seh et al. *Combining Theory and Experiment in Electrocatalysis: Insights into Materials Design*. Science 2017, 355, 1-12.
- [77] J.E. Pander et al. *Practices for the Collection and Reporting of Electrocatalytic Performance and Mechanistic Information for the CO₂ Reduction Reaction*. Catal. Sci. Technol. 2017, 7, 5820-5832.
- [78] Hori et al. *Electrochemical Reduction of CO at a Copper Electrode*. J. Phys. Chem. B, 1997, 101 , 7075 —7081.
- [79] Hori et al. *Formation of Hydrocarbons in the Electrochemical Reduction of Carbon Dioxide at a Copper Electrode in Aqueous Solution*. J. Chem. Soc., Faraday Trans. 1, 1989, 85 , 2309-2326.
- [80] Kortlever et al. *Catalysts and reaction pathways for the electrochemical reduction of carbon dioxide*. J Phys Chem Lett 6:4073–4082.
- [81] Y. Hori. *CO₂ reduction using electrochemical approach. Solar to Chemical Energy Conversion: Theory and Application*. Springer International, Cham, Switzerland, 191–211.
- [82] F. Baletto et al. *Crossover among structural motifs in transition and noble-metal clusters*. J. Chem. Phys. 2002, 116, 3856.

- [83] C. Zeni et al. <https://pypi.org/project/mff/>. 2020, 02.
- [84] G. L. De Gregorio et al. *Facet-dependent selectivity of Cu catalysts in electrochemical CO₂ reduction at commercially viable current densities*. ACS Catal. 2020, 4.

Appendices

Appendix A

Here some examples of how the NP geometrical analysis was carried out when defining the Ih, FCC or Dh classes. Figures 5.1, 5.1 and 5.1 display the CNA pattern of NPs at different time snapshots for the three different processes.

As expected, the liquid structures have a similar CNA pattern distribution associated to them, with peaks at (311) and (433) signatures. With the time evolution, all the structures take on a peak in the (421) signature, corresponding to an FCC environment, but the latter is more evident in the two Octahedra than in the Ih structure. The Ih has a higher occurrence of (555) symmetries and a lower occurrence of (211), as expected. The other two structures have a higher occurrence of (211), typical of Oh structures, but a lower occurrence of (311) compared to the Ih. Cu₉₇₆ presents no five-fold symmetries, while the meant-to-be Oh seems to exhibit a very low percentage of them, due to the fact that it still hasn't reached its completely ordered phase.

The Ih growth maintains a high occurrence of (555) symmetries, while the To evolution presents many (421) patterns, representing its hexagonal facets.

It is harder to interpret the CNA patterns for the final stage of the coalescence processes, since the NPs evolve towards disordered structures.

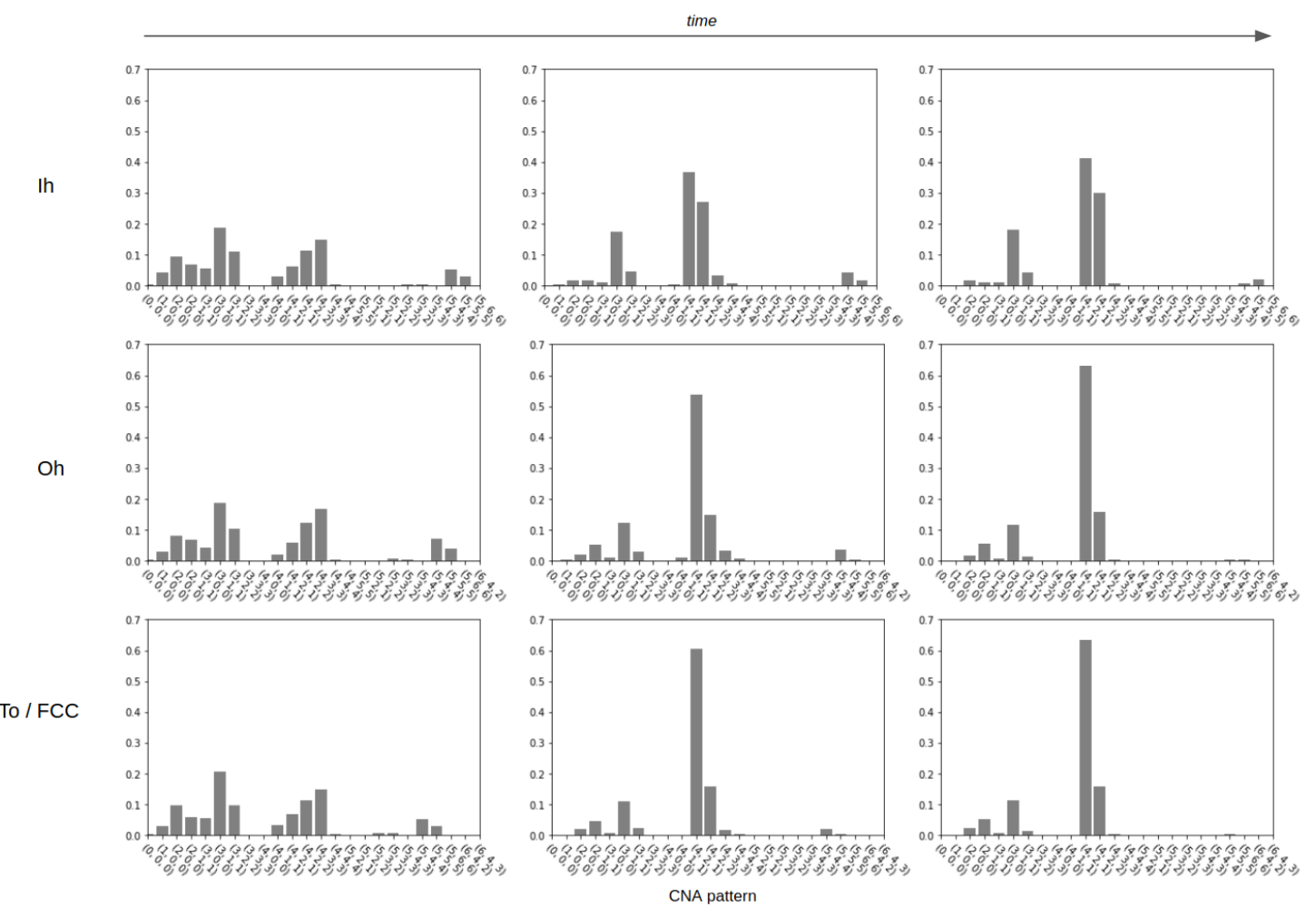


Figure 5.1: CNA pattern evolution for Cu_{561} , leading to an Ih, Cu_{891} , leading to a dOh, and Cu_{976} , leading to a dTo with FCC facets.

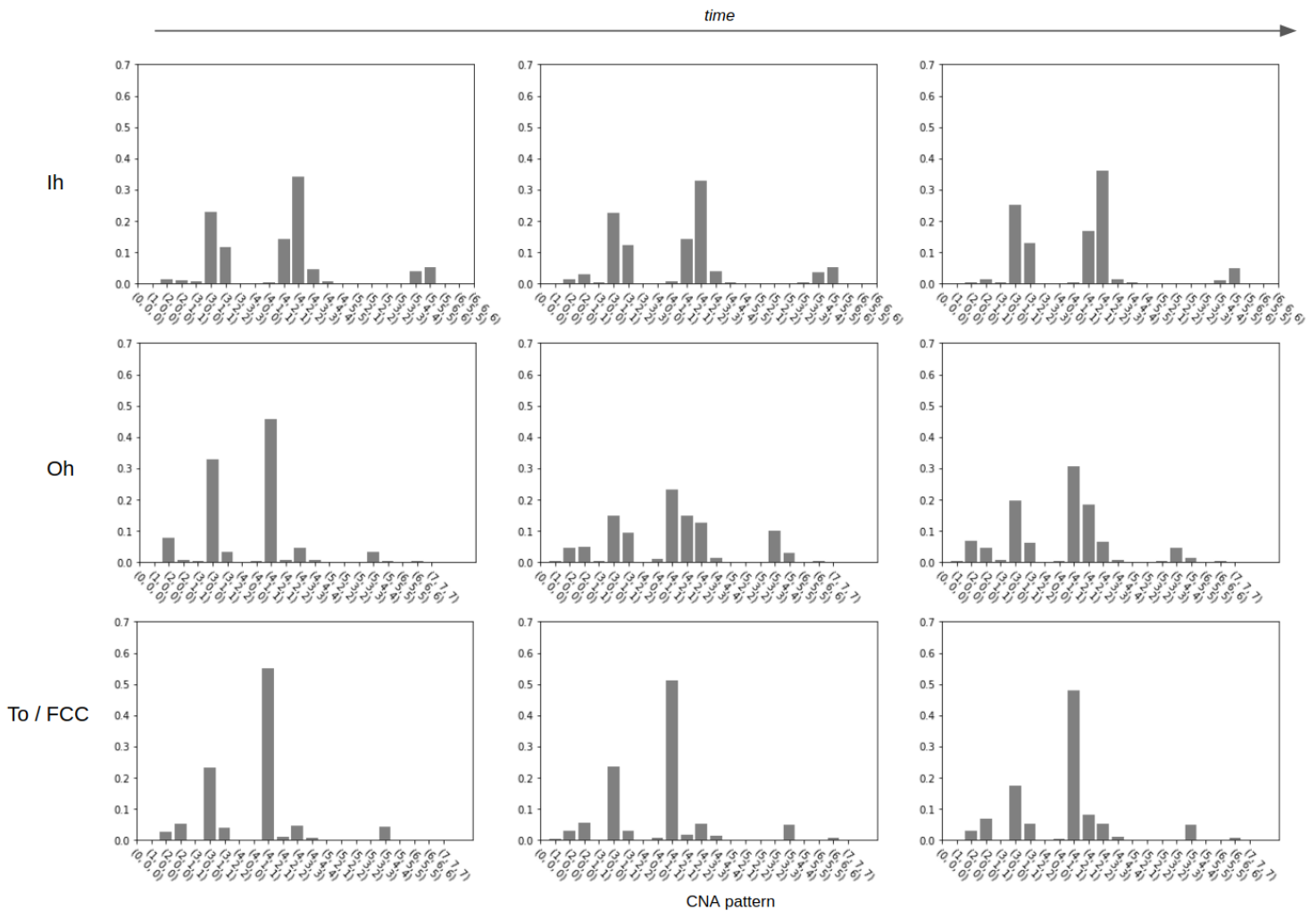


Figure 5.2: CNA pattern evolution for an initial Oh, Ih and FCC, which are grown.

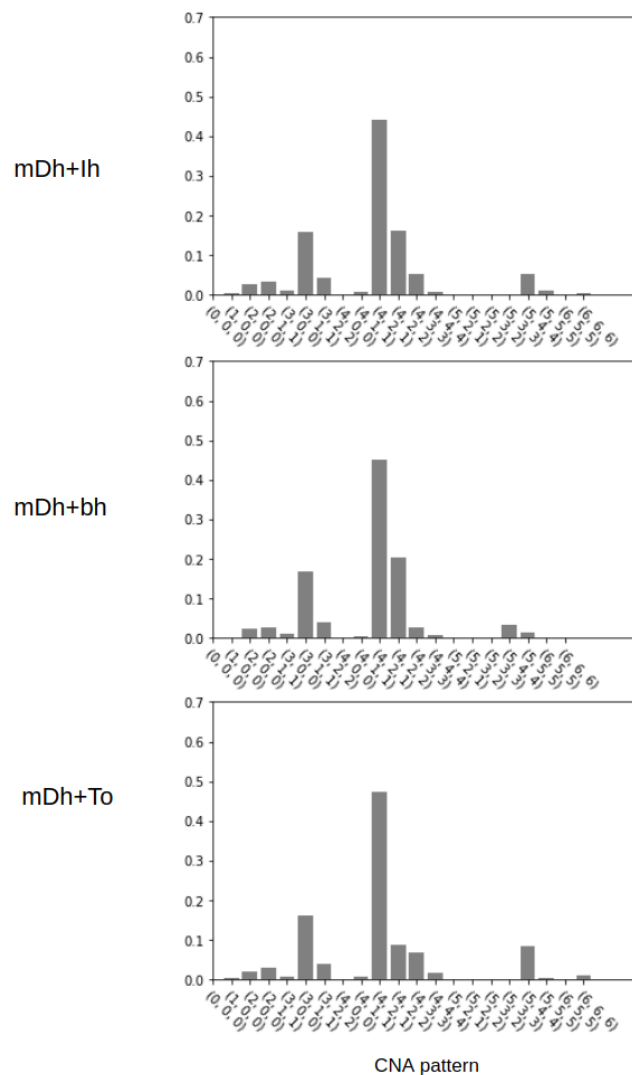


Figure 5.3: CNA pattern for final structures resulting from growth processes.

Appendix B

MY CODE

```
1 """This code does the following:  
2  
3 - Plots the excess energies averaged over all simulations. ( $\Delta E = (E_{coh} - E_{pot})/\{N^{2/3}\}$ )  
4 - Reads a movie.xyz file and calculates the Pair Distribution Function (PDF) of  
    the cluster  
5     averaged over all time frames. It then individuates the first noticeable  
      minimum, whihc corresponds  
6     to the radius for cut off.  
7 - Calculates the atop Generalized Coordination Number (aGCN) for each atom for  
    each time frame.  
8     (aGCN_i=sum_j (CN_j/12)).  
9 - Plots histograms of relevant time steps for an easy comparison.  
10 - Outputs a new movie file (movie-aGCN.xyz) with a column (last columns) with the  
      aGCN genome, readable  
11     by Ovito and easily visualizable.  
12 - Plots a heatmap of the aGCN occurrence over time (this takes some time).  
13 - Calculates the surface area (in  $cm^2$ ) of the NP and its evolution through time  
      and plots it  
14     ( Sum(from i to N)  $4\pi r^2(1-(aGCN(i)/12))$  ).  
15 - calculates the current density j (in  $mA/cm^2$ ) for an applied potential between  
      -1.299 and 0 V  
16     from the relations by Zhao et al. (J. Phys. Chem. C 2016, 120, 28125-28130.)  
      and through an equation  
17     in which the constant is specific to each case ( $C = -1530172262342.5735$  for  
      copper). It then plots j at initial,  
18     middle and final time steps.  
19 - calculates the mass activity (MA) (in  $mA/mg$ ) evolution through time of the NP  
      through the  
20     formula  $MA = (A_{surf} * SA) / M$ , where SA is the current density for a specific  
      applied potential (-1.1V)  
21     and M is the NP's mass.  
22  
23 """
```

```

24
25 from asap3 import FullNeighborList
26 from ase import Atoms
27 from ase.io import read
28 import numpy as np
29 from matplotlib import pyplot as plt
30 import time
31 from scipy.interpolate import interp1d
32 import seaborn as sns
33 import pickle
34 import numpy as np
35 from itertools import groupby
36 from collections import namedtuple
37 from scipy.ndimage import gaussian_filter1d
38 import math
39
40 """YOUR folder, the code will automatically select the files needed.
41 Make sure you have a movie.xyz file and an energy.out file.
42 If not, comment some of the following lines to address your specific needs."""
43
44 folder= "..."
45 filename = str(folder)+'movie.xyz'
46 traj = read(filename, index = ':')
47
48 """Check that the time in the energy file is in the fourth column.
49 For growth, change [:,4] to [:,5]. """
50 energy= np.loadtxt(str(folder)+'energy.out')[:,4]
51 PATH_TO_NEW_MOVIE = str(folder)+"movie-AGCN.xyz"
52
53 """Check that the time in the energy file is in the first column"""
54 tempo=np.loadtxt(str(folder)+'energy.out')[:, 0]
55 time_red=tempo/1000    #converting in to ns.
56
57 """CONSTANTS TO BE UPDATED AND INSERTED MANUALLY BY THE USER !!!"""
58 sigma=2  #how much you want to smoothen out your functions?
59 applied_V=1.1  #at whihc voltage do you want the mass activity calculation to
     happen?

```

```

60 U_bins = 1299 #binning of the voltages (v)
61 beta= 1/((8.6173303E-5)*(300)) #Boltzmann constant at room temperature. Change
   the temperature at whihc you want the catalytic activities to be performed
   at.
62 r=1.28*10**(-9) #atomic radius of your atoms (in cm)?
63 mass_cu = 1.0552e-19 #mass of your atoms (in mg)?
64 C=-30082651629632.555 # constant in equation, to be calculated from initial
   conditions
65 natoms = 586 #number of atoms in system?
66 mass_NP = mass_cu * natoms
67
68
69 """Plots average excess energy evolution from simulations coming from different
   irands.
70 Modify in a way that if you have more than four simulations, """
71 def plot_energies(filename):
72     sigma=4           #decide how much you want to smoothen out the curve
   with a Gaussian filter
73     E_tot=[]
74     for j in range(4):
75         E=np.loadtxt(str(folder)+'energy.out')[ :, 4]
76         E.tolist()
77         E_tot.append(E)
78     E_avg=(E_tot[0]+E_tot[1]+E_tot[2]+E_tot[3])/4
79     plt.plot(time_red, gaussian_filter1d(E_avg, sigma))
80     plt.show()
81     plt.close()
82     return
83
84 """Calculates the distances between atoms."""
85 r_cut=10
86 def read_trajectory(filename, r_cut):
87     atom_number_list = [atoms.get_atomic_numbers() for atoms in traj]
88     flat_atom_number = np.concatenate(atom_number_list)
89     elements = np.unique(flat_atom_number, return_counts=False)
90     all_distances = []
91     for i, atoms in enumerate(traj):

```

```

92     atoms.set_cell([[100, 0, 0], [0, 100, 0], [0, 0, 100]])
93     nl = FullNeighborList(r_cut, atoms=atoms)
94     for i in np.arange(len(atoms)):
95         indices, positions, distances = nl.get_neighbors(i)
96         all_distances.extend(distances**0.5)
97     return all_distances
98
99 """Creates the r_cut_cn, the cut_off radius for further aGCN calculations. """
100 def create_function(distances, r_cut):
101     y, bin_edges = np.histogram(distances, bins = np.linspace(0, r_cut, r_cut
102                               *100+1))
103     x = bin_edges[:-1] + 0.005
104     y = np.array(y) / sum(np.array(y))
105     spline = interp1d(x, y)
106     values = np.linspace(1, 5, 100)
107     x=np.asarray(x)
108     minima=[]
109
110     """ Finding the minima in a very general way, finding the 10th y-value (
111     percentage of
112     atoms within a certain radius) value before and after a point on the x-axis
113     """
114
115     for i in range (len(y)-10):
116         if y[i]<y[i+10] and y[i]<y[i-10]:
117             minima.append(x[i])
118
119     global r_cut_cn
120
121     """r_cut_cn is the first encountered minima, used for cn calculation"""
122     r_cut_cn=minima[0]
123     print("Radius for cutoff=", r_cut_cn)
124     plt.plot(values, spline(values))
125     plt.show()
126
127     return spline, r_cut_cn
128
129
130
131 """Atop Genralized Coordination Number calculation. Returns different arrays:agcn
132     , a 2D array
133
134     (every 1D composing it refers to a single time step) of aGCNs between 2 and 9,
135     agcn_tot_1D, a 1D array of all the values

```

```

123 over all time frames, and agcn_tot_2D, a 2D array of all aGCN values (1D arrays
    correspond to singular
124 time frames). """
125 def cn_generator (filename, r_cut_cn):
126     global agcn, agcn_tot_1D, agcn_tot_2D
127     agcn_tot_1D=[]
128     agcn_tot_2D=[]
129     agcn=[] #containing arrays of aGCN at every time step
130
131     for i, atoms in enumerate(traj):
132         #frame by frame
133         cn_frame=[]
134         agcn_frame=[]
135         agcn_tot_frame=[]
136         atoms.set_cell([[100, 0, 0], [0, 100, 0], [0, 0, 100]])
137         ind=[]
138         for j in np.arange(len(atoms)):
139             nl = FullNeighborList(r_cut_cn, atoms=atoms)
140             indices, positions, distances = nl.get_neighbors(j)
141             ind.append([int(k) for k in indices])
142             distancej=[]
143             distancej.extend(distances**0.5)
144             cnj=len(distancej)
145             cn_frame.append(cnj)
146             for l in np.arange(len(atoms)):
147                 cc=ind[l][:]
148                 list=[]
149                 for m in range(len(cc)):
150                     list.append(cn_frame[ind[l][m]])
151                     sm=sum(list)/12
152                     agcn_tot_1D.append(sm)
153                     agcn_tot_frame.append(sm)
154                     #we only want surface atoms, whihc have an atop GCN smaller than
155                     #11, from the freezing graphs
156                     if sm<=9:
157                         agcn_frame.append(sm)
158
159 agcn_frame=np.asarray(agcn_frame)

```

```

158     agcn_tot_frame=np.asarray(agcn_tot_frame)
159     #rounding it to first decimal figure
160     agcn_frame=np.around(agcn_frame, 2)
161     agcn_tot_frame=np.around(agcn_tot_frame, 2)
162     agcn.append(agcn_frame)
163     agcn_tot_2D.append(agcn_tot_frame)
164     agcn=np.asarray(agcn) #2D array: only surface atop GCN rounded at first
165     decimal figure, each subarray corresponding to one time frame
166
167     return (agcn, agcn_tot_1D, agcn_tot_2D)

168
169 def plot_hist (filename):
170
171     plt.hist(agcn[0], bins=45, histtype= 'step', lw = 3, color='orange', label='
172     liquid')
173     plt.hist(agcn[int(len(agcn)/2)], bins=45,histtype= 'step', lw=2, color='
174     purple', label = 'freezing T')
175     plt.hist(agcn[len(agcn)-1], bins=45, histtype= 'step', lw=2, color = 'r',
176     label = 'solid')
177     plt.xlabel('aGCN', size='15')
178     plt.ylabel('Distribution', size='15')
179     plt.xticks(size='13')
180     plt.yticks(size='13')
181     #plt.legend(prop={'size': 13}, bbox_to_anchor=(1, 1))
182     plt.savefig(str(folder)+'full_hist.png', bbox_inches='tight')
183     plt.show()
184     plt.close()

185
186     return

187
188 def heatmap(filename):
189
190     occ_long=[]
191
192     for i in range(len(agcn)):
193         (n, bins, patches)=plt.hist(agcn[i], bins=90, density=True)
194         occ_long.append(n)
195
196     occ_long=np.asarray(occ_long)
197
198     global corrected_occ
199
200     corrected_occ=np.zeros((90, len(agcn)))

```

```

191     for i in range(90):
192         corrected_occ[-i-1]=np.asarray(occ_long[:, i])
193     print(corrected_occ)
194     sns.heatmap(corrected_occ, vmax=1, xticklabels=False, yticklabels=False, cbar
195 =False)
196     plt.savefig(str(folder)+'occurrency.png', bbox_inches='tight', dpi=400)
197     plt.show()
198     plt.close()
199
200 def readMovieFileXYZ(path_to_movie):
201     """
202     Reads a LoDiS movie.xyz file and fetches the coordinates
203     for each atom for each frame.
204
205     Input:
206         path_to_movie: path to movie.xyz
207
208     Returns:
209         Named tuple read_movie:
210             - read_movie.Frames: list of frames; each is an array of atoms each
211             described by [Atom, x, y, z, Col]
212             - read_movie.Headers: list of the movie frames headers"""
213
214     read_file_chars = []
215
216     with open(path_to_movie, 'r') as file:
217
218         for line in file:
219
220             read_file_chars.append(line)
221
222         # 1. Delete line jump
223
224         read_file_chars = [line[:-1] for line in read_file_chars]
225
226         read_file_chars
227
228         # 2. Separate line by line
229
230         grouped_lines = [(list(group) for k, group in groupby(line,lambda x: x == "
231             ") if not k]) for line in read_file_chars]
232
233         # 3. Concatenate characters
234
235         joined_string = [','.join(info_elem) for info_elem in grouped_line] for
236         grouped_line in grouped_lines]
237
238         # 4. Regroup into list of lists. Elements of outerlist are movie frames
239
240         merged_frames = []
241
242         current_frame = []

```

```

224     for line in joined_string:
225         if(line==joined_string[0]):
226             if len(current_frame)!=0:
227                 merged_frames.append(current_frame)
228             current_frame=[]
229         else:
230             current_frame.append(line)
231     merged_frames.append(current_frame)
232 # 5. Removing second line of header
233 movie_headers_all_frames = [frame[0] for frame in merged_frames]
234 merged_frames = [frame[1:] for frame in merged_frames]
235 # 6. Converting coordinates and pressure to floats
236 for frame in merged_frames:
237     for line in frame:
238         line[1] = float(line[1]) # x coord
239         line[2] = float(line[2]) # y coord
240         line[3] = float(line[3]) # z coord
241     Movie = namedtuple('Movie', 'Frames Headers')
242     read_movie = Movie(merged_frames, movie_headers_all_frames)
243     return(read_movie)

244
245
246
247 def catalytic_analysis (filename):
248     current=[]
249     mass_activity=[]
250     y=[]
251     for j in range(0, len(agcn)):
252         surf_area=0
253         for i in range(len(agcn[j])):
254             once = 4*np.pi*r**2*(1-agcn[j][i]/12)
255             surf_area = surf_area + once
256         y.append(surf_area)
257         surface_area=gaussian_filter1d(y, sigma)
258         site=np.zeros((U_bins))
259
260         for h in range(U_bins):

```

```

261         spec=0
262
263     for m in range(len(corrected_occ)):
264
265         if m<31:
266
267             sitecurrent = C*np.exp(((0.162 * m/10 - 1.11)-(h*0.001))*beta
268             )*m/10*corrected_occ[m][j]/len(agcn[j])
269
270         elif 31<=m<81:
271
272             sitecurrent = C*np.exp(((0.067 * m/10 - 0.416)-(h*0.001))*beta
273             )*m/10*corrected_occ[m][j]/len(agcn[j])
274
275         else:
276
277             sitecurrent = C*np.exp(((0.222 * m/10 + 0.849)-(h*0.001))*beta
278             )*m/10*corrected_occ[m][j]/len(agcn[j])
279
280         spec=spec+sitecurrent
281
282     site[h]=spec
283
284     current.append(site)
285
286     mass_activity.append(-site[int(1299-applied_V*1000)]*surf_area/mass_NP)
287
288
289 """Calculation and plot of the surface area, the dashed line corresponds to
the surface area per time
290 step, while the solid line has been smoothened through the Gaussian filter by
whatever amount
291 you desire. Change sigma to explore. """
292
293 plt.xlabel("Time(ns)")
294 plt.ylabel("Surface area (cm^2)")
295 plt.plot(time_red, y, color='black', linestyle='dashed')
296 plt.plot(time_red, surface_area, color='black')
297 plt.savefig(str(folder)+'surf_area.png', bbox_inches='tight', dpi=200)
298 plt.show()
299 plt.close()
300
301 """
302 Plotting the current density at different applied potentials for different
time steps."""
303
304 potentials = np.linspace(-1.299, 0, U_bins)
305 plt.plot(potentials, current[int(len(traj)-1)], color='orange', lw=3, label='final')
306 plt.plot(potentials, current[int(len(traj)/2)-1], color='purple', label='middle')
307 plt.plot(potentials, current[0], color='r', label='initial')

```

```

290     plt.xlabel('V vs RHE')
291     plt.ylabel('j (mA/cm^2)')
292     plt.savefig(str(folder)+'current_densities.png', bbox_inches='tight', dpi=200)
293     plt.show()
294     plt.close()
295
296     """Mass activity plots at desired applied_V."""
297     plt.xlabel('Time(ns)')
298     plt.ylabel('MA (mA/mg)')
299     plt.plot(time_red, mass_activity, linestyle='dashed', color='black')
300     plt.plot(time_red, gaussian_filter1d(mass_activity, sigma), linestyle='solid',
301             , color='black')
302     plt.savefig(str(folder)+'mass_activity.png', bbox_inches='tight', dpi=200)
303     plt.show()
304     plt.close()
305
306
307 if __name__ == '__main__':
308
309     plot_energies(filename)
310
311     tic = time.time()
312     distances = read_trajectory(filename, r_cut)
313     toc = time.time()
314     print("Time to calculate distances: %.2f [s]" %(toc-tic))
315
316     tic = time.time()
317     create_function(distances, r_cut)
318     toc = time.time()
319     print("Time to create spline: %.2f [s]" %(toc-tic))
320
321     tic = time.time()
322     agcn, agcn_tot_1D, agcn_tot_2D= cn_generator(filename, r_cut_cn)
323     toc = time.time()
324     print("Time to calculate aGCN: %.2f [s]" %(toc-tic))

```

```

325
326     plot_hist(filename)
327
328     heatmap(filename)
329
330     catalytic_analysis(filename)
331
332 """Appending a last column to the movie file with aGCN information. """
333
334 with open(PATH_TO_NEW_MOVIE, 'a+') as newmovie: # Mode chosen: append
335     movie = readMovieFileXYZ(filename)
336     NATOM = int(len(movie[0][0]))
337     open(PATH_TO_NEW_MOVIE, 'w').close() #Clear old movie pressure file
338     for frame_num, current_frame in enumerate(movie.Frames):
339         with open(PATH_TO_NEW_MOVIE, 'a+') as newmovie: # Mode chosen: append
340             num_lines = sum(1 for line in open(PATH_TO_NEW_MOVIE))
341             if (num_lines==0): # No newline for first line -- bugs Ovito if there
342                 is newline at beginning
343                 newmovie.write(str(NATOM)+'\n')
344             else:
345                 newmovie.write('\n' + str(NATOM) + '\n')
346             newmovie.write('\t'.join(str(item) for item in movie.Headers[
347                 frame_num]))
348             for atom_index, atom_info in enumerate(current_frame):
349                 print(atom_index, frame_num)
350                 atom_info[-1] = agcn_tot_2D[frame_num][atom_index] # Adding
351                 pressure to tuple
352                 newmovie.write('\n')
353                 newmovie.write(' \t'.join(str(item) for item in atom_info))

```